EURISOL DS Project

Task 2: Multi MW target station

Deliverable n^o D1

Engineering study of the Hg converter

Planned Date (month): 19

Achieved Date (month): 39

Lead Contractors: P4, P18, P19

Project acronym:	*EURISOL DS*
Project full title:	*EUROPEAN ISOTOPE SEPARATION ON-LINE RADIOACTIVE ION BEAM FACILITY*
Start of the Project:	*1st February 2005*
Duration of the project:	*54 months*

EURISOL-DS/TASK2/Deliverable D1

Engineering study of the Hg converter

For the Multi-Megawatt target station

Target Group Leader

Y. Kadi

Editor:

K. Samec

Contributors;

M. Ashrafi-Nik, L. Blumenfeld, A. Herrera-Martinez, Y. Kadi, C. Kharoua, J. Lettry, M. Lindroos, R. Rocca

CERN
European Laboratory for Particle Physics,
Geneva, CH-1232, Switzerland

I. Bucenieks, E. Freibergs, A. Flerov, N. Jēkabsons[a], K. Kravalis, P. Lūķis, S. Ivanov, E. Platacis, A. Romančuks, J. Šeimanis, A. Ziks

IPUL
Institute of Physics, University of Latvia, Salaspils, LV-2156 Latvia
[a] Independent, contracted from Jekabsons Engineering Systems

P. Barbagallo, E. Brun, S. Dementjev, T. Dury, F. Gröschel, A. Kalt, E. Manfrin, R. Milenkovic, Q. Prétet, K. Samec, B. Sigg, B. Smith, K. Thomsen, W. Wagner.

PSI
Paul Scherrer Institut,
Villigen, CH-5232, Switzerland

Table of Contents

-

L i s t o f F i g u r e s

-

L i s t   o f   T a b l e s

-

R e f e r e n c e s

-

[Ref1]	Y. Kadi: Baseline parameters Eurisol-DS Multi-MW target station"		
	Eurisol N°02-25-2006-0011	Eurisol Technical Note	January.2006
[Ref2]	A. Herrera-Martínez: Neutronic Calculations for the Baseline Configuration of the Multi-MW Target		
	ABNote-2006-035 ATB	CERN Internal Report	January 2006
[Ref3]	A. Herrera-Martínez: Target Preliminary Study of the Liquid Metal Proton to Neutron Converter		
	AB-Note-2006-013 ATB	CERN Internal Report	January 2006
[Ref4]	A. Herrera-Martínez: Comparative Neutronic Performance of the Baseline Configuration vs. the Hg-Jet Option		
	AB-Note-2006-037 ATB	CERN Internal Report	January 2006
[Ref5]	K. Samec: Best-estimate fit for EURISOL Heat Deposition Profiles		
		PSI Technical Memo	September 2006
[Ref6]	Q. Prétet: Stress Analysis of the EURISOL DS target		
	TM-34-06-02	PSI Technical Report	October 2006
[Ref7]	M. Ashrafi-Nik : Thermo hydraulic optimisation of the EURISOL DS target		
	TM-34-06-04	PSI Technical Report	December 2006
[Ref8]	K. Samec: Design of the Eurisol converter target		
	TM-34-07-05	PSI Technical Report	July.2007
[Ref9]	V. Geza: Hydraulic simulation of the flow condition at the inlet of the beam entrance window of the EURISOL converter target		
	EURISOL-MR34-004/0	PSI External report	May 2008
[Ref10]	K. Samec: Test predictions for the converter target		
	AB-Note-2008-057 ATB	CERN Internal Report	September 2008
[Ref11]	CEA Nuclear Code RCCM-R		
	CEA	Nuclear Code	1993 edition
[Ref12]	K. Samec: Off-line thermal and fluid dynamics test of the converter		
	D4	EU Deliverable N°D4	July 2009

[Ref13]	J. Neuhausen: Innovative Waste Management in the Mercury Loop		
	D2	Eurisol Deliverable	July 2009
[Ref14]	E. Freibergs: Engineering design and construction of a functional mercury loop		
	D3	Eurisol Deliverable	2008
[Ref15]	E. Freibergs: Assembly of complete Hg Loop with window less jet		
	02-25-2009-0035	Eurisol technical Note	May 2008
[Ref16]	L. Blumenfeld: CFD post test analysis of METEX measurements		
	EN-Note-2009-008 STI	CERN Internal Report	July 2009
[Ref17]	C. Kharoua; EURISOL-DS Multi-MW Target Study of the WTF Liquid Metal Proton-to-Neutron Converter		
	EN-Note-2009-003 STI	CERN Internal Report	July 2009
[Ref18]	A. Konobeyev: Analysis of nuclide production in the MEGAPIE target		
	Vol. 605 p224–232	NIMA Article	April 2009
[Ref19]	K. Samec: Target Fluid-structure interaction		
	TN-02-25-2009-0034	EURISOL Technical note	January, 2009
[Ref20]	M. Ashrafi-Nik: Beam influence on thermal-hydraulics of EURISOL DS liquid metal target		
	TM-34.07	EURISOL Technical note	July 2007

1 Introduction

1.1 Role of the converter target in Eurisol

The development of high-power converter targets otherwise known as neutron sources is today the focus of much attention, driven by the need for ever greater densities of neutron fluxes which are required in the fundamental sciences such as neutron imagery, isotope production and also for the more long-term goal of realising a hybrid sub-critical nuclear reactor. The neutrons in a converter target are produced by a process known in physics as spallation whereby a heavy Z atom releases neutrons below 20 [MeV] when hit by an incoming proton.

The Eurisol initiative seeks to develop such an isotope production facility to provide the scientific community with the means to achieving high yields of isotopes and extending the variety of isotopes thus produced towards more exotic types rarely seen in existing facilities.

The scientific case for promoting the use of high-intensity radioactive Ions Beams (RIBs) using the ISOL method includes :

- o the study of atomic nuclei under extreme and so-far unexplored conditions of composition (i.e. as a function of the numbers of protons and neutrons, or the so-called isospin), rotational angular velocity (or spin), density and temperature;

- o the investigation of the nucleo-synthesis of heavy elements in the Universe, an important part of Nuclear Astrophysics;

- o a study of the properties of the fundamental interactions which govern the properties of the Universe, and in particular of the violation of some of their symmetries;

- o potential applications of RIBs in Solid-State Physics and in Nuclear Medicine, for example, where completely new fields could be opened up by the availability of high-intensity RIBs produced by the ISOL method. These cases require a 'next generation' infrastructures such as the proposed EURISOL facility, with intensities several orders of magnitude higher than those presently available or planned, allowing the study of hitherto completely unexplored regions of the Chart of the Nuclei.

The main components of the proposed facility (Figure 1) are: a driver accelerator, a target/ion source assembly, and a mass-selection system. The driver accelerator investigated in this study is a 1-3 GeV, Multi-MW, superconducting proton linear accelerator, although the implications of enabling it to accelerate light nuclei were also considered.

An alternative suggestion, i.e. an electron accelerator using Bremsstrahlung to generate photo fission, was also examined, but found to have limitations which would make it more expensive for the high yields demanded for EURISOL.

The proposed ISOL facility would use both (a) several 100 kW proton beams on a thick solid target to produce RIBs directly, and (b) a liquid metal 1–5 MW 'converter' target to release high fluxes of spallation neutrons which would then produce RIBs by fission in a secondary uranium carbide (UCx) target. An alternative windowless liquid mercury-jet 'converter' target to generate the neutrons has also been proposed for this Multi-MW target station.

The Multi-MW converter target at the heart of the projected facility is designed to create isotopes by fissioning uranium carbide (UC) target arranged coaxially around a 4 MW converter target. It is therefore essential that

the target be as compact as possible to avoid losing neutrons to capture whilst maximising the neutron flux to enhance the number of fissions per second in the UC targets.
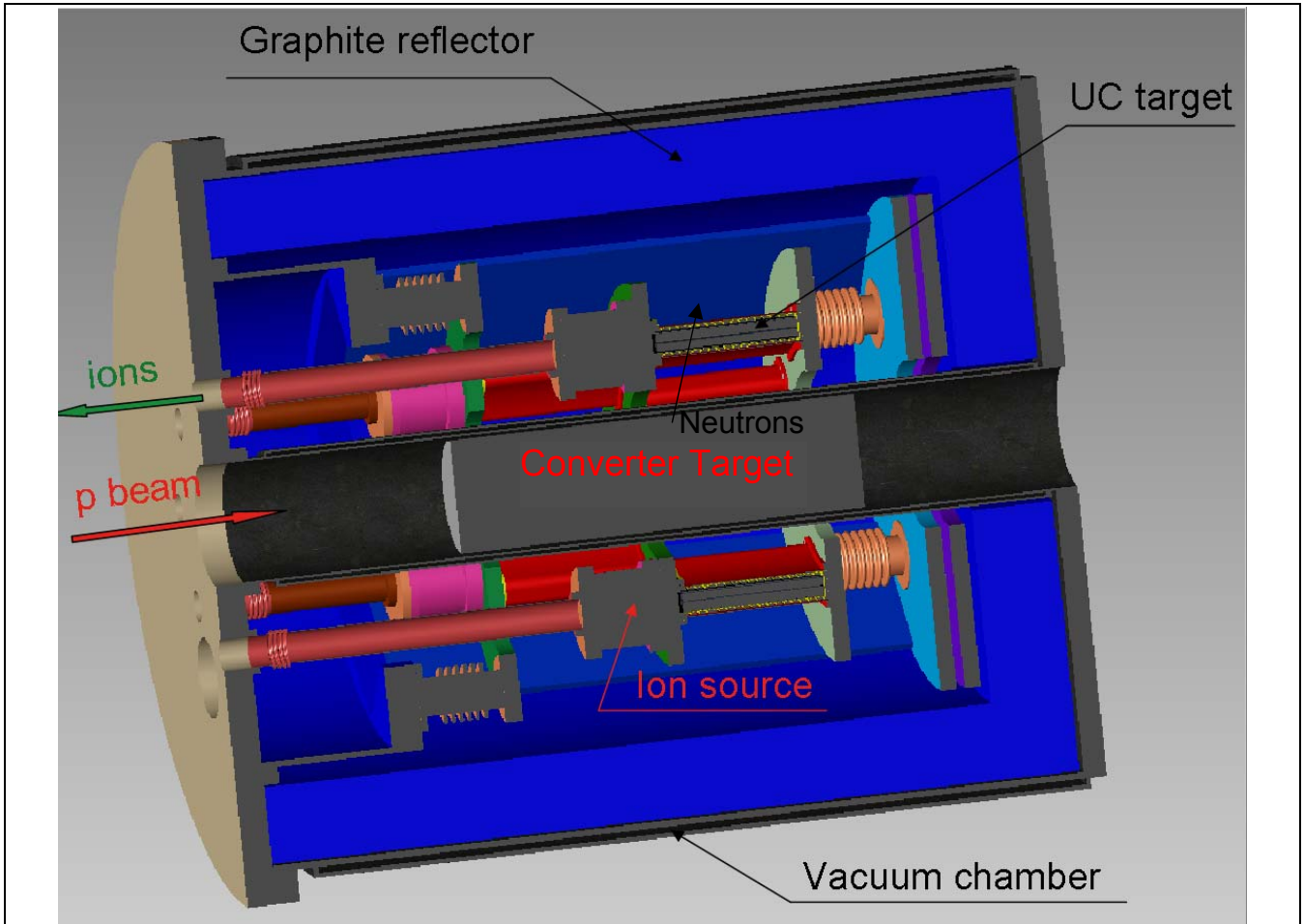
Figure 1: EURISOL general layout

Since the purpose of the facility is to produce rare radioisotopes, maximising the yield of such isotopes is the main objective in the design. In the case of the proton-to neutron converter this implies increasing the neutron yield and reducing the parasitic absorptions in the converter.

The compactness and efficiency of the spallation target is mandatory in order to minimise the total inventory of material in the facility and attain the specified neutron flux and fission density. Reducing the dimensions of the target would have a positive impact on the radioprotection and waste management of the facility (e.g. confinement of the radioactive material, lesser production of radioactive heavy metals to be disposed of) as well as it would cut the final costs of the project. Moreover, to increase the fission rate in a non-enriched target, the neutron energy spectrum should lie in the fast neutron region, since fission cross-sections for non-fissile isotopes are higher at these energies. This harder neutron spectrum may be achieved by decreasing the moderation of the spallation neutrons in the target.

The resulting conflicting demands on the converter target present a challenge in terms of evacuating heat depositions rates of up to 8 [kW/cm3].The necessity to dissipate high heat densities has lead to the development of neutron sources containing liquid metal as target material, as was the case in the MEGAPIE project which operated successfully at close to 1 [MW] beam power for over 4 months in 2006. Allowing for the evacuation of the heat from the converter, in particular from the liquid metal target to beam window interface is one of the most complicated issues when dealing with high power spallation targets.

1.2 Essential system parameters

The parameters governing the design of the target and loop are outlined in the table below. They are the result of an optimisation process which was lead by the physics optimisation (see section 1.3.1 hereafter), the goal being to increase the yield of rare isotopes.

One notices in Table 1 that as the parameters progress towards the engineering characteristics, design options are more open. This is a consequence of the optimisation process which leant heavily towards a precise physics operation and thereby narrowed down the parameters of the beam and target material early on in the development of the program.

In Table 1, the column "Nval" contains the nominal (baseline) value of the parameter for which the design will be optimised. The range to which the study will be extended is described by the second column designated "Range"

Parameter	Symbol	Units	Nval	Range
Converter Target material	Z_{conv}	-	Hg (liquid)	LBE
Secondary Target material	Z_{targ}	-	UC_x, BeO	
Beam particles	Z_{beam}	-	Proton	
Beam particle energy	E_{beam}	GeV	1	≤ 2
Beam current	I_{beam}	mA	4	$2-5$
Beam time structure	-	-	dc	ac 50Hz 1ms pulse
Gaussian beam geometry	σ_{beam}	mm	15	≤ 25, parabolic
Beam power	P_{beam}	MW	4	≤ 5
Converter length	l_{conv}	cm	45	≤ 85
Converter radius (cylinder)	r_{conv}	cm	15	$8-20$
Hg temperature	T_{conv}	°C	150 (tbc)	$\ll 357$
Hg flow rate	Q_{conv}	ton/s	1 (tbc)	$\ll 3$
Hg speed	V_{conv}	m/s	5 (tbc)	$\ll 15$
Hg pressure drop	ΔP_1	bar	tbc	$\ll 100$
Hg overpressure	ΔP_2	bar	tbc	$\ll 100$
UC_x temperature	T_{targ}	°C	2000	500-2500

Table 1: Essential system parameters [Ref1]

The neutronic analysis of the proton beam heat deposition is an important governing parameter which is critical to the design of the converter targets. The deposition is recorded by the FLUKA code in the form of discrete values in a discretised space (referred to as "binning" by neutron physics specialists). The deposition rates can then be transferred to a thermo-hydraulic code for detailed engineering studies of the target.

1.3 Review of the neutronic performance

1.3.1 Optimisation process

The production of neutrons through the spallation reaction is a well-known technique, studied since the 1950's and currently applied in a wide range of processes. It is based on a charged particle induced cascade in a generally high-Z and high-density material. In such a charged particle induced cascade one can distinguish between two qualitatively different processes: a spallation-driven high-energy phase and a neutron driven

regime. In the first phase, neutrons are produced by spallation and act as a source for the following phase, in which they gradually loose energy by collisions and are multiplied, in some cases, by fission or (n, xn) reactions.

Therefore, depending on type of neutron source required, e.g. pulsed sources with a wide energy range for time-of-flight measurements, continuous sources presenting a hard spectrum for accelerator-driven systems etc.), the following governing parameters must be selected:

o   The target material; mercury was compared to lead bismuth eutectic as target material in terms of neutron production and power densities.

o   The target dimensions; radii ranging from 10 to 40 cm and active lengths ranging from 40 to 100 cm were studied.

o   The incident particle type. Protons and deuterons were considered.

o   The incident particle energy: 1-3 GeV for protons and 100 MeV-1 GeV for deuterons.

o   Beam profile: the optimum beam standard distribution was studied in order to decrease the power densities.

Indeed, the choice of the target dimensions and material is a critical issue for the neutronics of the system and the operation of the facility. Such decisions have an incidence on the activation of the facility or the neutron source efficiency. The nature of the incident particle influences the spatial and energy distribution of the neutrons and the power densities in the target.

A study in [Ref3] was therefore carried out in order to determine the optimum value of relevant parameters in the target design. Different scenarios were simulated using the Monte Carlo code FLUKA. Namely, sensitivity studies were performed to assess the impact of the projectile particle energy on the neutronics and energy deposition in the spallation target.

The optimal target dimensions were also studied for every case as well as the proper target material for the liquid metal proton-to-neutron converter, since mercury and lead-bismuth eutectic are reasonable options. The effect of the beam width on the power densities were also evaluated, taking into account the geometrical limitations of the facility. Finally, a comparison between protons and deuterons as primary particles was performed, acknowledging the limitations of using FLUKA for these simulations.

The results of these calculations showed the benefit of using protons as primary particles and increasing their energy, in order to reduce the high power densities occurring in the first few centimetres downstream from the interaction point.

A 2 GeV proton beam with a σ~15 mm Gaussian distribution on a 15 cm radius 50 cm long target seemed a suitable trade between increasing the neutron and fission yields and reducing the power densities in both, the liquid metal and fission targets.

After this preliminary study [Ref3] carried out in order to understand the nature of the interactions taking place in the proton-to-neutron converter, the performance of a Hg target design were addressed in more detail in [Ref2] focusing on issues, such as the composition of the fission target and use of a neutron reflector. The detail study also attempted to integrate all these various components and estimate the system-level performance in terms of number of fissions, isotopic yields and power densities.

The results of these calculations demonstrate the feasibility of a Multi-MW target design and the possibility of achieving the desired fission rates with a reduced fission target. The assembly has been characterised in terms of neutronics and power densities, both key factors in the technical design, due to the high isotopic yields aimed for and the large foreseen power densities.

1.3.2 The neutronic code and physics assumptions

The Fluktuierende Kaskade (FLUKA) code is a general purpose tool used in the calculation of particle transport and interactions with matter, covering an extended range of applications spanning from proton and electron accelerator shielding to spallation target design, calorimetry, activation, dosimeter, detector design, Accelerator Driven Systems, cosmic rays, neutrino physics, radiotherapy etc.

The code can accurately simulate the interaction and propagation in matter of about 60 different particles, including neutrons down to thermal energies and heavy ions.

Below a few GeV, the FLUKA hadrons-nucleon interaction models are based on resonance production and decay. Two models are used also in hadrons-nucleus interactions: at momenta below 3-5 GeV/c the PEANUT package includes a very detailed Generalized Intra-Nuclear Cascade (GINC) and a pre-equilibrium stage, while at high energies the Gribov-Glauber multiple collision mechanism is included in a less refined GINC. Both modules are followed by equilibrium processes: evaporation, fission, Fermi break-up, gamma de-excitation.

Moreover, an original treatment of multiple Coulomb scattering and of ionization fluctuations allows the code to handle accurately some challenging problems such as electron backscattering and energy deposition in thin layers even in the few keV energy range.

For neutrons with energy lower than 20 MeV, FLUKA uses its own neutron cross-section library (P5 Legendre angular expansion, currently 200 neutron energy groups), containing more than 140 different materials. Neutron energy deposition is calculated by means of kerma factors; however, recoil protons and protons from (n, p) reactions are transported explicitly.

1.3.3 Governing parameters for increasing the neutron yield

The energy of the incident particle is strongly related to the maximum distance these particles can reach hence to the dimension of the target to limit the number of charged particles escaping.

For the energy range considered (1-3 GeV) the proton range in Hg increases greatly, going from ~46 cm for 1 GeV, to ~110 cm for 2 GeV and ~175 cm for 3 GeV protons, as illustrated in Figure 2 hereafter.
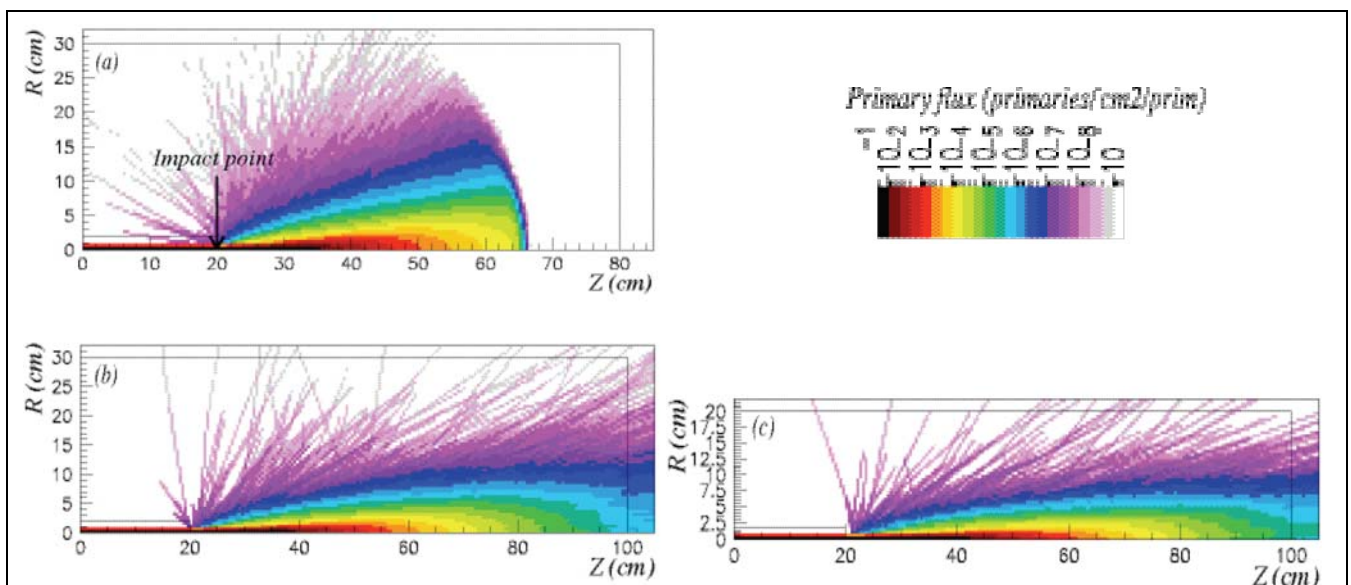
Figure 2: Primaries/cm^2/proton for incident proton energies: (a) 1 GeV, (b) 2 GeV, (c) 3 GeV [Ref2]

For 1 GeV protons, the primary shower (down to 10^{-6} primaries/cm^2/primary) is contained within a solid angle of ~20 degrees. For 2 and 3 GeV, the shower is more forward –peaked, being contained within ~10 and ~8 degrees respectively, therefore allowing a reduction of the target radius to about 10-15 cm, as far as the primary escapes are concerned. Few primary backscattering occurs for 1 GeV protons, but disappear totally at higher energies, thus reducing the need of a beam vacuum inside the target.
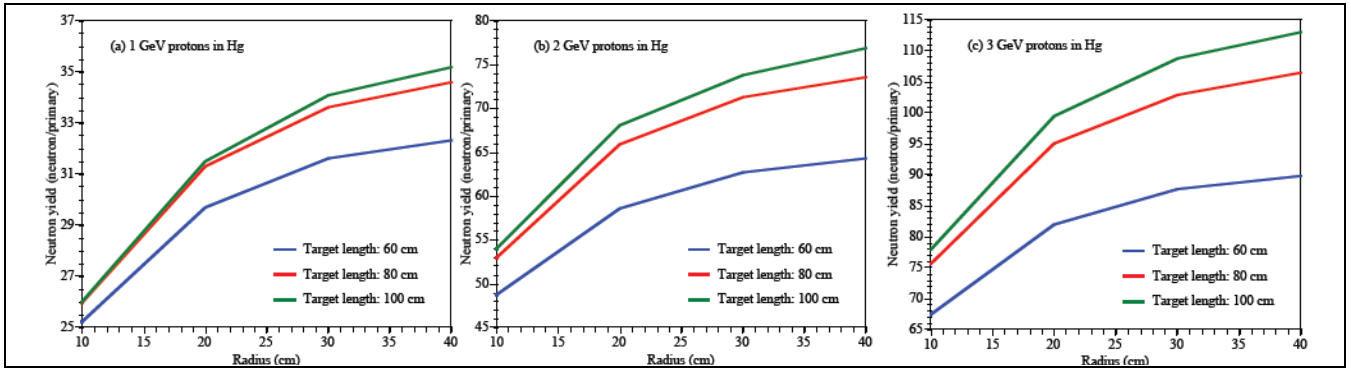
Figure 3: Neutrons/primary as a function of the target dimensions for (a) 1 GeV, (b) 2 GeV, (c) 3 GeV incident proton energy. [Ref2]

The neutron yield increases with the incident proton energy and with the volume of the target decreasing escapes. Nevertheless, the slope of this tendency changes both with the target length and radius. Figure 3.(a), (b) and (c) illustrate this evolution for 1, 2 and 3 GeV, respectively. It can also be seen that for every energy level, there are some target dimensions beyond which the efficiency of the source does not increase significantly. For instance, in the case of 1 GeV protons, an increase of the target radius beyond the proton range has a minor contribution to the neutron yield. Thus, increasing the target radius from 10 to 20 cm increases the yield by 20 %, whereas changing the radius from 30 to 40 cm adds only a 3 % to the neutron yield. Likewise, for the target length and 2 GeV protons, extending the target from 60 to 80 cm would increase the yield by ~18%, whereas an increase from 80 to 100 cm would just improve the yield by ~4%.
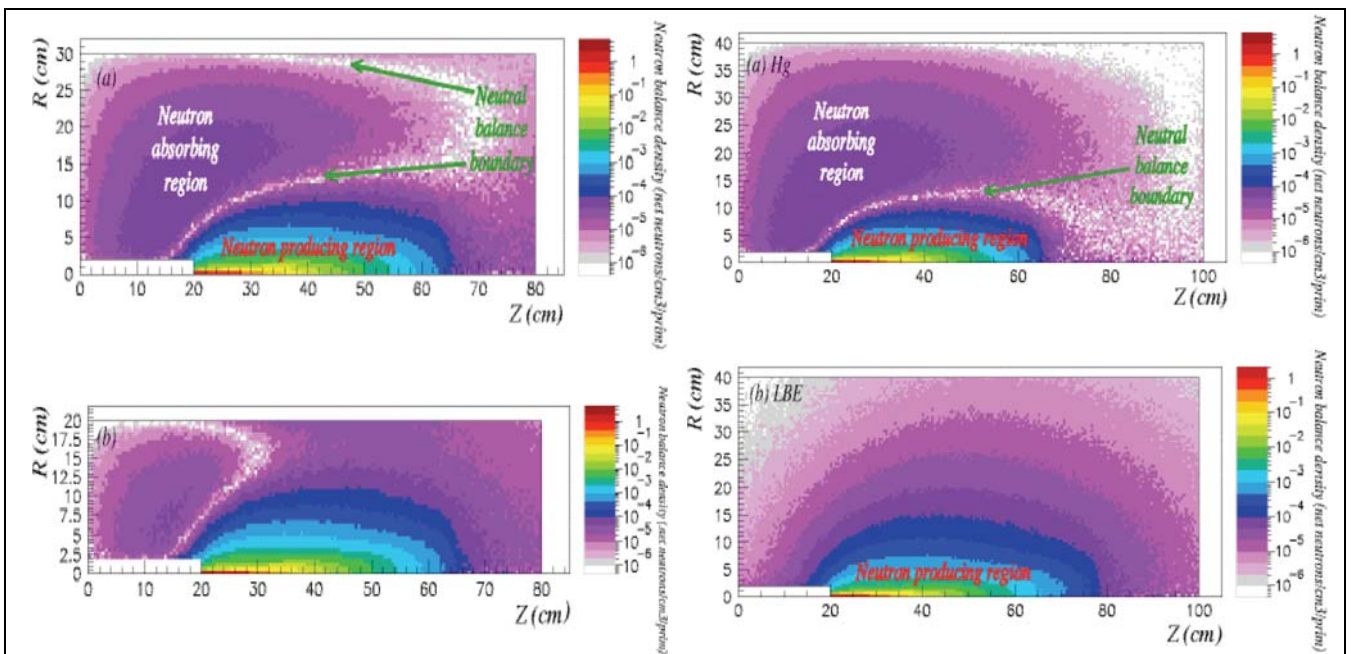
Figure 4: Neutron balance density (net neutrons/cm3/primary) in Hg (left) for a 1 GeV proton beam for a 30 cm radius 80 cm long target (a), and a 20 cm radius 80 cm long target (b). Comparison (right) between Hg (top) and LBE (bottom). [Ref3]

Moreover, Figure 4 shows an excessive increase in target dimensions actually decreases the overall neutron population due to the neutron captures in the periphery. These results conclude that a 20-30 cm radius and a

60 cm (for 1 GeV) or 80 cm long (for 2 and 3 GeV) target is enough for an efficient production of neutrons. As shown in Figure 4 the neutron flux for 2 and 3 GeV follows a similar distribution to the one for 1 GeV, with the exception of a shift in the centre of the spherical distribution, which lies at ~15 cm from the impact point for 2 GeV protons and at ~20 cm for 3 GeV protons. For these higher energies, the high-energy component (above 20 MeV) in the neutron flux gains weight, as explained later in the analysis of the neutron energy distribution.

Hence, the region beyond a 10-12 cm radius represents a minor contribution to the total neutron balance and even acts as an absorbing region, as shown by Figure 5.(a) and (b). Any length beyond the proton range is not necessary (even the last portion of the range) and the region upstream from the impact point should be reduced to about 5 cm and reshaped according to the positive neutron balance distribution.

The neutron energy distribution is a relevant issue, since the fissionable material, i.e. U-238, presents a threshold fission cross-section, for which practically no fissions are produced below the MeV region (Figure 5). A hard neutron spectrum should be favoured and balanced against containment of charged particles.
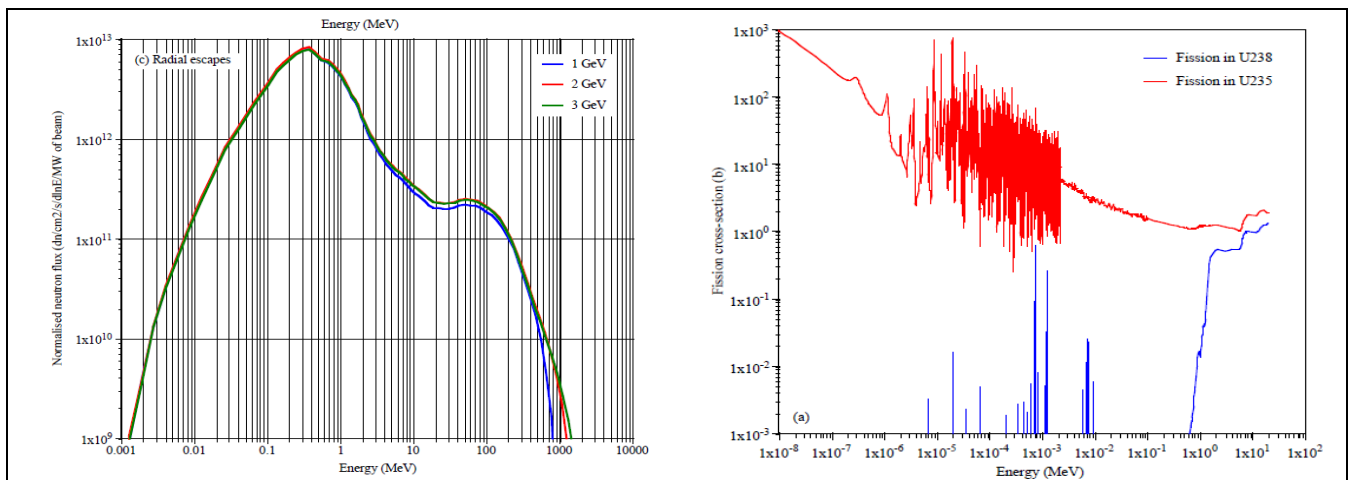
Figure 5: Neutron spectrum exiting radially (left) and U238/235 fission cross-section [Ref3]

The escaping neutron spectrum is dominated by evaporation neutrons having undergone some moderation (peak at ~300 keV); there is also a significant component of neutrons with energies greater than 100 MeV, especially in the forward direction, due to direct knock-out interactions between the primary protons and single nucleons (intra nuclear cascade).

Although the gain in fission rate by using natural uranium instead of pure U-238 is rather small (i.e. 11%), in the case of a reflected system where the escaping neutrons are bounced back by the reflector at a lower energy, the effect of the small U-235 fraction in natural uranium may be significant. On these premises, there may be several geometrical configurations for the fissile target (most probably, UCx). A first approach may be to place the fissile material around the target, in order to use the maximum number of neutrons (higher fluxes) to produce fission. Therefore, to maximise the efficiency of the neutron-to-proton converter and increase the absolute fission rates, the fissile target should also be placed around the spallation neutron source.

Mercury has been up to this point the proposed material for proton-to-neutron conversion, due to its high neutron yields and convenient thermo-mechanical properties (liquid at ambient temperature and high density). However, other target materials are possible. In particular, the use of lead-bismuth eutectic (henceforth referred to as LBE) should be studied due to its, arguably, more favourable neutronic properties.

The incident proton distributions and overall neutron flux distribution are rather similar for both materials. The most significant discrepancy is obtained by analysing the neutron balance densities which present a net neutron absorbing region in Hg for a radius greater than 12 cm and a length greater than 70 cm, whereas the whole target volume has a positive neutron balance when LBE is used. In other words, no parasitic captures occur in the LBE target (Figure 4 right)

Conservatively, the maximum radius for the target is set at 8 cm and the target length at 60 cm

In the case of LBE, the total (capture + diffusion) cross-section is rather flat, in particular below the keV region. This is due to the dominance of elastic scattering over the other reactions. On the other hand, for Hg in the keV region the total cross-section decreases with $1\sqrt{E}$, since it is dominated by capture.

This implies that the neutron flux below the keV region will be significantly higher in LBE than in Hg due to the reduced number of captures. Above 100 keV, the total cross-sections of both materials are quite similar.
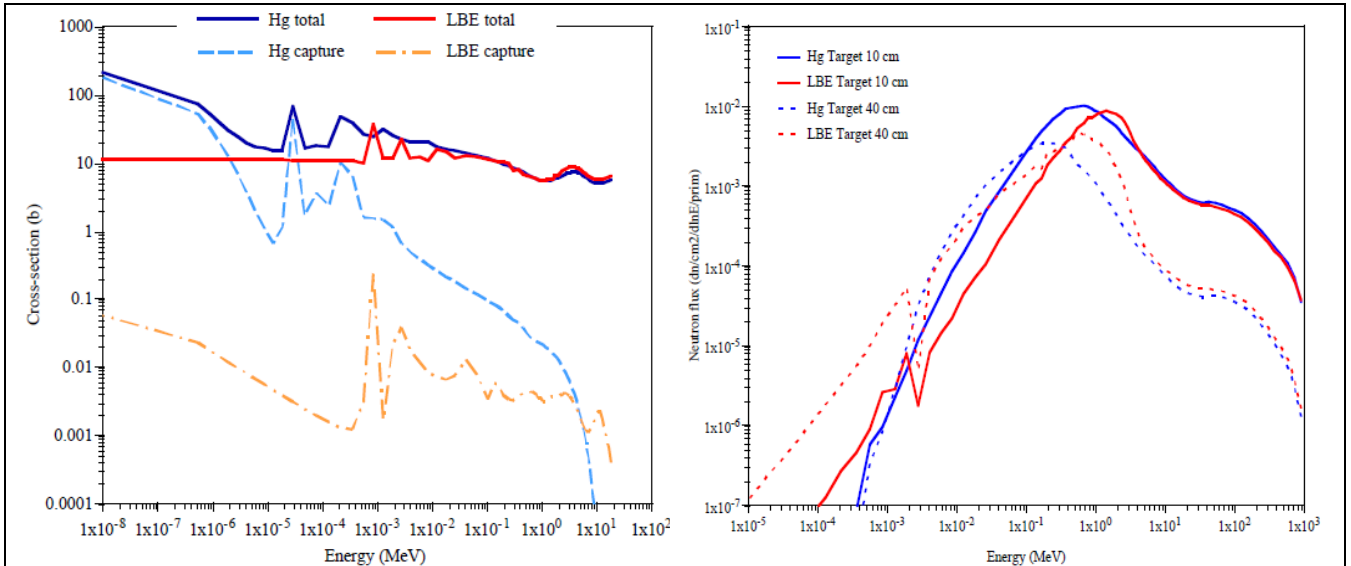
Figure 6: Neutron cross-section of LBE and Hg (left). Resulting spectra in LBE vs. Hg (right) [Ref3]

The high capture of Hg does offer one advantage which is not present with LBE. In the case of a pulsed beam, a bunch of delayed neutrons follows roughly 10^{-5} seconds after the prompt neutrons which are emitted within 10^{-17} seconds of the proton hitting the target. Because the Hg is so effective at capturing neutrons, the delayed neutrons will be mostly absorbed in the target which implies that the pulse of neutrons produced by the proton beam will be very sharp in the case of Hg. On the contrary with LBE the delayed neutrons arriving "on the heels" of the prompt neutrons will not be absorbed in the target but, on contrary, will come flying out and "smudge" the neutron pulse, thus reducing the precision of the time of flight experiments.

1.3.4 Study of the shape of the target

There are other parameters governing the efficiency of the facility beyond those studied in the previous sections. The actual geometric shape of the target also has a bearing on how many fissions are generated per incoming proton. The two main possibilities, shown below in Figure 7, are either a cylindrical converter target surrounded by a cylindrical fission target or a rectangular slab geometry with fission boxes arranged tightly either side of the narrowest dimension of the slab.
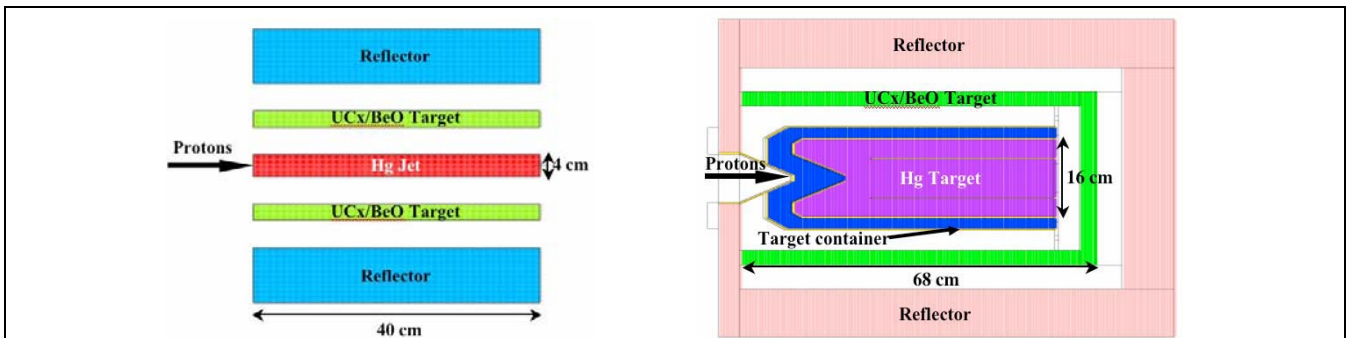
Figure 7:Two types of targets; slab (left) and cylindrical (right) [Ref4]

A cylindrical target

The previous considerations lead to a "best possible" shape for the cylindrical converter target which is a coaxially impacted by a 1 GeV proton beam. The main dimensions are as follows;

o   Diameter < 16 cm

o   Length > 60 cm

The target material may be either Mercury or LBE from a physics point of view for a continuous pulse. A mercury target shall be preferred for a pulsed target.

Slab Target

It is possible to increase the neutron yield by sending a narrow beam into a thin target whose narrowest dimension will lead to a shorter escape route for neutrons thus increasing the neutron yield in that transverse direction. In this manner, the fission target is closer to the neutron source and the neutron energy spectrum is much harder which offers interesting perspectives in particular for fission targets with a higher content of U238.

Some streaming of primary particles into the fission targets can be observed in the slab target on the right of Figure 8, an effect of the very narrow dimensions transverse to the beam. This may lead to damage in the adjoining structures as these charged particles can deposit a great deal of heat and cause a significant dpa. The cylindrical target on the other hand manages to contain most of the charged primaries within its bounds.
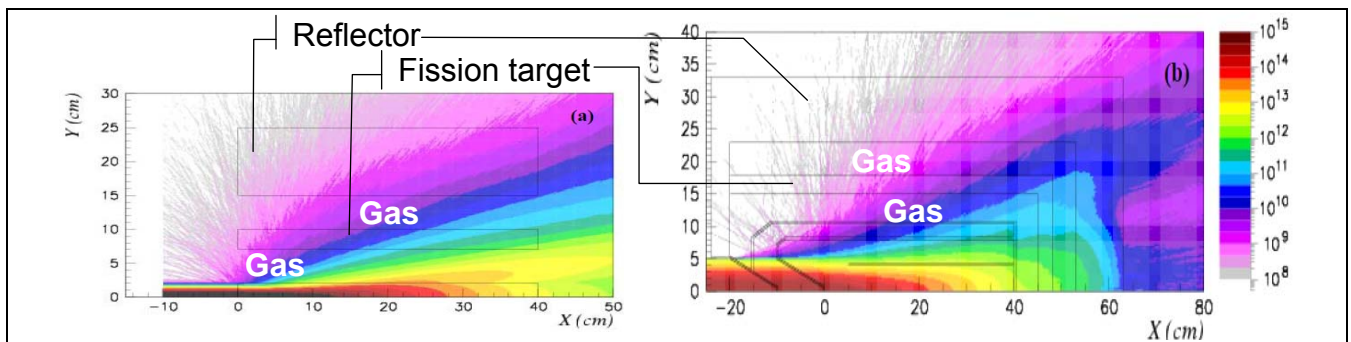
Figure 8: Primary proton flux distribution (primaries/cm2/s/MW of beam) on slab target (left) and cylindrical target (right) [Ref4]

All targets present a significant neutron flux close to values associated with nuclear reactors. For the cylindrical configuration, the neutron flux reaches ~10^{14} neutrons/cm^2/s/MW of beam. The escapes could be further reduced by increasing the reflector thickness. For the Hg jet design, the neutron flux is four times higher in the fission target and presents a more anisotropic distribution, with important neutron escapes both in the front cap (backscattering problems, such as the activation of the beam line) and end cap, as illustrated in Figure 9.
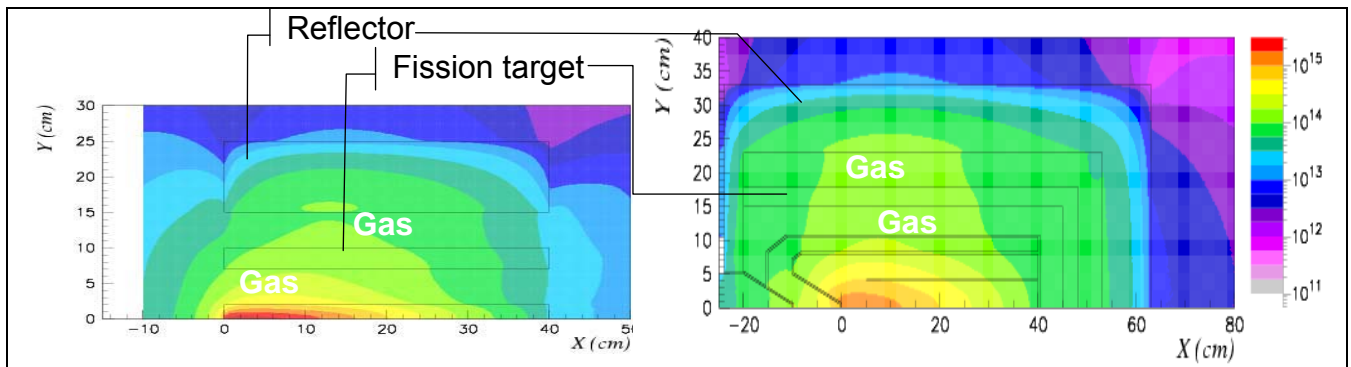
Figure 9: Neutron flux distribution (n /cm^2 /s/ MW of beam) on slab target (left) and 16cm diameter cylindrical target (right) [Ref4]
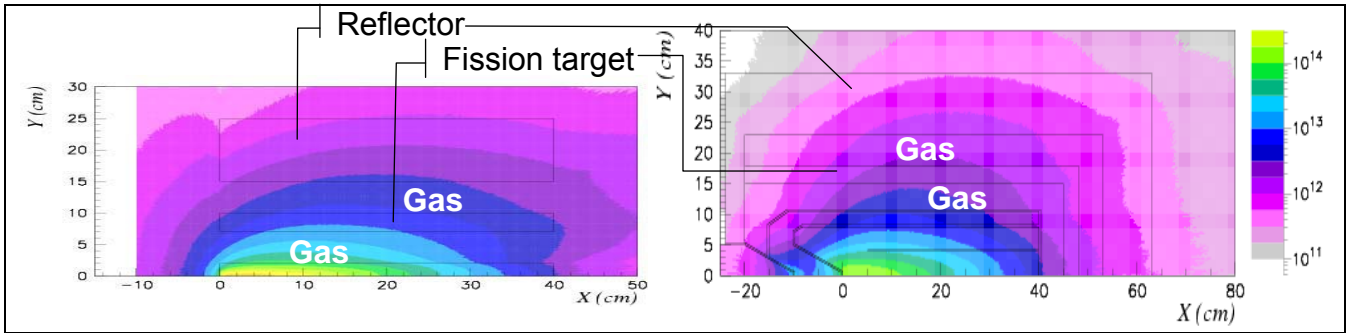
Figure 10: High-energy neutron flux distribution (n /cm^2 /s /MW of beam) on slab target (left) and 16cm diameter cylindrical target (right) [Ref4]

Of particular interest is the high energy end of the spectrum; Figure 11, left shows the flux exiting the Hg jet has a peak energy between 1 and 2 MeV and is significantly harder than in the other two cases, where the peak energies are 300 keV and 700 keV. The large high-energy component of the neutron flux has a negative impact in terms of radioprotection and structural damage, deteriorating mechanical properties of the structure. This is clearly shown in the spatial distribution of the high-energy neutrons in Figure 10, where very small fluxes escape the reflector in the cylindrical configuration, compared to those streaming from the Hg jet design, which is at least one order of magnitude higher.
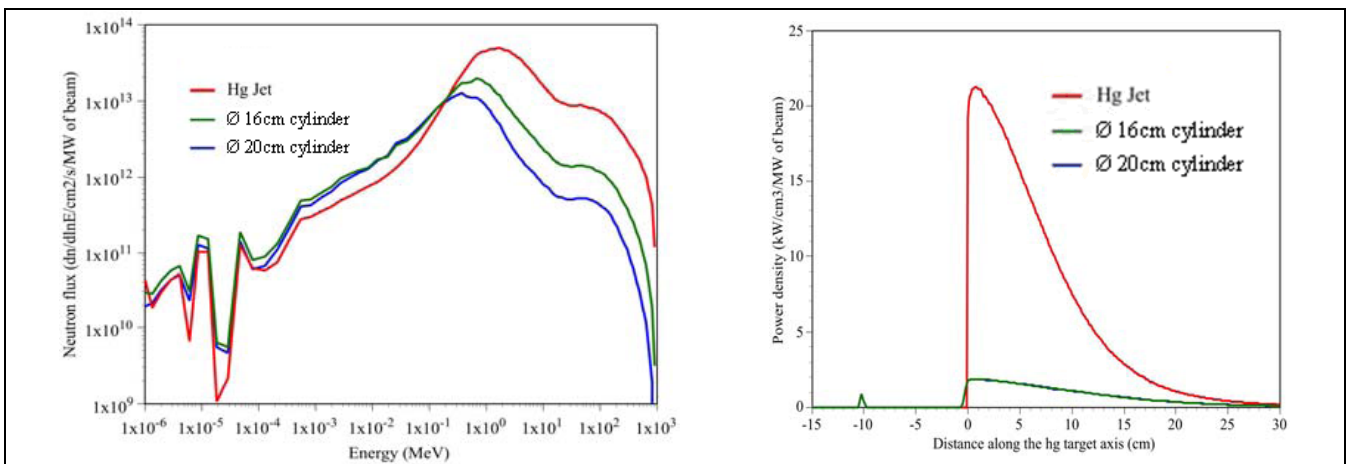
Figure 11: Neutron spectrum in dn /dlnE /cm^2 /s /MW of beam (left) and power deposition in kW /cm^3 /MW of beam along beam axis (right) for cylindrical and slab targets [Ref4]

The energy deposition in the beam window may be another source of problems due to thermally-induced stresses. The maximum power density of ~1 kW /cm^3 /MW of beam in the window of the cylindrical target implies detailed design studies are required to address the cooling of the window. Conversely, power densities in the Hg jet design reach ~22 kW/cm3/MW of beam, requiring very large Hg flows to avoid vaporisation.

1.4 Isotopic yield

Of great interest is the yield of rare isotopes in the fission targets and this depends to a large extent on increasing the number of fissions. Indeed the chances of witnessing the appearance of a short-lived isotope close to the edges of the valley of stability are much greater if the overall number of hadronic reactions is increased.

The jet shows a superior yield for a fission target made of natural uranium (99.3% U238, 0.7% U235) due to the harder spectrum which favours fast fission of U238 in the rapid domain (cf. fission section in Figure 5)
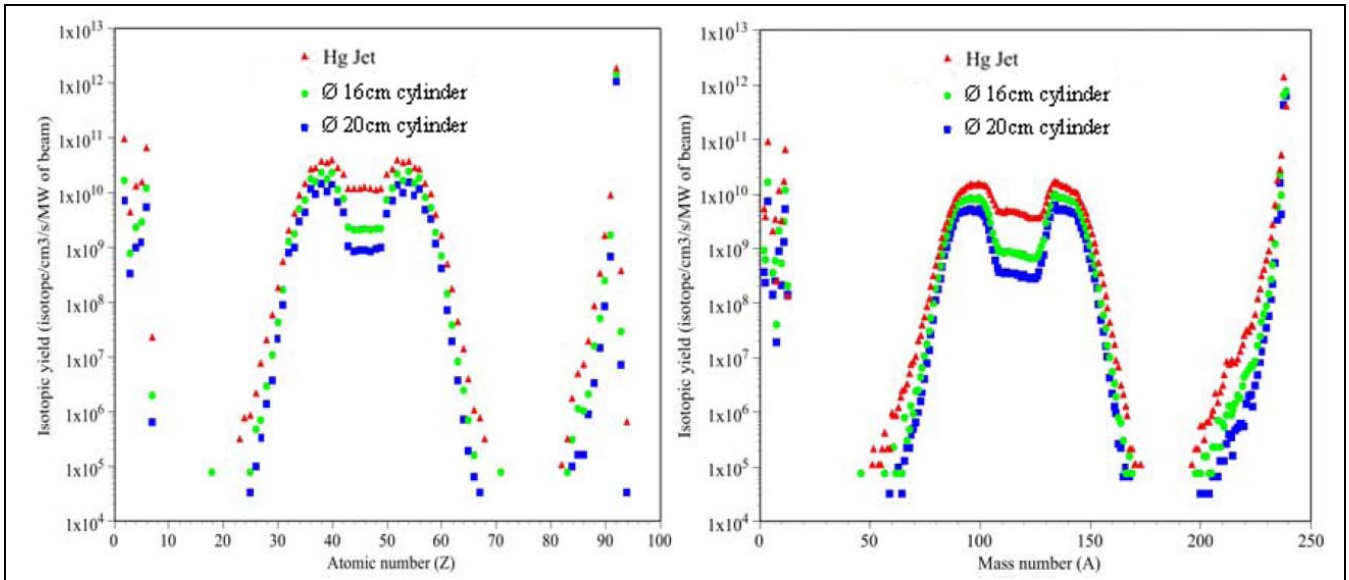
Figure 12: Isotopic yield in Isotope /cm^3 /s /MW of beam according to Element (left) and mass (right) [Ref4]

1.5 Safety aspects

Two main concerns governing the safety of the planned facility are :

- o Radio toxicity

- o Chemical toxicity

The radio-toxic content of the two options for the liquid metals being considered were the subject of theoretical studies with codes such as FLUKA for recording the instant inventory and associated decay simulations, but also the results of experimental investigations in [Ref18] such as the Megapie post-irradiation test and the sub-scale chemical test of a proton-irradiated mercury sample in [Ref13]

Mercury toxicity:

The radiotoxic content taken from a sample is shown below in Table 2. No detailed information on irradiation conditions was available but in the ISOLDE facility it was subjected to a total of approximately 10^{18} protons at an energy of 1 GeV.

Nuclide	Half life [d]	Activity [Bq]
^{102}Rh	207	3.9
^{102m}Rh	~1000	1.3
^{110m}Ag	249.79	0.9
^{133}Ba	3836.15	3.4
^{143}Pm	265	3.2
^{153}Gd	240.4	4.1
^{172}Hf/^{172}Lu	682.5	65
^{173}Lu	500	58
^{194}Hg/^{194}Au	189800	5.1

Table 2: Radio nuclides identified in a proton irradiated mercury sample. [Ref13]

The chemical toxicity of mercury is high and it relatively easy to inhale because of the high vapour pressure. Hence at room temperature precautions must be taken to avoid inhaling vapour by wearing dedicated Hg protective masks and goggles. Direct contact should be also avoided by wearing a full body disposable suit and disposable gloves as vapours will deposit on all surfaces.

The experience at the IPUL mercury lab showed that in order to remain below the 50 μg / m^3 limit deemed acceptable for an 8 hour exposure, it was necessary to clean the lab and ventilate it thoroughly. The effect of temperature is quite clear from the peak occurring after noon. In essence for a continued use of mercury in a dedicated facility, scrubbing the air with filters is necessary, as is high-standard quality control and the utmost care to avoid spillage must be taken. In addition to monitoring the atmosphere, it is also necessary to test workers present on the test loop to check levels of mercury in the blood remain below 10 μg / l.
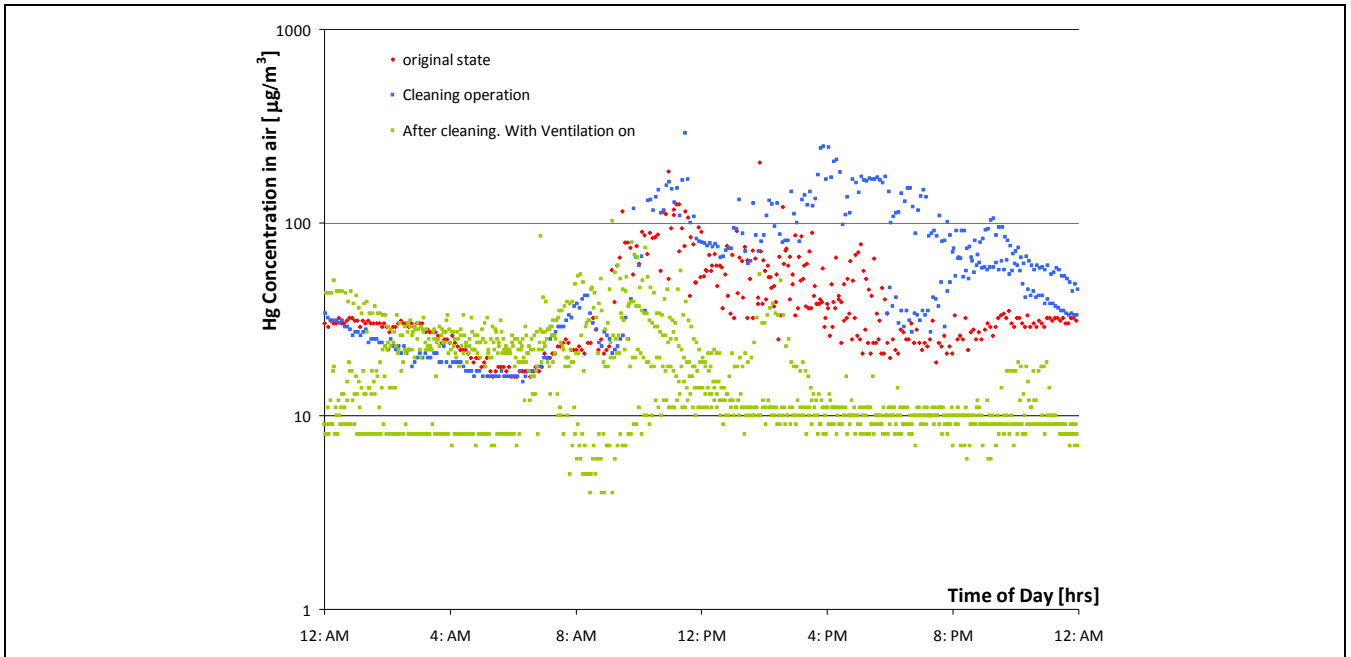
Figure 13: Operational Mercury concentration in the IPUL mercury lab

LBE toxicity:

The radiotoxic content taken from the MEGAPIE irradiation test is shown below in Table 3. The test lasted 4 months at 0.6 GeV/1.3 mA. Content is given for the total target mass of 800 kg.

Time of cooling (days)	Total activity (Bq)	Nuclide, R (%)		Nuclide, R (%)		Nuclide, R (%)		Nuclide, R (%)		Nuclide, R (%)	
0	1.23+16[a]	Pb 203	4.23	Bi 206	3.79	Tl 201	3.50	Tl 200	3.05	Pb 201	2.84
1 min	1.20+16	Pb 203	4.33	Bi 206	3.87	Tl 201	3.57	Tl 200	3.12	Pb 201	2.90
60 min	8.83+15	Pb 203	5.86	Bi 206	5.26	Tl 201	4.87	Tl 200	4.24	Pb 201	3.75
1 d	4.03+15	Bi 206	10.5	Pb 203	10.1	Tl 201	9.36	Bi 205	7.61	Tl 200	7.28
2 d	3.06+15	Bi 206	12.5	Tl 201	10.0	Pb 203	10.0	Bi 205	9.65	Tl 200	6.50
10 d	1.20+15	Bi 205	18.0	Bi 206	14.4	Po 210	6.99	Au 195	6.38	Ir 189	6.26
30 d	5.32+14	Bi 205	18.7	Po 210	14.6	Au 195	13.4	Ir 189	5.36	Bi 206	4.91
60 d	3.08+14	Po 210	21.7	Au 195	20.7	Bi 205	10.1	Os 185	5.97	Re 183	4.57
180 d	1.35+14	Au 195	30.2	Po 210	27.2	Os 185	5.62	H 3	4.66	Bi 207	3.83
1 yr	6.52+13	Au 195	31.4	Po 210	22.3	H 3	9.38	Bi 207	7.84	Tl 204	5.89
2 yr	2.79+13	H 3	20.8	Au 195	18.9	Bi 207	17.9	Tl 204	11.5	Po 210	8.37
10 yr	1.01+13	Bi 207	41.4	H 3	36.4	Tl 204	7.67	Pt 193	6.87	Po 208	1.87
20 yr	6.63+12	Bi 207	51.0	H 3	31.7	Pt 193	9.16	Tl 204	1.99	Hg 194	1.52
100 yr	1.03+12	Bi 207	57.2	Pt 193	19.4	Hg 194	8.64	Au 194	8.64	H 3	2.27
200 yr	2.87+11	Hg 194	26.6	Au 194	26.6	Bi 207	23.2	Pt 193	17.5	Po 209	2.80
1000 yr	4.94+10	Hg 194	44.3	Au 194	44.3	Pb 202	3.79	Tl 202	3.79	Bi 208	1.84
2000 yr	1.44+10	Hg 194	32.0	Au 194	32.0	Pb 202	12.8	Tl 202	12.8	Bi 208	6.30
10000 yr	4.44+09	Pb 202	37.5	Tl 202	37.5	Bi 208	20.1	Nb 94	1.56	Nb 93 m	0.79
20000 yr	3.93+09	Pb 202	37.1	Tl 202	37.1	Bi 208	22.2	Nb 94	1.25	Tc 99	0.49
100000 yr	1.84+09	Bi 208	40.8	Pb 202	27.8	Tl 202	27.8	Pb 205	0.89	Tc 99	0.80
200000 yr	9.56+08	Bi 208	65.2	Pb 202	14.5	Tl 202	14.5	Pb 205	1.71	Tc 99	1.12
1000000 yr	1.72+08	Bi 208	80.4	Pb 205	9.16	Bi 210m	3.19	Tl 206	3.19	Nb 93 m	0.93

Table 3: Radionuclide content from LBE irradiated in the Megapie experiment. [Ref18]

The much-feared Po210 is dominant in the months after irradiation, but diminishes rapidly after 2-3 years. Hence Polonium is essentially a shielding problem during irradiation. It is not however a long-term problem for storage after LBE has been taken out of the facility.

The chemical toxicity of LBE is the same as for ordinary lead. The vapour pressure is not a matter of concern as with Mercury, so there is no risk of inhaling LBE vapours at room temperature. Direct contact can be avoided by simply wearing gloves.

1.6 A liquid metal target

The heat deposition rates in the target reach such high values that a solid target would melt if it were not cooled very efficiently. Such effective cooling however requires increasing amounts of water which takes away many of the advantages of spallation by absorbing neutrons, to the point even where the target material would occupy far less volume than the surrounding water needed to evacuate the heat.

Hence in order to cope with the high heat deposition rates in the target, a target material in liquid form is used so that the target material can be pumped rapidly towards a heat exchanger where it can dump its heat more efficiently into a secondary heat exchanger circuit. Thus the spallation zone and the heat removal out of the target are essentially decoupled. In addition the presence of a liquid with a high heat carrying capacity can serve in a window version of the target to cool the window as well.

1.7 Properties of liquid metals considered for the target

The liquids considered for the target were essentially metallic in nature as metals are characterised by a high thermal conductivity. This serves to remove the heat more effectively to the secondary heat exchanger, and also equalises temperature gradients within the liquid thus redistributing efficiently the deposited heat from the beam out of the beam deposition area. The two liquid metals considered in the Eurisol Design Study were :

o   Mercury (Hg)

o   Lead-Bismuth Eutectic (LBE)

Both these metals are characterised by favourable thermal-hydraulic properties (good conductivity, thermal capacity, low viscosity) but are also attractive for producing neutrons by spallation as they are heavy nuclei. Furthermore the capture cross-section for neutrons in these metals is quite low, which enhances their ability to allow escaping neutrons to leave the target unhindered.

Na or Ga on the other hand are also liquid metals with interesting thermal properties which might have been considered, but they lack sufficient atomic mass to produce enough neutrons by spallation.

The properties of the two selected liquid metals is best summed up in the next tables and figures on the following pages of the current section, which relate to all aspects relevant to their possible use in spallation targets.

Property Name	Symbol	Unit	Hg	LBE
Melting temperature	T_{Melt}	C	-40	125
Boiling temperature	T_{Boil}	C	350	1'640
Thermal expansivity	α_{Vol}	1/K	0.00018	0.00012

Table 4: LBE vs. Hg material properties
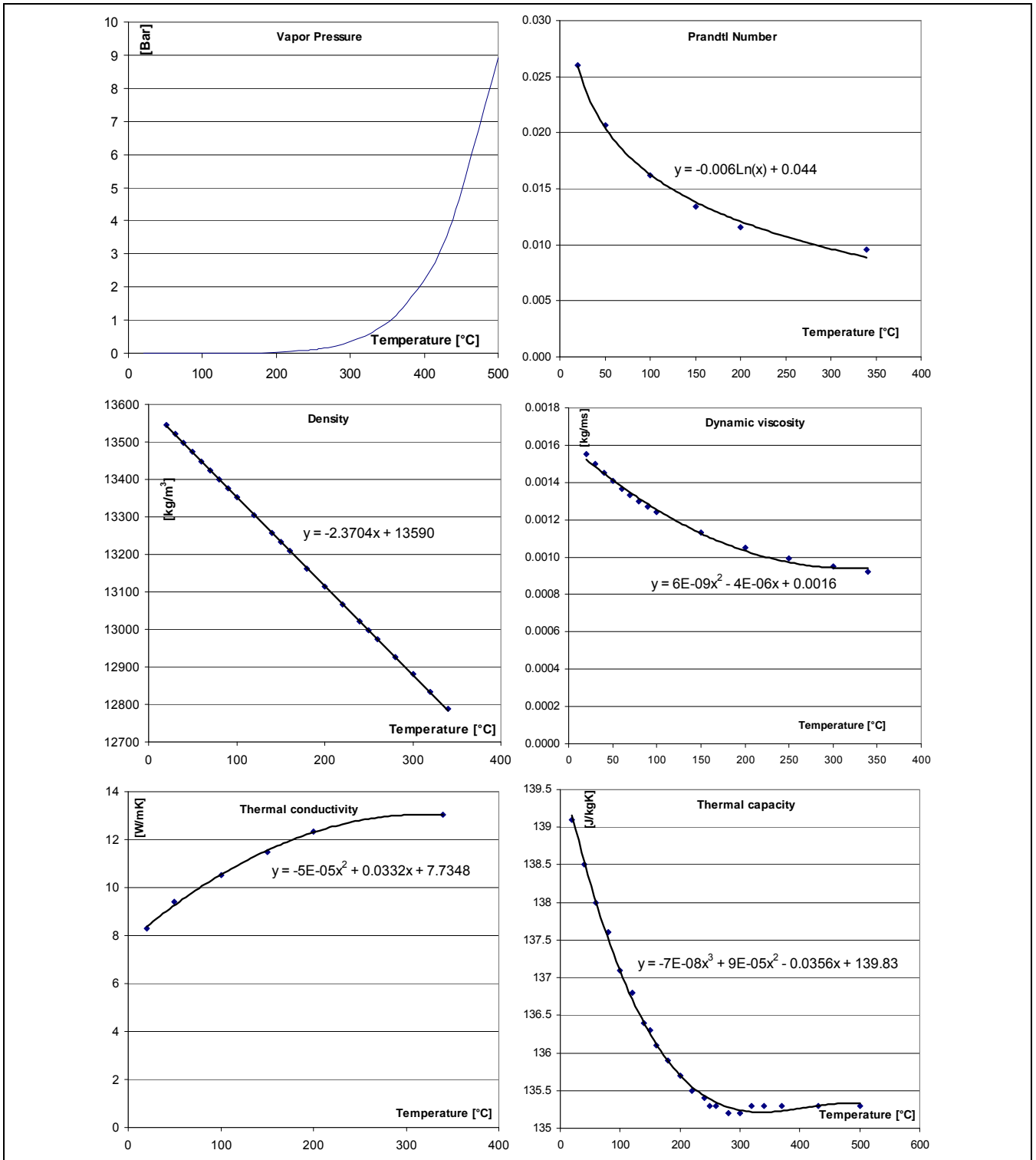
Figure 14: Liquid Material Properties of Hg
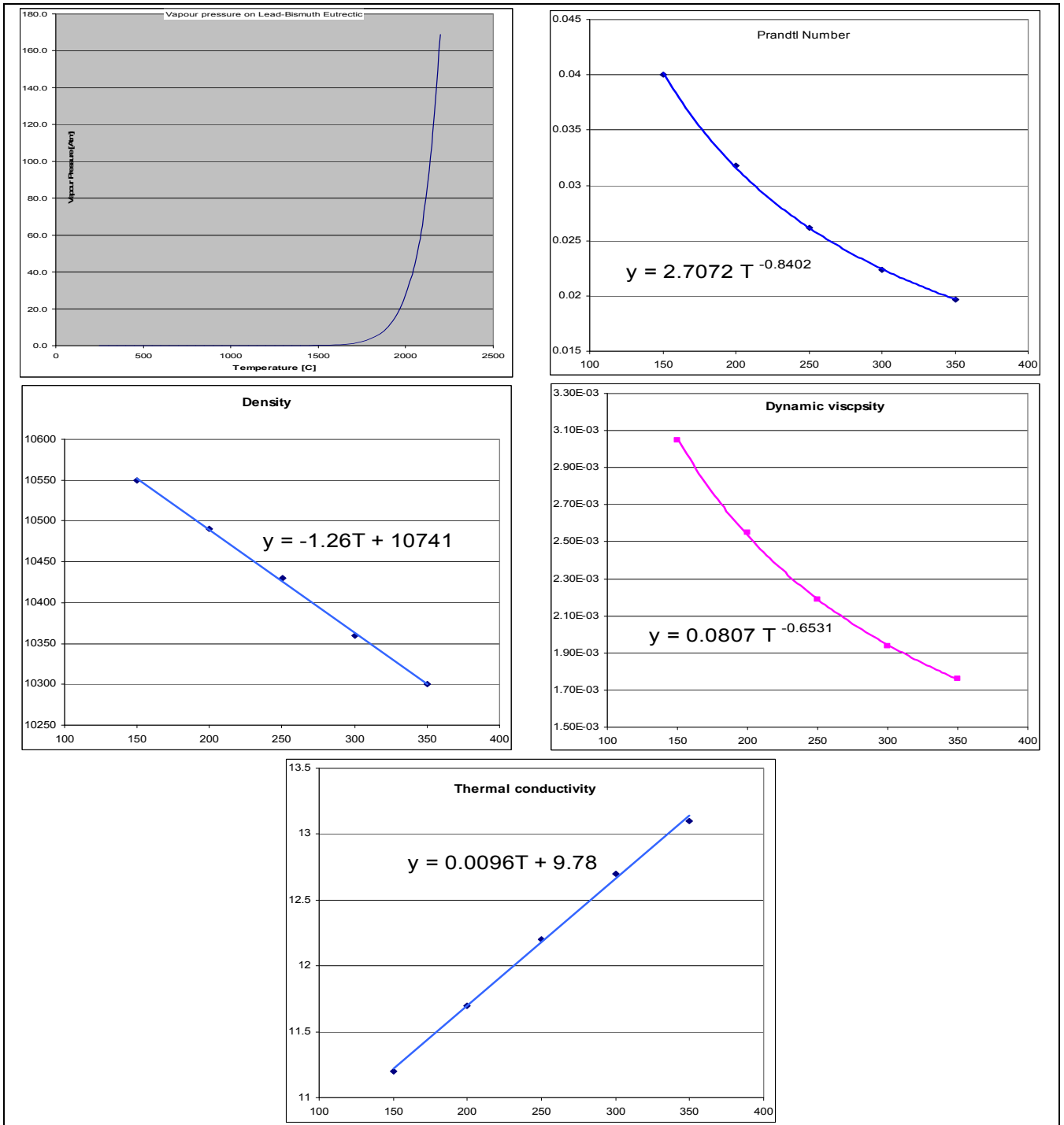
Figure 15: Liquid Material Properties of LBE

The preference for LBE or Mercury is based on an assessment of their suitability in terms of evacuating heat from the target safely, but also their properties with regards to physics performance. The section on target development gives a complete overview of these differing requirements.

1.8 Properties of target structural materials

The structure of the target and surrounding structure is primarily made of stainless steel. Two are of primary importance in the design:

  o Martensitic stainless steel T91 for all highly irradiated components such as the window and target

  o Austenitic stainless steel 316L for less highly irradiated components such as the loop

The reason behind this choice is the experience gathered during the MEGAPIE experiment which highlighted the good resistance to irradiation of T91. 316L on the other fares less well under irradiation but is more readily available and therefore suitable for all other structures.

All steel properties are taken outside irradiation. Irradiation has an effect which is strongly dependent on the dose rate expressed in dpa and causes embrittlement. Therefore the design shall strive to remain in the elastic range which is not influenced significantly by the dose rate. In particular, the first iteration will attempt to remain within the so-called "design strength" which is a fraction of the elastic limit.

1.8.1 Martensitic steel T91

The properties of stainless steel T91 are summarised hereafter from a thermo-structural standpoint.

Young's modulus

Temperature dependency for the stiffness modulus follows the following relations;

$$E \text{ [MPa]} = 207300 - 64.58 \, T \qquad \text{for } 20ºC < T < 500ºC$$
$$E \text{ [MPa]} = 295000 - 240 \, T \qquad \text{for } 500ºC < T < 600ºC$$

T	ºC	20	100	200	300	400	500	600
ρ	kg/m^3	7730	7710	7680	7650	7610	7580	7540

Table 5: Density for T91 austenitic steel, temperature dependency

T	ºC	20	50	100	150	200	250	300	350	400	450	500	550	600
S_m	MPa	193	193	193	193	192	190	187	183	174	163	146	126	101
$R_{p0.2}$	MPa	420	400	375	367	362	359	355	349	338	320	292	254	203
R_m	MPa	580	559	536	525	519	514	506	493	471	439	395	340	273

Table 6: Design, Yield and Ultimate strength for T91 steel, temperature dependency

	N	100	200	400	10^3	$2\ 10^3$	$4\ 10^3$	10^4	$2\ 10^4$	$4\ 10^4$	10^5	$2\ 10^5$	$4\ 10^5$	10^6
$\Delta\varepsilon_t$	%	1.229	0.942	0.743	0.570	0.485	0.425	0.347	0.285	0.242	0.205	0.187	0.174	0.163
$\underline{\Delta\varepsilon}$	%	1.207	0.920	0.722	0.550	0.465	0.406	0.329	0.269	0.227	0.191	0.173	0.160	0.149

Table 7: Admissible plastic and total strain range in fatigue for T91 steel at 20°C

$\Delta\varepsilon_t$ = total uni-axial strain range; $\underline{\Delta\varepsilon}$ = plastic strain range

T	°C	20	100	200	300	400	500	600	700
α_m	10^{-6}/K	10.4	10.8	11.2	11.6	11.9	12.2	12.5	12.7
α_i	10^{-6}/K	10.4	11.1	11.9	12.4	13.0	13.6	13.8	

Table 8: Linear thermal expansion coefficient for T91 austenitic steel, temperature dependency

T	°C	20	50	100	150	200	250	300
c_p	J/kgK	448.85	462.76	484.11	503.92	523.04	542.34	562.69
λ	W/mK	25.9		27.0		28.1		28.8
a	$10^{-6}\ m^2$/s	7.46		7.23		6.99		6.69
T	°C	350	400	450	500	550	600	
c_p	J/kgK	584.94	609.96	638.61	671.75	710.25	754.96	
λ	W/mK		29.2		29.0		28.5	
a	$10^{-6}\ m^2$/s		6.29		5.70		5.01	

Table 9: Thermal properties for T91 austenitic steel, temperature dependency

1.8.2 Austenitic steel 316L

The properties of stainless steel 316L are summarised hereafter from a thermo-structural standpoint.

Young's modulus

Temperature dependency for the stiffness modulus follows the following relations

$$E\ [MPa] = 194000 - 81.4\ T \qquad \text{for } 20°C < T < 700°C$$

T	°C	−157	−129	−73	20	93	204	316
ρ	kg/m^3	8 025	8 016	7 994	7 958	7 925	7 883	7 836
T	°C	427	538	649	760	871	982	
ρ	kg/m3	7 792	7 745	7 698	7 645	7 593	7 543	

Table 10: Density of 316 stainless steel

T	ºC	20	100	150	200	250	300	350	400	450	500	550	600	650
S_m	MPa	115	115	115	108	100	95	90	87	84	80	77	74	71
$R_{p0.2}$	MPa	235	196		159		135	126	120	115	110	106	101	98
R_m	MPa	530	470	430	423	423	423	420	411	388	350	309	530	470

Table 11: Design, Yield and Ultimate strength for 316L steel, temperature dependency

Fatigue deformation admissible [%]	Temperature [°C]							
	20	425	450	475	500	525	550	650
10^3 cycles	0.818	0.711	0.499	0.344	0.236	0.161	0.129	0.129
10^4 cycles	0.403	0.376	0.278	0.205	0.150	0.110	0.0922	0.0922
10^5 cycles	0.245	0.224	0.171	0.101	0.101	0.077	0.0662	0.0662
10^6 cycles	0.163	0.151	0.118	0.0693	0.0693	0.0482	0.0482	0.0482

Table 12: Admissible total strain range in fatigue for 316L steel at various temperatures

T	ºC	20	50	100	150	200	250	300	350	400	450
α_m	10^{-6}/K	15.9	16.1	16.4	16.7	17.0	17.2	17.5	17.7	17.9	18.1
α_i	10^{-6}/K	15.2	15.7	16.5	17.2	17.8	18.4	18.8	19.2	19.6	20
T	ºC	500	550	600	650	700					
α_m	10^{-6}/K	18.3	18.5	18.7	18.9	19.0					
α_i	10^{-6}/K	20.3	20.7	21	21.5	22					

Table 13: Thermal expansion coefficient of 316 stainless steel:
α_m mean coefficient between 20ºC and α_i instantaneous coefficient at T

T	[°C]	21	38	66	93	121	149	177	204	232	260
λ	[W/mK]	13.3	13.7	14.2	14.5	15.1	15.6	15.9	16.4	17	17.3
Cp	[J/KgK]	452			486				528		
T	[°C]	288	316	343	371	399	427	454	482	510	538
λ	[W/mK]	17.8	18.2	18.5	19	19.4	19.9	20.2	20.8	21.1	21.5
Cp	[J/KgK]		548				565				574
T	[°C]	566	593	621	649	677	704	732	760	788	816
λ	[W/mK]	22	22.3	22.7	23	23.5	23.9	24.2	24.6	24.9	25.3
Cp	[J/KgK]				586				615		649

Table 14: Heat transfer properties of 316 stainless steel

1.9 Retained target concepts

There are two basic designs which correspond to the two layouts derived from the neutronic analysis presented in section 1.3.4. The two designs are henceforth referred to as:

o The Coaxial Guided Stream (CGS) design in which a beam penetrates a cylindrically shaped closed-vessel target in which the flow turns 180° at the beam entry point, thus cooling the container wall at the point of entry, also referred to as the Beam Entry Window (BEW)

o The Window Transverse Film (WTF) design in which a beam passes an uncooled window separating the beam line from the target, and then impacts side-on a falling curtain of liquid metal

These two options are presented schematically in the figure below.
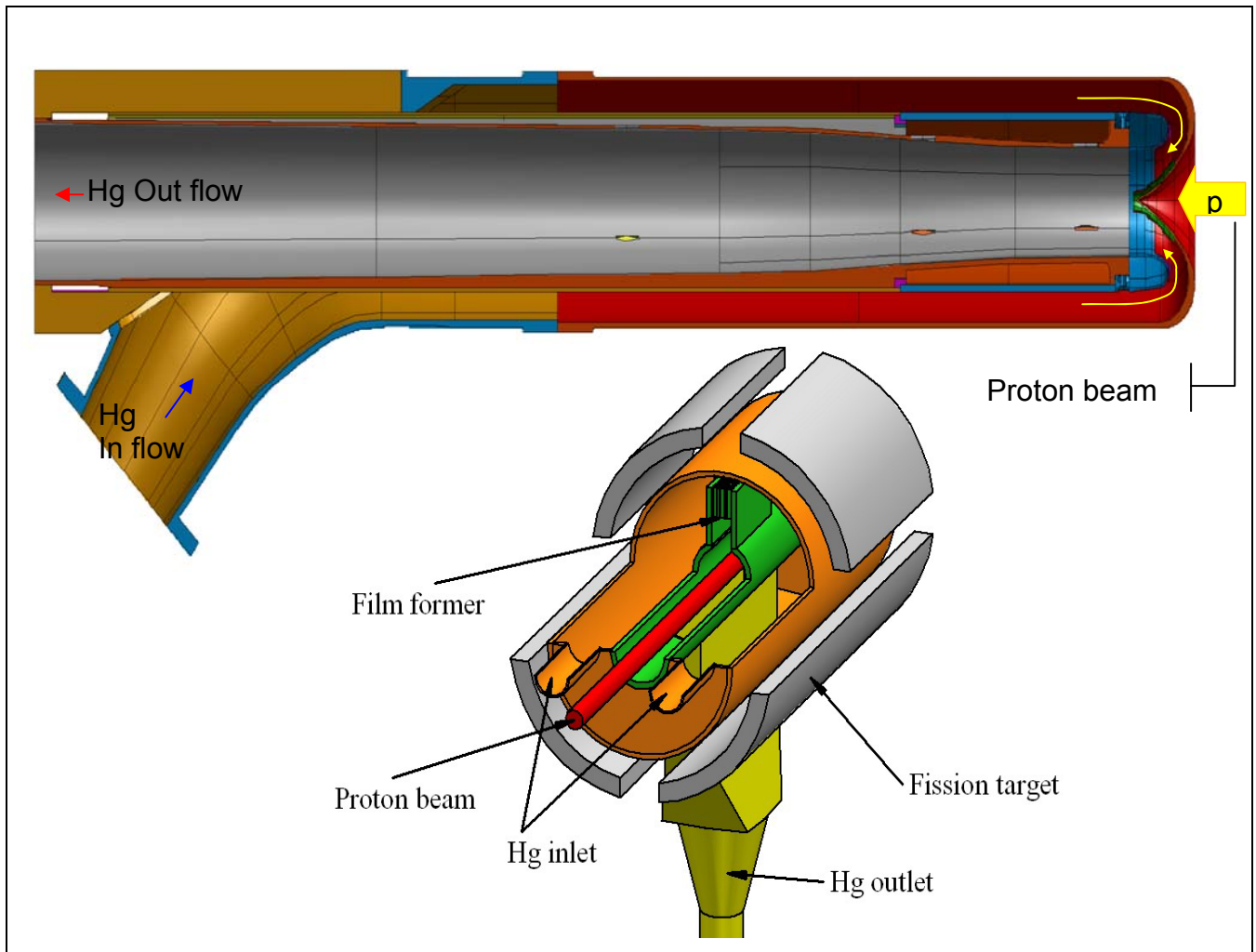
Figure 16: Design variants for the neutron source; CGS design (top, PSI) and film design (bottom, IPUL)

2 The CGS converter target

2.1 Conceptual features of the window design

The basic mode of operation in a liquid metal target with a beam window is to create a rapid flow of liquid metal at the point of entry of the beam into the hull containing the liquid metal, such that the wall when impacted by the beam is simultaneously cooled by the liquid metal rushing past the inner surface.

In Eurisol as in other liquid metal targets in the past, the method for channelling the flow towards the window and away from it is via two concentric channel flows. As depicted in the lower portion of Figure 17, this may be achieved either by channelling the cooler in-flowing liquid metal via the outer annulus or the inner guide tube.

Figure 17, also indicates schematically the section taken through the target for all preliminary iteration steps in driving the best possible shape for the beam-facing part of the target. Other aspects such as the entrance and exit of the liquid metal from back of the target are addressed in a later step with fully three-dimensional models. The stress analysis of the target covers nominal operations. The goal of the initial optimisation was to reduce the stresses under nominal conditions by changing the detail of the window geometry.

Dashed contour indicates location of the axis-symmetric model used in the following section

Two possible flow configurations. flow directed away from the window (left) or towards the window (right)
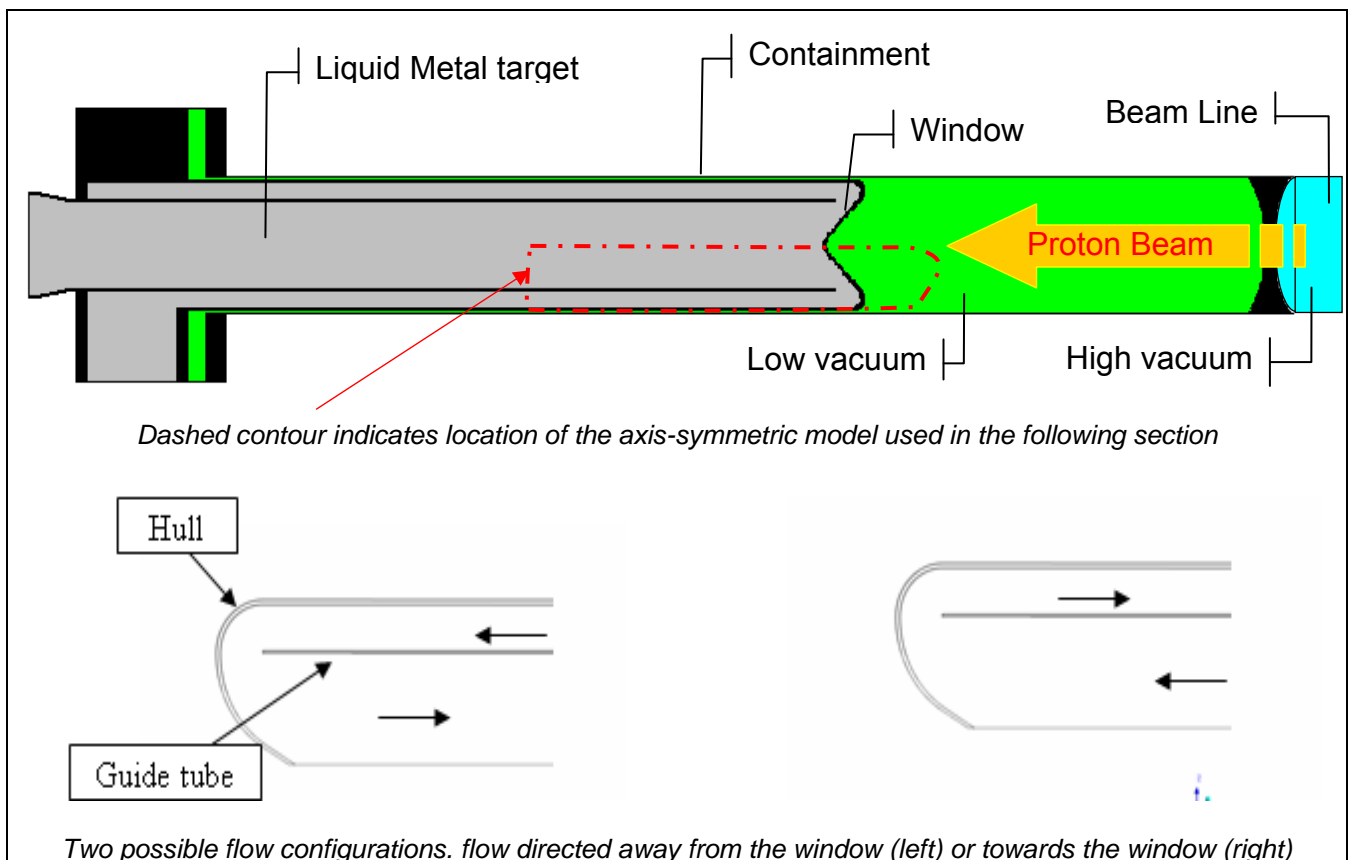
Figure 17: flow conditions investigated with rotationally symmetric model [Ref6]

The model detailed in the next following section used axis-symmetric assumptions for the flow and hence the stress, and concentrated on the main area of interest, i.e. the window as shown in Figure 17, above. The

analysis was carried out using the commercial codes CFX for the thermal hydraulic analysis and ANSYS for the structural analysis.

2.2 Power Deposition and Thermal Hydraulic Design

The most important parameter in designing the target, the heat deposition profile of the proton beam into the EURISOL target, has been calculated under normal operating conditions and compiled in [Ref2]. It was then abstracted in mathematical form in [Ref5] for the target mercury and structural components. The most salient feature of the beam is that it has a narrow Gaussian in profile and its footprint is assumed circular.

The discrete values form the FLUKA code may then be expressed as a mathematical function which is then easier to manipulate in the various thermal-hydraulic and structural codes used to derive an appropriate target design.

For a target beam axis parallel to the z axis, the deposition rate are given taking the reference z=0 as the beam window beam-side surface, or point of entry of the beam into the target and with r the radial distance away from the beam axis.

The total heat deposited in the liquid metal amounts to 2.3 MW of 4 MW total, roughly 60% of the total beam power. The equations to be used for all calculations are given hereafter, for 4 MW of total beam power deposited in the target.

The deposition in the target window is as;

$$q(r) = Q_0 \cdot e^{-\left(\frac{r}{\sigma}\right)^n} \quad \text{W/cm3}$$

The heat deposition in the liquid metal is approximated as;

$$p(r,z) = f(z) \cdot e^{-\left(\frac{r}{\sigma(z)}\right)^{n(z)}} \quad \text{[W/cm}^3\text{] for } 0 < z \le 40cm \quad and \quad \forall r$$

$$p(r,z) = P \cdot p_0 \cdot \ln(c_2) \cdot e^{-\left(\frac{r}{s_0}\right)^{n0}} \quad \text{[W/cm}^3\text{] for } z \le 0 \quad and \quad \forall r$$

$$p(r,z) = 0 \quad \text{[W/cm}^3\text{] for } z > 40cm \quad and \quad$$

With,

$$f(z) = P \cdot (p_4 z^4 + p_3 z^3 + p_2 z^2 + p_1 z + p_0)$$

$$\sigma(z) = s_4 z^4 + s_3 z^3 + s_2 z^2 + s_1 z + s_0$$

$$n(z) = n_2 z^2 + n_1 z + n_0$$

The resulting deposition profile represented in three dimensions:

Heat deposition in r-Z space

Beam entrance
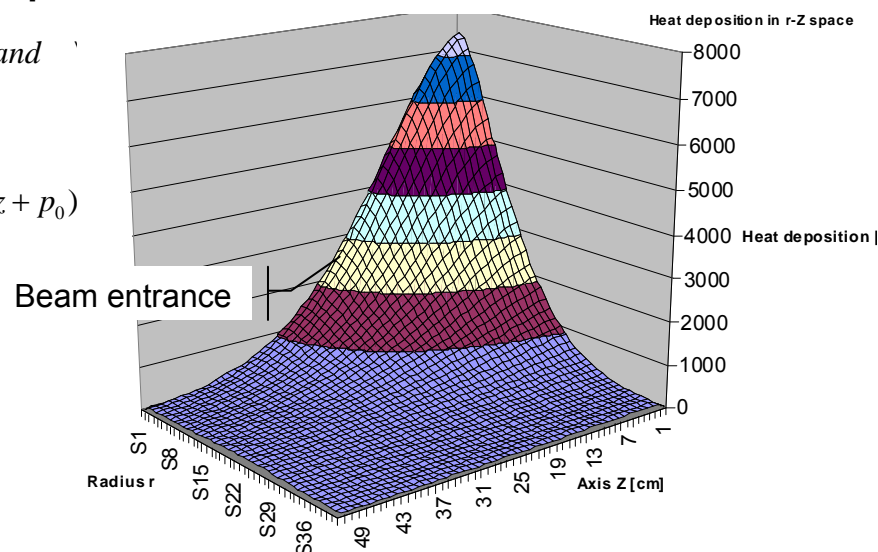
The parameters to be used in the equations above have been calculated for a steel window and mercury for the target liquid metal for two sizes of the beam.

$\sigma = 15$ [mm]				
P 3500 [W/cm³]				
p_0 0.9934 [-]	p_1 0.00042 [cm⁻¹]	p_2 0.001747 [cm⁻²]	p_3 -0.000146 [cm⁻³]	p_4 2.47E-06 [cm⁻⁴]
c_1 3 [cm⁻¹]	c_2 8 [-]	c_3 -0.112 [cm⁻¹]		
s_0 2.011 [cm]	s_1 -0.01714 [-]	s_2 0.001731 [cm⁻¹]	s_3 -3.5E-06 [cm⁻²]	s_4 1.06E-06 [cm⁻³]
n_0 1.6958 [-]	n_1 -0.02083 [cm⁻¹]	n_2 0.000357 [cm⁻²]		
$\sigma = 25$ [mm]				
P 980 [W/cm³]				
p_0 1.0368 [-]	p_1 -0.026981 [cm⁻¹]	p_2 0.005623 [cm⁻²]	p_3 -0.000279 [cm⁻³]	p_4 3.8795E-6 [cm⁻⁴]
c_1 20 [cm⁻¹]	c_2 20 [-]	c_3 -0.11 [cm⁻¹]		
s_0 3.1811 [cm]	s_1 -0.070335 [-]	s_2 0.005992 [cm⁻¹]	s_3 -1.5455E-4 [cm⁻²]	s_4 2.7273E-6 [cm⁻³]
n_0 1.7625 [-]	n_1 -0.022976 [cm⁻¹]	n_2 0.00069 [cm⁻²]		

Table 15: Beam parameters [Ref4]

For different combinations of materials, the results above can be ratioed according to the density for the window and for the deposition length in the target liquid metal as a first approximation.

2.3 Optimisation of the target

The optimisation of the target is approached gradually in steps of increasing complexity, starting with the most pressing issue i.e. cooling of the window.

2.3.1 Structural optimisation of the target window cusp under nominal conditions for the σ = 15mm beam

The optimisation of the window starts with a simple axis-symmetric model of the tip of the cusp, using simplified boundary conditions to replicate heating by the **σ = 15mm beam** and cooling by flowing liquid metal. The figure hereafter shows the main parameters used in deriving an optimal shape of the window

T_{Bulk} :The Bulk temperature of the liquid metal wetting the inner surface

α or HTC: associated Heat Transfer coefficient

Radius, Angle, thickness: can be varied independently to modify the shape of the window tip

The thickness distribution along the window from the tip outwards from the beam path should increase from a minimum to a maximum in order to minimise thermal stress. Hereafter, Figure 18 shows the 1st and 3rd principal stresses along the wall for two different configurations in terms of

$(T_{Bulk}, HTC)_{At\ Centre}$
Radius
Angle
Variable thickness
$(T_{Bulk}, HTC)_{At\ Rim}$
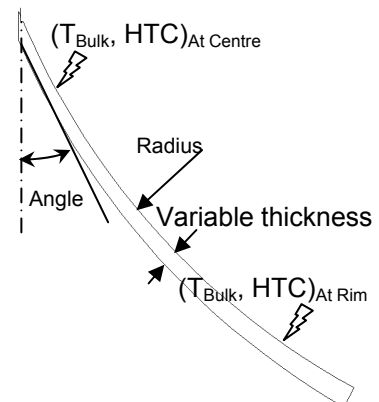
thickness. The thickness of 2mm with 1st (tension) and 3rd (compression) principal stresses of 355MPa and -210MPa respectively can be reduced significantly to stresses of 134MPa and -73Mpa, by reducing the window thickness to 0.8mm overall. This finding is quite significant in that it shows that no matter how strong the cooling from the liquid metal, stress will arise from the temperature gradients thru the thickness.
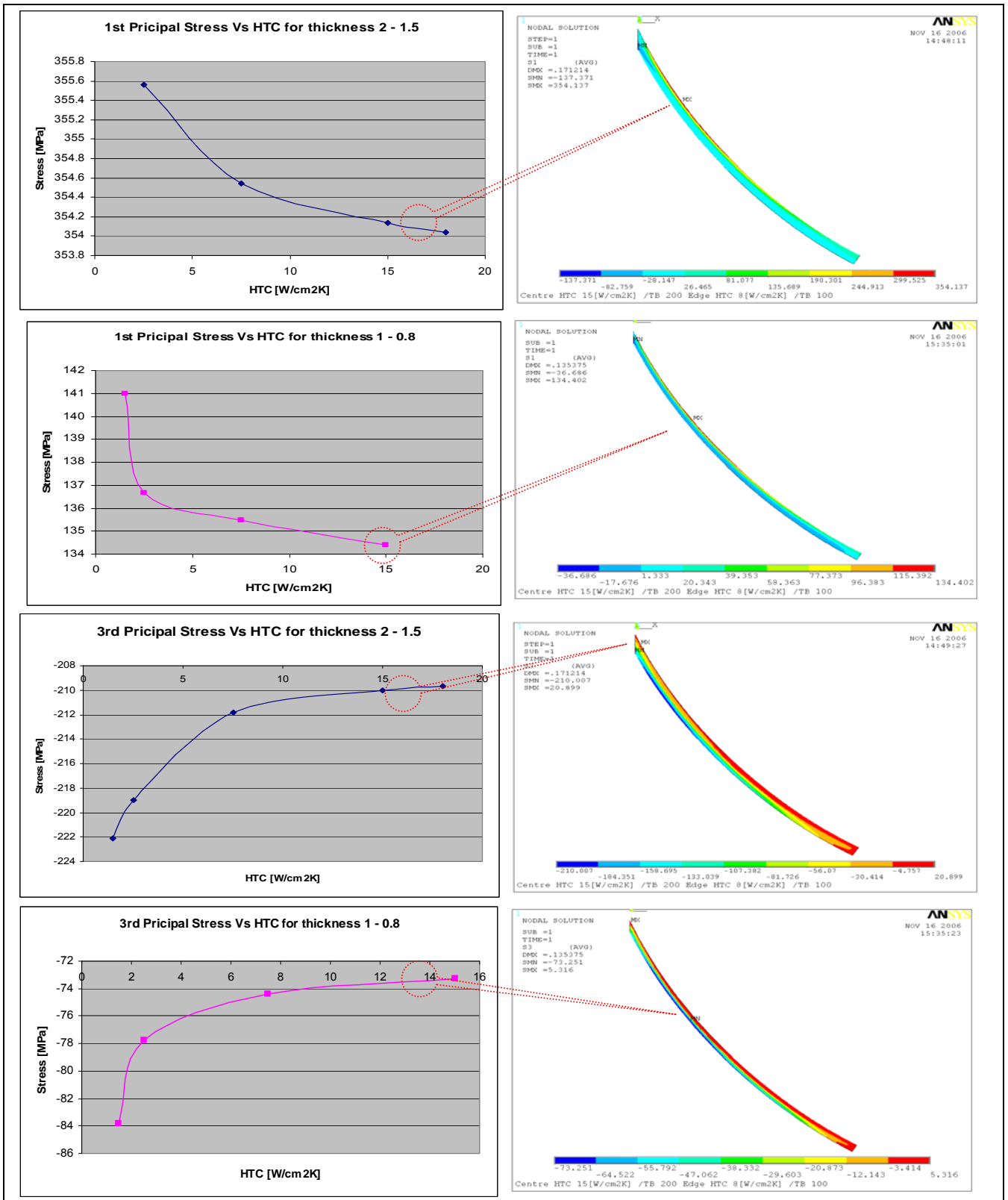
Figure 18: 1st and 3rd Principal stresses results; variable thickness of the window hull [Ref6]

The reduction in thickness should however be kept within bounds, as there could be stability problems due to internal pressure. Hence a taper is used, whereby the thickness along the outer edge of the window is higher than at the centre. Different ratios of centre thickness to edge thickness are studied in the following. Best results are obtained with a thickness of 0.8 [mm] at the centre, and 1-2 [mm] along the edge.

Varying the opening angle of the window tip does not have a significant effect on the stresses along the window hull. This significant finding entails that the angle of the cone may be freely chosen so as to optimise cooling and prevent the formation of recirculation vortices in the fluid. Hence, the best angle will eventually arise out of a subsequent detail CFD calculation.

Changing the radius has a more significant effect. The radius chosen to minimise stress is around 60 [mm]. The effect of increasing the radius starts to taper off after 90 [mm]. Overall the gain in terms of lowering the stress is about 10%. Hence in this case again, the best possible choice of radius will be governed by the CFD calculations, although the radius should remain in a range between 50 and 100 [mm]

Figure 19: Effect of window radius and opening angle on stresses [Ref6]

Thus the best possible shape for the tip of the window cusp from a structural point of view is as follows in order of decreasing importance;

- o a thickness of 0.8 [mm] at the centre, and 1-2 [mm] along the edge

- o the radius should remain in a range between 50 and 100 [mm]

- o An angle greater than 60°

Next, these structural constraints must be accommodated within an efficient hydraulic design.

2.3.2 Hydraulic optimisation of the target window cusp

Any lower velocity and flow instability along the window have an influence on the cooling efficiency; an estimate of the effect on the wall temperature of the window may be derived using the Subothin correlation for the Heat Transfer Coefficient (HTC) which is based on experimental data.

Velocity [m/s]	HTC [W / m^2 K]
1	6'000
2	10'000
3	13'500
4	17'000
5	20'000

Table 16: Heat Transfer Coefficient as a function of Liquid Metal speed [Ref19]

The speed of the Liquid Metal influences the wall temperature through the HTC. To study the effect on the wall temperature, the previous simple rotationally symmetric model of the window cusp is used. The HTC values given in Table 16 above for different LM speeds are applied as a uniform boundary condition to the cusp inner surface wetted by the Liquid Metal and the resulting temperature and stresses are calculated.
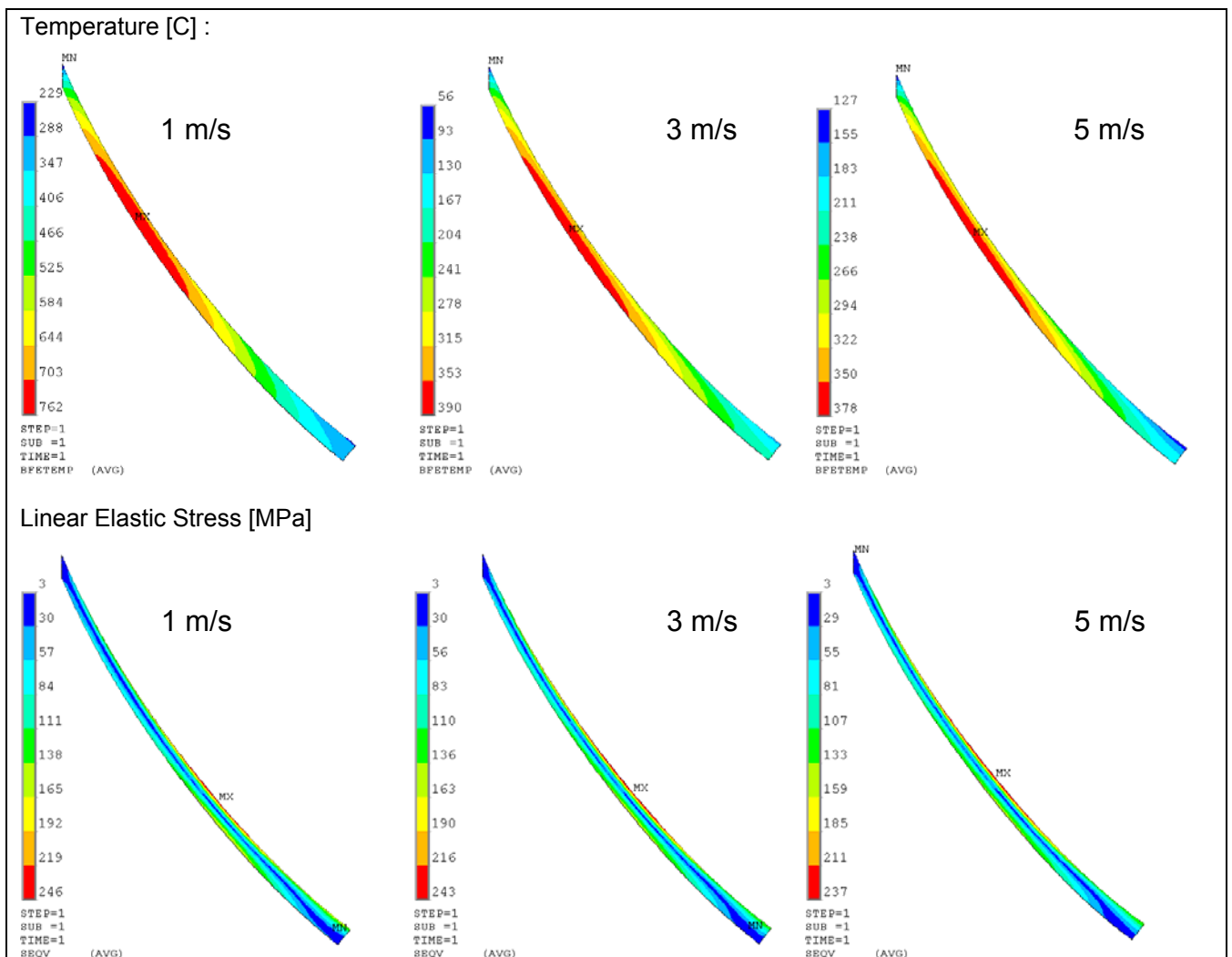
Figure 20: Window Temperature (top) and Von Mises stress (bottom) for different LM speeds [Ref19]

As had been shown previously, the effect of the HTC on the window stresses is not as high as may be feared. However below 1-2 m/s the temperature of the window rises significantly. This has an indirect effect on the stresses as the linear relationship between stress and strain will be affected., Furthermore temperatures above 500 C are not allowable due the sustained irradiation damage on the window which causes embrittlement. From the consideration above, the following requirement must be made on the flow along the window:

o   Liquid metal speed along window > 2 m/s

The next optimisation process focuses on the overall shape of the target at the beam end by taking a rotationally-symmetric cut through the target along its beam length, from the tip to a depth of 40 cm. The CFD package CFX is used and the LES turbulence model which promotes stability at the expense of covering up small instabilities in the flow (more on the subject follows in the next sections).

A first optimisation step is shown hereafter for a straight guide tube. The liquid metal in this instance is mercury with an inlet temperature of 60C. Structural temperatures peak at 370C which is well below the upper limit of 500C. The liquid metal temperature at 267C is approximately 90C below boiling at atmospheric pressure. The peak velocity is quite high for mercury at 6 m/s. Given the flow rate this is unavoidable. Of more concern is the vortex behind the straight incomer tuber which will accumulate heat from the beam and promote structural vibrations.
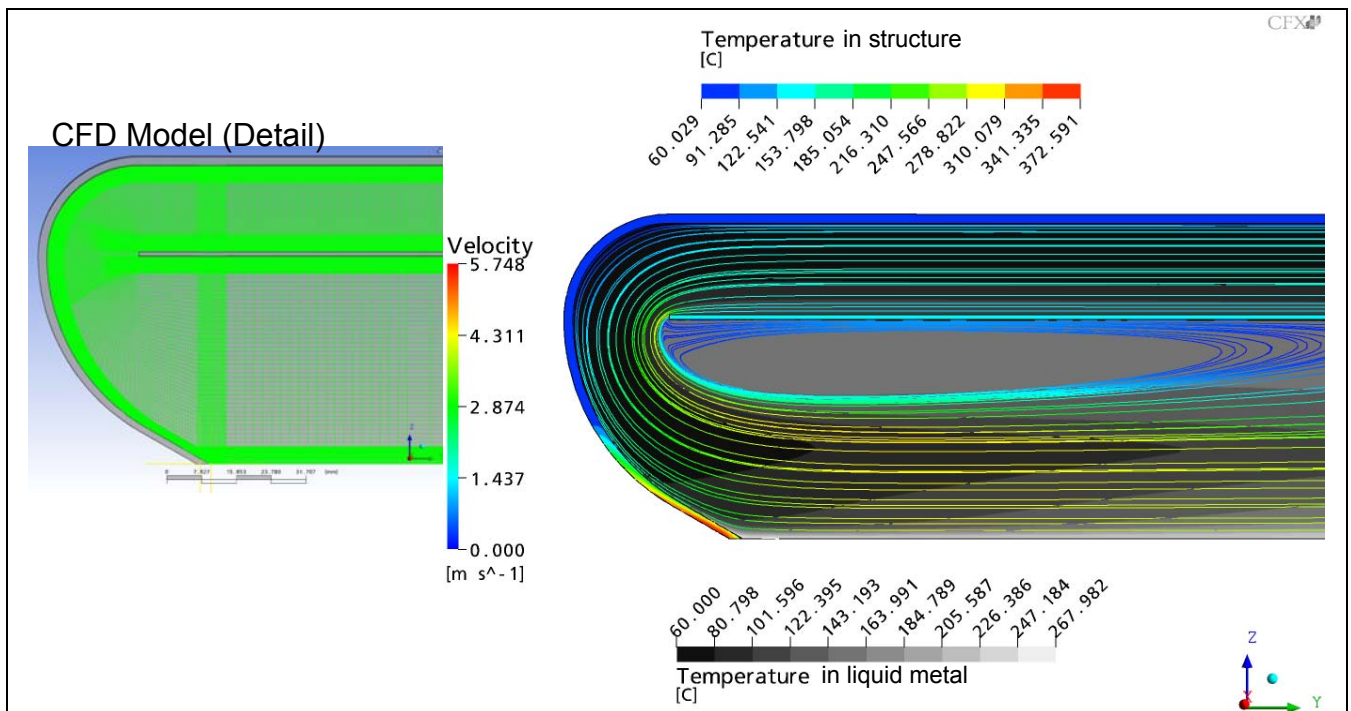
Figure 21: fluid temperature, velocities and hull temperature. Mercury. Outer annular inflow [Ref6]

Before the next iteration step, the possibility shown in Figure 17 of reversing the flow is examined, as this has some attraction is in terms of stabilising the fluid on the window inner surface. The main problem is the far higher temperatures appearing with this counter-flow mode of operation. The mercury peak temperature at 576C is well above the boiling limit of 357C such that the pressure would have to be increased in excess of 10 Bar (cf. Figure 14), an unreasonable value given the constraints which would ensure for the liquid metal loop in terms of leak tightness, sealing etc. Also the window temperature reaches close to 700c, far too high w.r.t. the structural capabilities of T91 steel envisaged for the window (cf. Table 6). The same recirculation vortex appears in reverse on the straight guide tube, evidently the guide tube shape needs to be optimised.
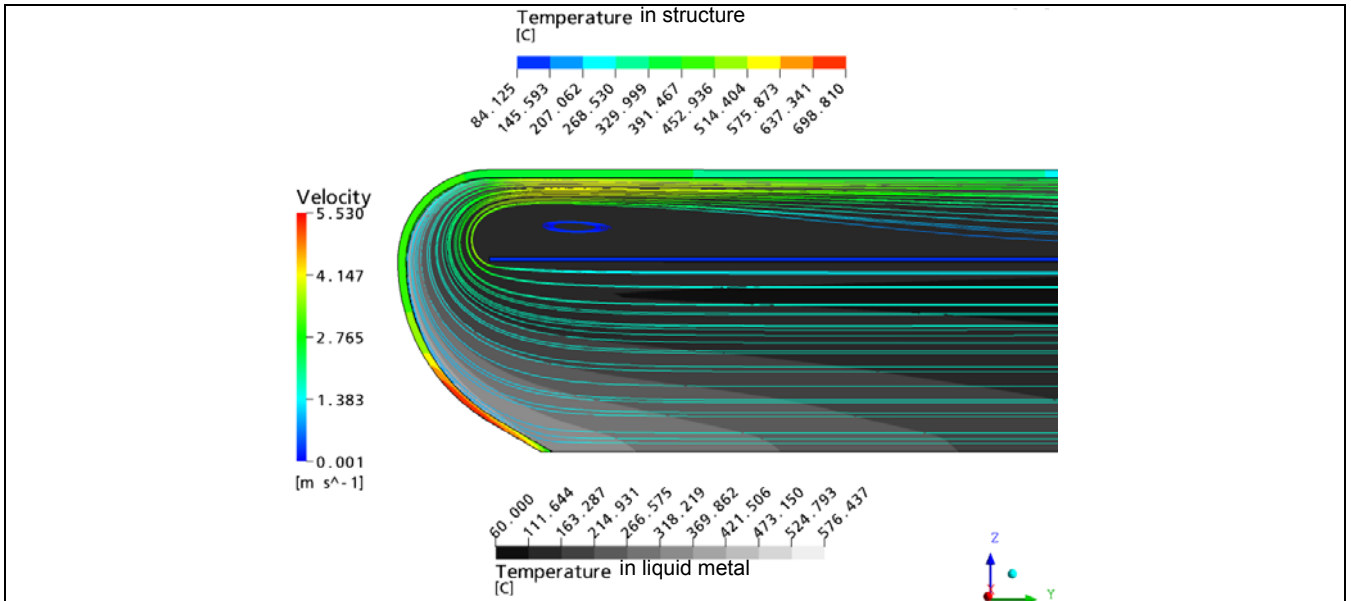
Figure 22: fluid temperature, velocities and hull temperature. Mercury. Inner guide tube inflow [Ref6]

Another attempt to improve flow conditions was examined by the use of LBE entering the target model at 240C, higher than the previous case with mercury because of the need to keep LBE liquid. LBE has the advantage of not boiling at low temperature and remains liquid until well over the melting temperature of stainless steel. As far as the liquid metal temperature is concerned, it remains below boiling point in both flow configurations including the counter-flow where the liquid metal is directed at the window. However the counter flow configuration remains weak structurally because of the very high temperatures in the window. By being less conservative over the concern of LBE freezing, it may be possible to lower the entrance temperature of the LBE by 100C, however this would still not allow the use of T91 steel for the window, as 685C would remains far too high for stressed irradiated stainless steel. The counter-flow option is therefore abandoned.
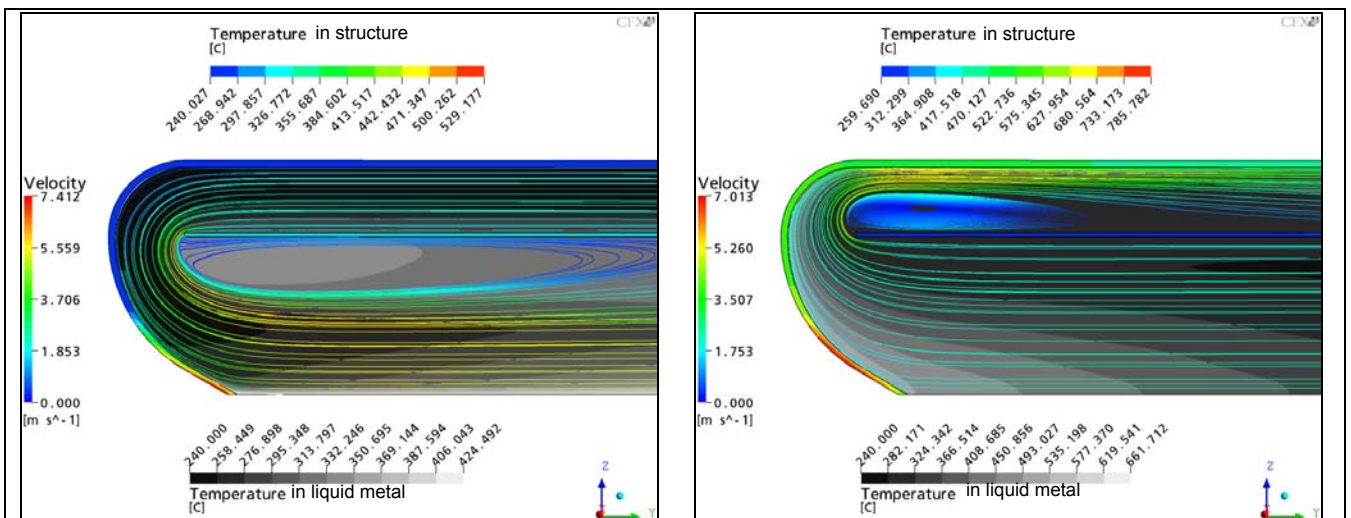
Figure 23: Resulting fluid temperature, velocities and hull temperature with LBE entering via the outer annulus (left) and the inner guide tube (right) [Ref6]

From this point on, project management decided to concentrate only on the mercury option. The reason for this choice were both technical but also in terms of shortening development time. Mercury has some neutronic advantages mentioned in section 1.3 for the pulsed source. But also, the availability of full-scale testing facilities at IPUL with mercury encouraged management to look in that direction so as to be able to test the target concept rapidly.

2.3.3 Hydraulic design of the guide tube

The overall shape of the window is fixed by the previous iteration. The fluid flow inside the target must now be calculated, in order to optimise the duct shape hydraulically, whilst remaining within the geometric constraints imposed by the window optimisation.
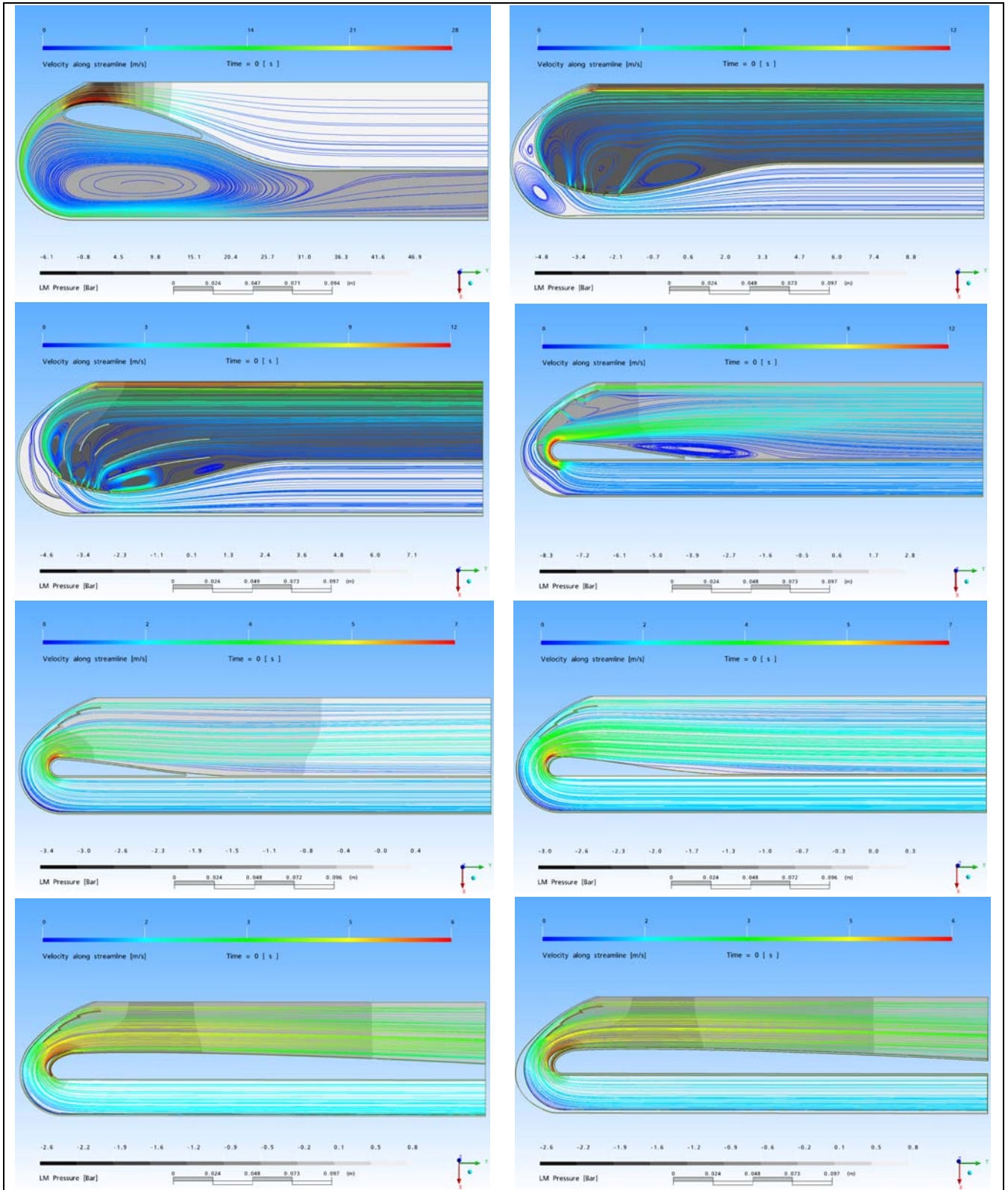
Figure 24: Streamline velocity and pressure drop for various designs [ref7]

The primary objective of the optimisation is to reduce pressure losses whilst ensuring adequate cooling of the structure, preventing boiling of the Mercury and precluding the onset of cavitation along back-swept surfaces. The configuration of the flow may be improved significantly - as described in [Ref7] - by implementing one or several of the following ideas;

- o Aerofoil-type end of guide tube to reduce friction at 180° turn whilst restricting the flow into the window area to increase velocity

- o Cusp-shaped annular blades in the flow to enhance the 180° turn in the flow.

- o Annular Blades along the window to accelerate liquid metal flow and cooling locally.

- o Holes thru the guide tube to destroy recirculation vortices in the main flow, and thus reduce pressure loss and LM heating

In a dedicated study [Ref7], the different configurations shown in Figure 24, under steady-state conditions, were calculated in separate CFD simulations. The optimisation process included several improvements tested independently to gauge their effect in terms of reducing hull stress, temperature, and pressure loses in the LM.

The figures show the most relevant design which yielded some success in terms of achieving the goals set out. The final design is shown in the right hand bottom corner of Figure 24.

The final optimised shape comprises a series of flow vanes on the window to accelerate the flow along the window and encourage cooling. Continuity of the cooling is extremely important to guarantee a constant level of stress and temperature (section 2.3.1).

In addition to the cooling of the window, much attention was spent on the backswept portion of the guide tube to ensure that no recirculation vortex may appear. A flow vane at the forward end of the guide tube was positioned to blow high velocity fluid close to the wall and break up any vortices along this wall.

The derived hydraulic design was seen to be satisfactory in terms of pressure loss with an estimated 0.8 Bar pressure head across the beam end of the target (cf. bottom right hand corner of Figure 24), this does not include pressure losses from the inelt and outlet portion of the target which are not contained in this model

2.3.4 Hydraulic design of the target inlet

In order to connect the outer incomer annulus of the target to a standard piping such as exists in a liquid metal loop is was necessary to find an optimal shape for the inlet. The incoming fluid has to come from the side as the outlet is located coaxially with the beam. Examination of all possible geometries have led to a design in which the incoming fluid enters a diffuser cone which is angled off the main beam axis and forms the transition between the loop piping and the incomer annulus. Such a design was found and is illustrated in Figure 25.
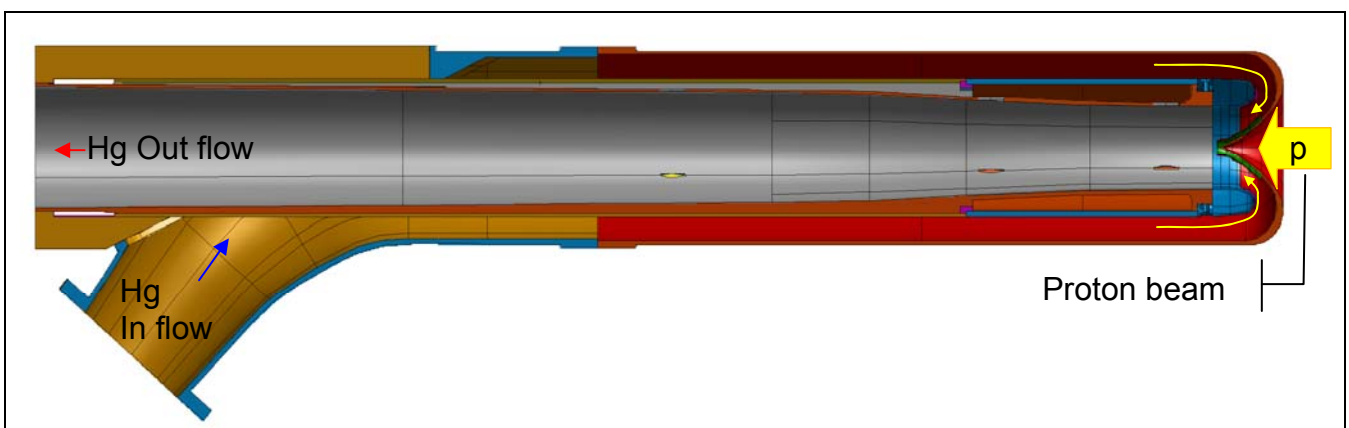
Figure 25: Complete design of the CGS target in section [ref8]

The inlet was modelled in detail in [Ref9] for various conditions of turbulence, the beam window areas was represented by a porous regions with increased friction losses and the model assumed half' symmetry. Figure 26 shows the detail of the model in 3D on the left, and the detail of the mesh seen side-on in the right-hand corner.
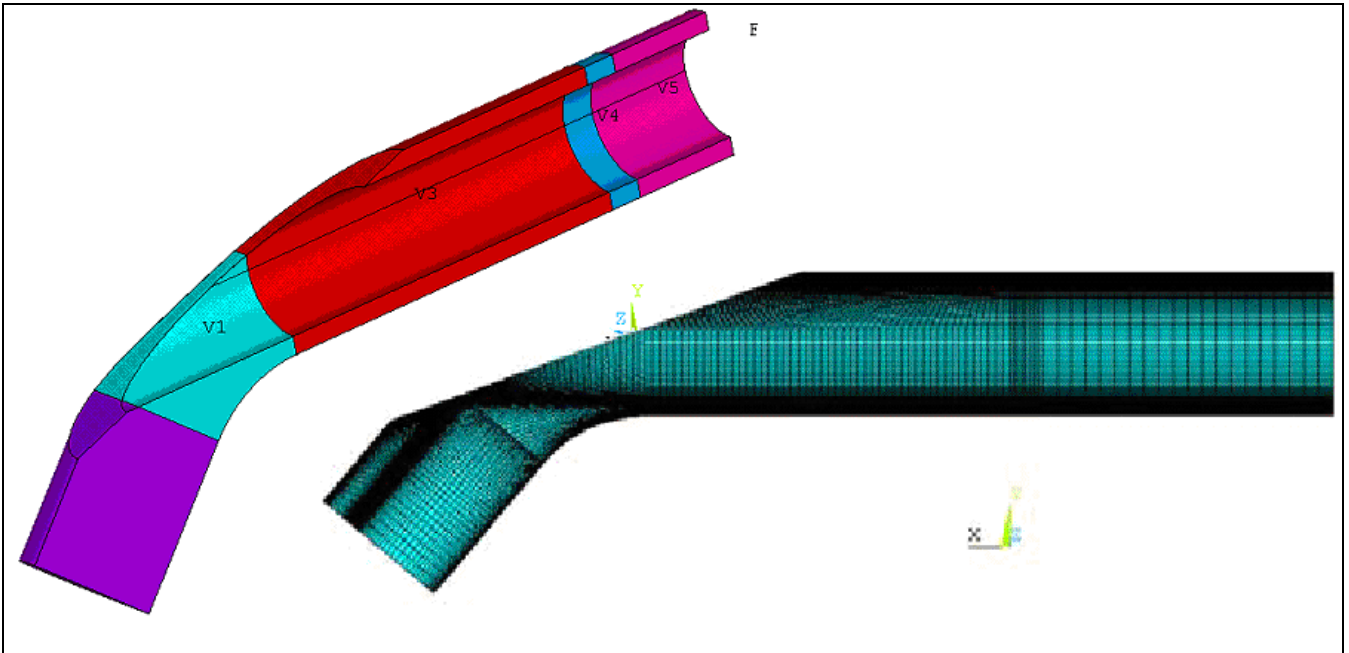
Figure 26: Complete design of the CGS target in section [Ref9]

The computations using a variety of turbulence models (Shear Stress Transfer or k-ε) resulted in a series of predictions for the pressure drop in the inlet and the distribution of flow between the upper and lower portion of the target. The latter was of particular importance to ensure cooling of the beam entrance window as it would be impossible to ensure stable flow over the entire cusp if there were an imbalance at the entrance to the window. Figure 27 shows the overall flow conditions in the inlet with (left) and without (right) a porous region.
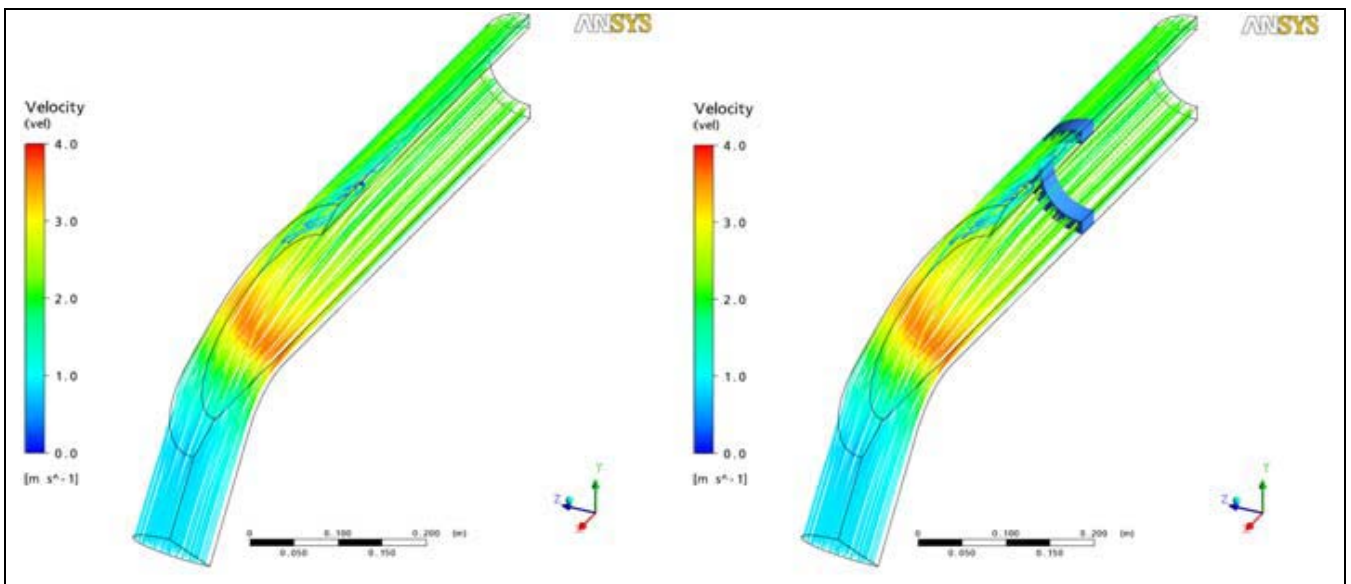
Figure 27: Circulation in the target inlet [Ref9]

The appearance of a vortex at the top of the inlet section was of particular interest, it was found to be stable in all conditions whatever the flow rate, the turbulence model or the downstream porous region friction. The fact

that this vortex does not propagate downstream was again of particular importance to ensuring stable flow conditions over the window.
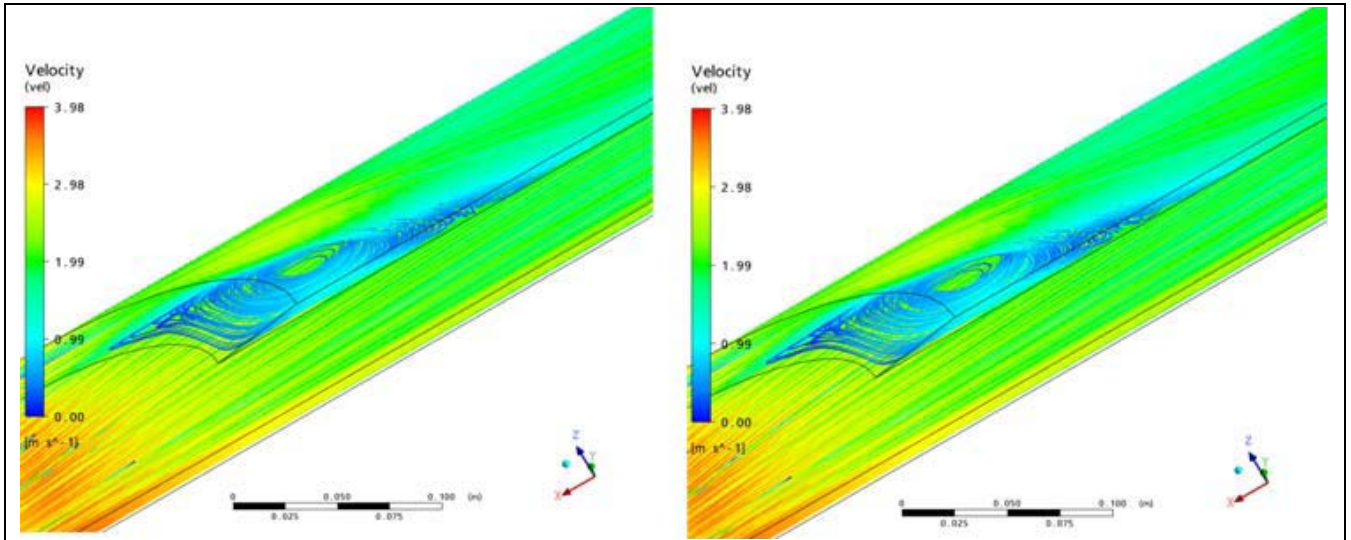
Figure 28: Recirculation vortex at the top of the inlet [Ref9]
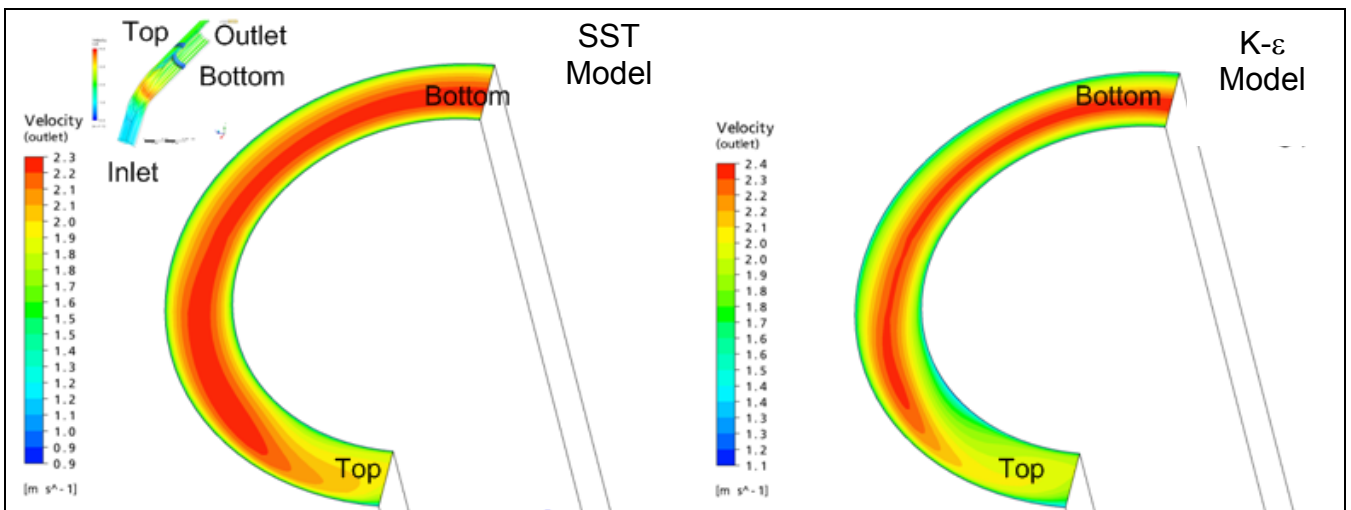
Figure 29: resulting flow distribution across the exit of the inlet (which precedes the window entrance) for different turbulence models [Ref9]

The hydraulic losses through the optimised inlet are quite modest; depending on the chosen turbulence model they do not exceed 0.37 Bar at the full flow rate.

An optimisation process in relation to both thermo-structural considerations and hydraulic constraints has thus resulted in a design of the target which can fulfil all requirements set out in the original parameters listed in Table 1. The next section will set out to verify adequate safety margins exist within the target structure.

2.4 Structural strength of the target

2.4.1 Structural strength of the cusp window

Prior 2D analyses proved that the introduction of thinning the window hull could eventually reduce the stresses in the window. Also, efficiency in cooling the window has been demonstrated by the prior CFD analysis. An axis-symmetric model is therefore set up to examine the effect of the beam on the thus optimised structure; thermal stresses are expected as the beam heat deposition is extremely high. The beam is programmed as mathematical function according to the equations in section 2.2.
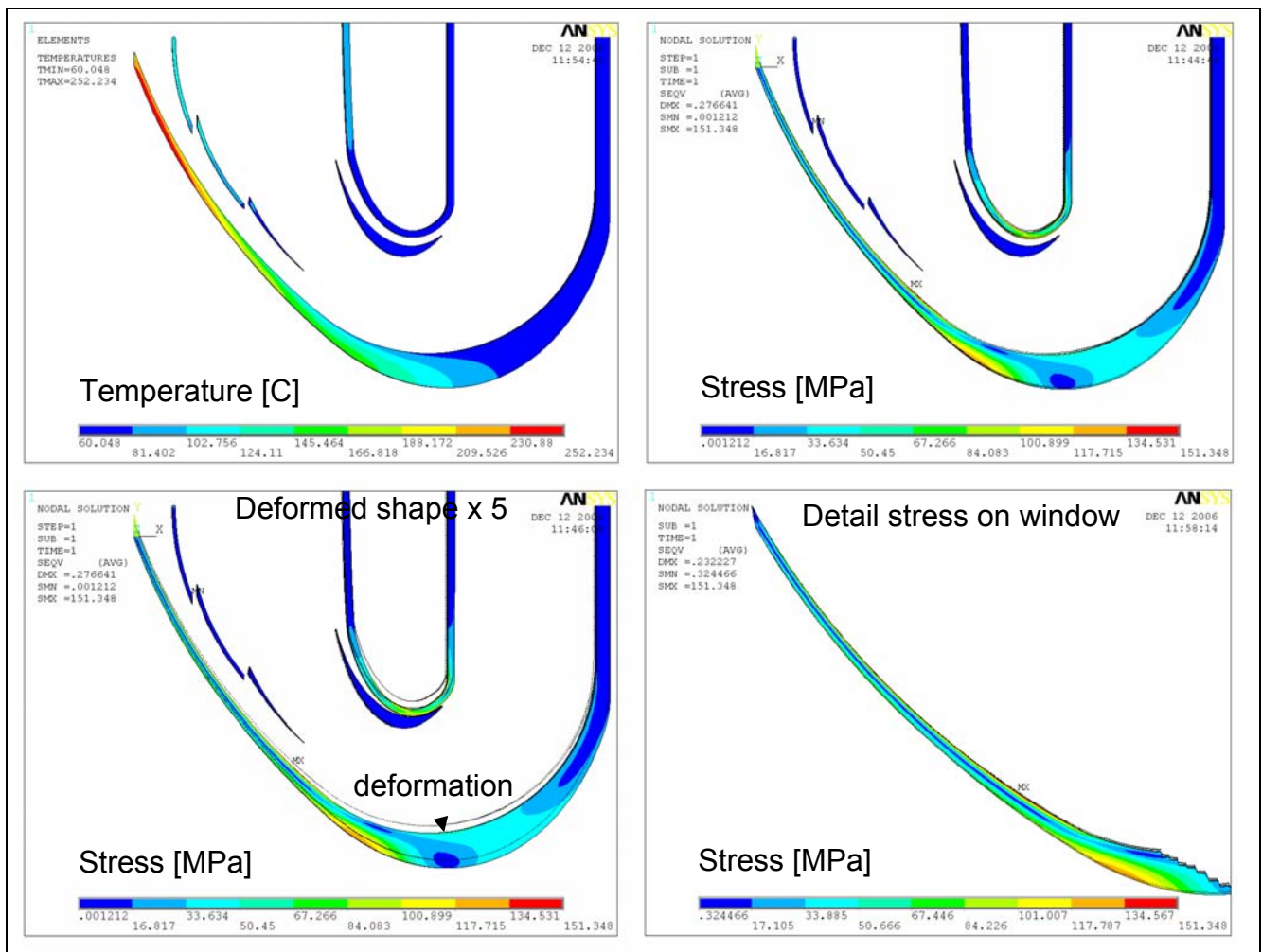
Figure 30: Stress in the window and corresponding temperature distribution due to a σ = 15 mm beam

Figure 30 shows the Von - Mises stress in the window corresponding to the temperature distribution calculated from the proton beam deposition. The maximum stress of 154MPa appears on the inner side of the window, which is admissible at the local applied temperature of 252 C. Note that the peak stress does not coincide with the location of the peak temperature.

According to Table 6, the admissible stress is;

$$\sigma_{Adm} = 190 \text{ [MPa]}$$

The margin of safety is therefore:

$$M.o.S = \frac{190}{154} - 1 = 0.23$$

This margin is sufficient to guarantee the window will not break up to 2 [dpa], the limit validated by RCCMR.

In addition to temperature, pressure is also exerted on the inner surface of the window: this is why the base of the container has been thickened locally to resist bending due to pressure. The most likely static pressure for the production unit is 5 bar; however in order to check the lower target reliability, 10 bar pressure is considered. The optimised design in this section is thus able to withstand a design pressure of:

P_{Design} = 10 [Bar]

Calculations show that in actual fact the pressure is beneficial to the most stressed area of the window, as the compression of the cone reduces the tensile stress caused by differential thermal expansion through the thickness. Hence, with 10 Bar applied pressure, the maximum Von-Mises Stress in the window reaches135MPa which is lower than without pressure (154 MPa). Hence the results without pressure are the most conservative and prove that stresses in the window up to 10 Bar static pressure actually benefit from applying pressure.
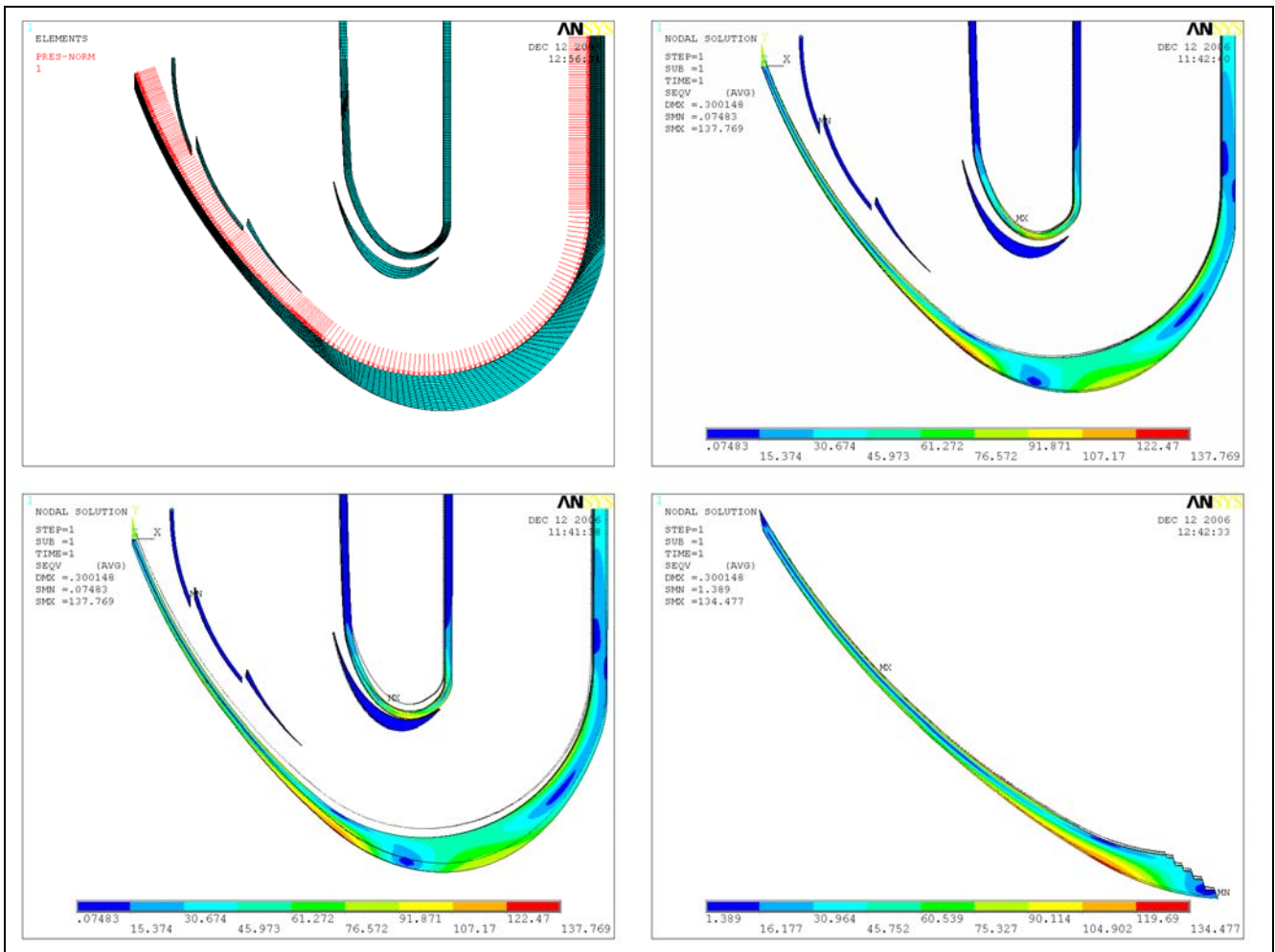
Figure 31: Von - Mises stress in the window corresponding to 10 bar pressure & temperature distribution

The findings in the previous section indicate it is desirable to reduce the thickness in the window. Hence structural stability under pressure may become a serious issue. In order to assess this problem, a 3D local

model of the window has been produced. The structural boundary conditions are clamped at bottom, and the following geometric properties of the window apply:

- o Centre thickness: 0.8 [mm]

- o Edge thickness: 1 [mm]

- o Opening angle: 20 [°]

- o Curvature radius: 90 [mm]

Figure 32 shows the first buckling Eigen mode under 40 [Bar] of pressure. This was a very conservative assumption made early on in the project before the hydraulic optimisation; since then the requirement on the static pressure has been drastically reduced to 10 Bar, but the calculation remains valid. The Eigen mode of 6.36 indicates the safety margin is quite adequate. Assuming ideal clamping conditions and no initial waviness in the shape, the centre peak in the window could sustain 6.36 x 40 Bar = 254 [Bar]. Naturally, elasticity in the restraints and slight manufacturing imperfections would reduce this value.
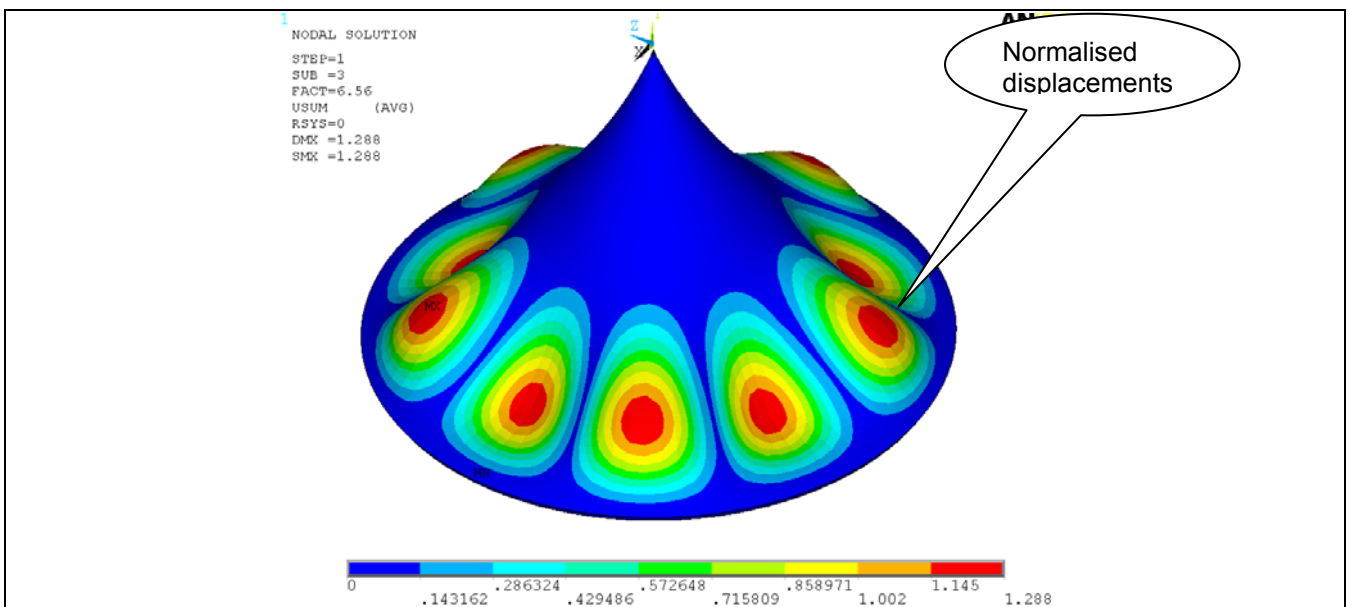
Figure 32: Graphs representing the Buckling Stress [Ref6]

The optimised target shape derived here-above is integrated in the form of a complete design which is coherent with manufacturing practices as detailed in section 2.7 of the current report. This design is modelled both hydraulically in a full CFD model (cf. next section 2.5) and from a structural perspective by a series of complete FEM models which address primarily concerns regarding resonance coupling.

2.4.2 Structural strength of the hull under 10 Bar Pressure

The structural analysis of the converter target focuses on the outer hull which is the main load-bearing component, and for which a simplified FEM shell model was set up.

The maximum static pressure applied to the inner surface of the converter target is 10 bar, with local variations around this value due to the circulation of mercury at high speed. However for assessing peak stresses in the most critical parts, the 10 bar pressure case is dimensioning.

$$\Delta P = 10^6 N/m^2 = 1[N/mm^2]$$

The resulting stress distribution in the converter target outer hull is shown in the figure below. There is a concentration of bending stresses in the cusp region of the window due to the pressure being reacted by the

apex of the window which in turn pushes on the inner rim on the cusp and tends to push it inside-out. These stresses are fairly low, and do not act in conjunction with other peak stresses in the hydraulic test. The allowable design stress at temperatures below 100°C is 400 [MPa] for T91. Hence the safety margin against ultimate failure (S.F. = 1.5) is,

M.o.S. = 400 / (1.5 ^{x} 79.6) -1 = 2.3 against ultimate pressure failure at 10 Bar
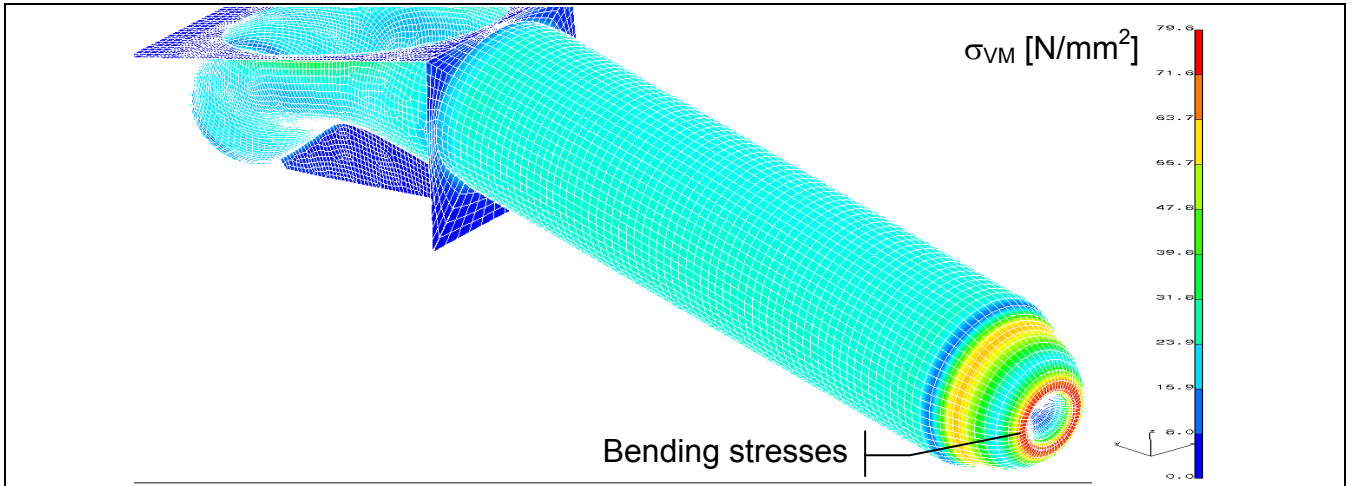
Figure 33: 10 Bar Pressure case Von Mises stress distribution [Ref10]

Furthermore it should be emphasised that under operational conditions under irradiation (not included in the hydraulic test reported here), pressure stresses add to the concentration produced by the beam, however satisfactory safety margins have already been demonstrated in the Eurisol design study (deliverable D1) for this particular case.
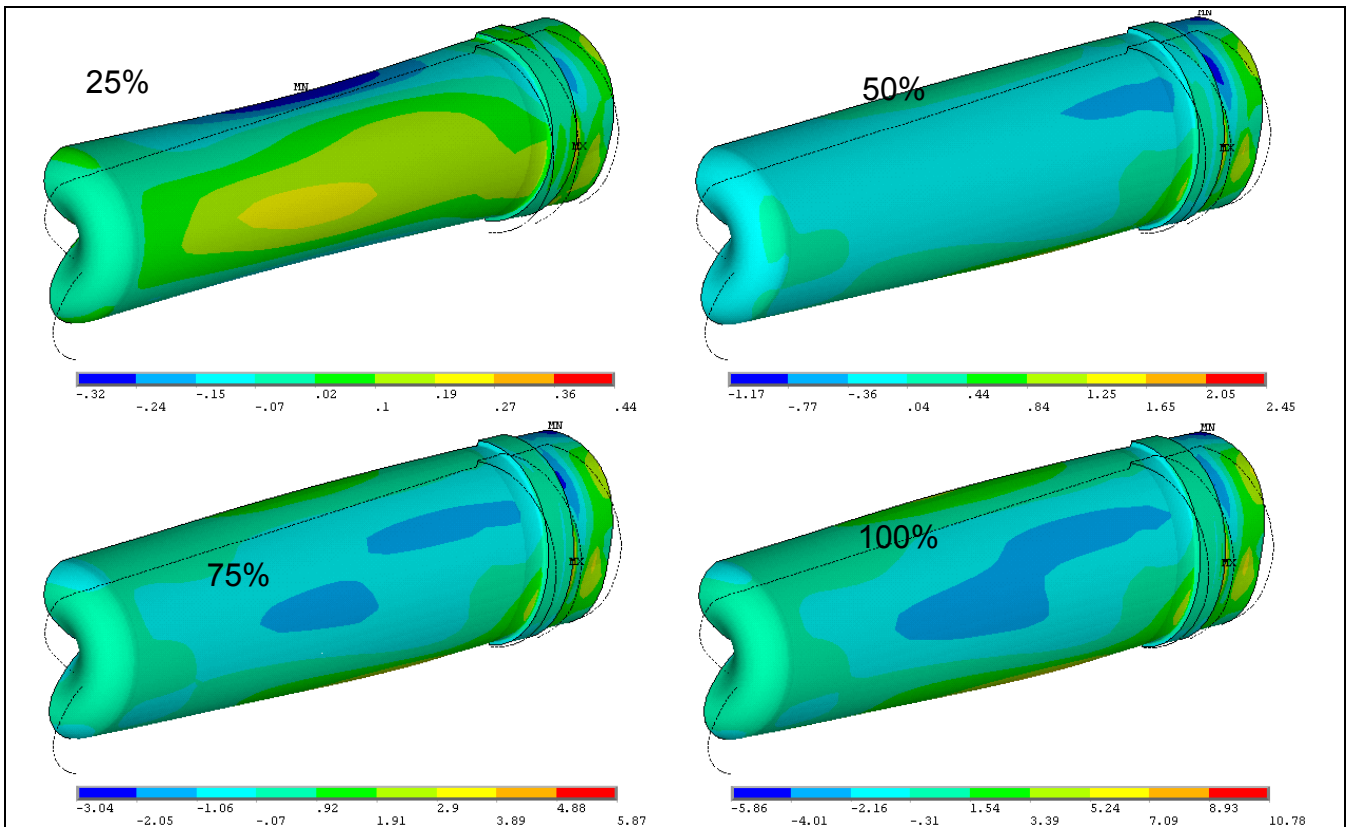
Figure 34: Deformations and Longitudinal stress [MPa] of the target under increasing flow rate from 25 to 100% [Ref19]

The 10 bar pressure case applies mainly to the pressure tests which are run before the actual hydraulic test to check for possible leaks and faulty welds. The actual pressure cases encountered during operation of the target are not uniform but depend on the local velocity field. The full CFD model described in section 2.5.1 allows such a distribution on the outer hull to be accurately predicted. The calculation uses a ramp function on the flow rate as indicated in Figure 46, and pressure distributions have been output for all intermediary steps. Hence pressure distributions on the hull at different flow rates may be applied to the structural model so as to gauge the effect of increasing flow rate in terms of stress and displacement.

The deformations in the hull indicate that with increasing flow rate vertical upwards bending of the hull increases, an effect which was clearly visible from the strain gauges monitoring vertical hull bending in the test (cf. [Ref12]). However the effect of an increasing flow rate on the overall stress pattern in the hull is somewhat diluted by the simultaneous increase in internal pressure which is overlaid with the bending stresses particularly midway between the hull attachment flange and the window end which tends to inflate slightly.

Therefore the measurements with strain gauges in the test took great care to focus on overall bending of the hull and filter out any local disturbance by positioning the gauges close to the hull interface flange at the rear. At that point, bending predominates in the hull and there is clear tensile/compressive pair, such that measuring the reacting bending moment at the base of the hull proved to be feasible in the hydraulic test.

2.4.3 Eigen value analysis of the target filled with mercury

The very high velocities in the liquid metal may cause natural resonance modes in the structure to be activated, which in turn could lead to excessive stresses in the outer hull. In order to gauge the magnitude of this potential problem, a first order approach is to simply add the entire mass of liquid metal to the outer structure and calculate the Eigen-frequencies using the FEM Lanczos method. Any disturbance in the flow coming from the inlet will propagate down the annulus towards the window, and it is only this mass of liquid entering the target which will participate in the postulated coupled resonance phenomena. So by adding all the mass in the target to the mass of the hull, the calculated value of the first Eigen-frequency will probably be lower that in reality. However it is the lowest frequencies which are the most likely to damage a structure, as such the approach is conservative.

First Eigen mode at 62.2 Hz.
Lateral vibration

Second Eigen mode at 67.8 Hz.
Vertical vibration
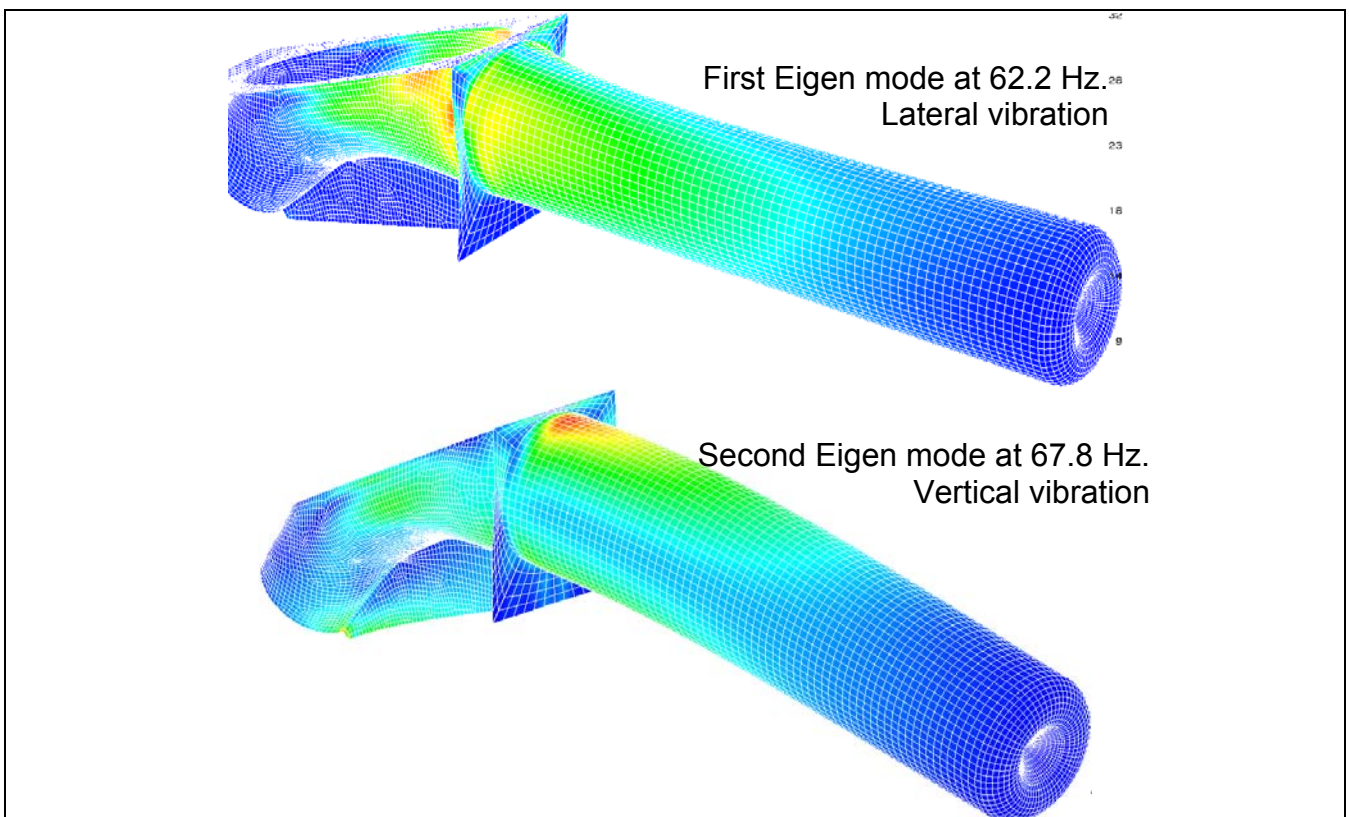
Figure 35: Mass-normalised Von Mises stress on deformed shape of first two Eigen modes [Ref10]

The stresses shown in Figure 35, have been calculated for a normalised Eigen-frequency vector. There are an infinite number of solution displacement vectors since the analytical method derives the mode shapes from a diagonalisation of the stiffness matrix. The stresses shown in the figures correspond to very large displacements for a mass-normalised Eigen-vector, which is physically impossible. To continue with this method, a full dynamic analysis is needed, which entails applying a PSD or sine-sweep of the excitation pressure load to the wetted walls of the structure, calculated from the fluid turbulence.

In a first approach, it is easier to calculate stresses from an enforced static displacement which results in roughly the same structural deformations as the characteristic Eigen-mode shape. The first mode shown in Figure 35, indicates that the stresses are caused by a lateral bending of the outer shell. In the corresponding static stress case shown in Figure 36 the entire window is shifted 1 mm to the side and stresses are calculated accordingly. This gives a fair assessment of the structural limits the hull may endure without failure.

2.4.4 Static lateral displacement, 1 mm

A 1 mm lateral displacement is enforced at the window. Results below show the stress pattern is quite similar to that obtained in the resonance case for the first Eigen-mode.
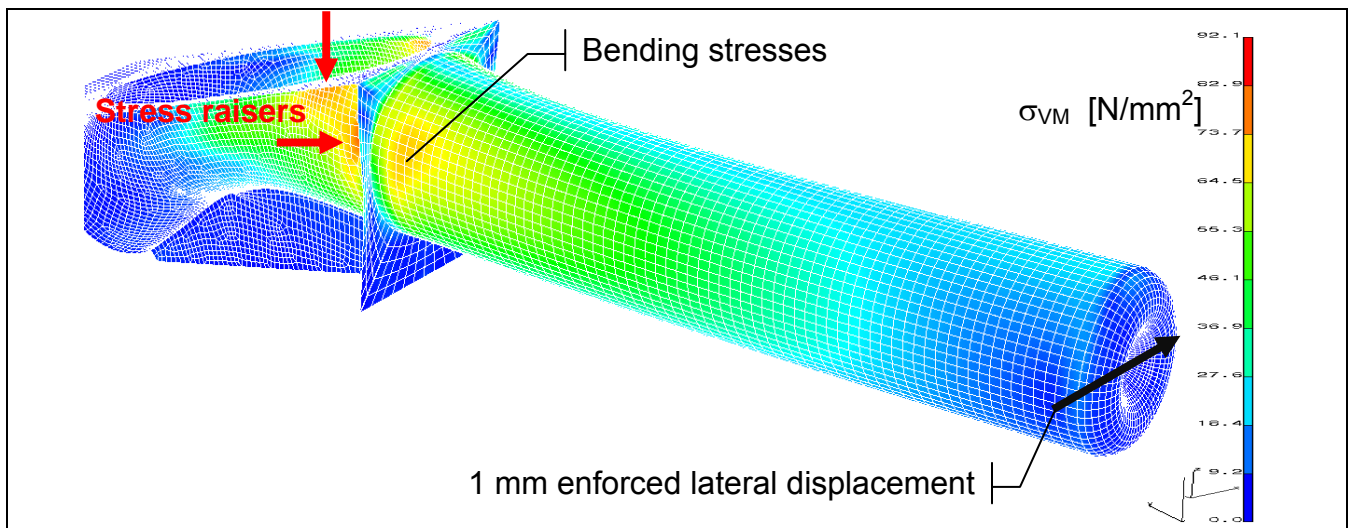
Figure 36: Von Mises stress distribution for the 1mm Lateral displacement case [Ref10]
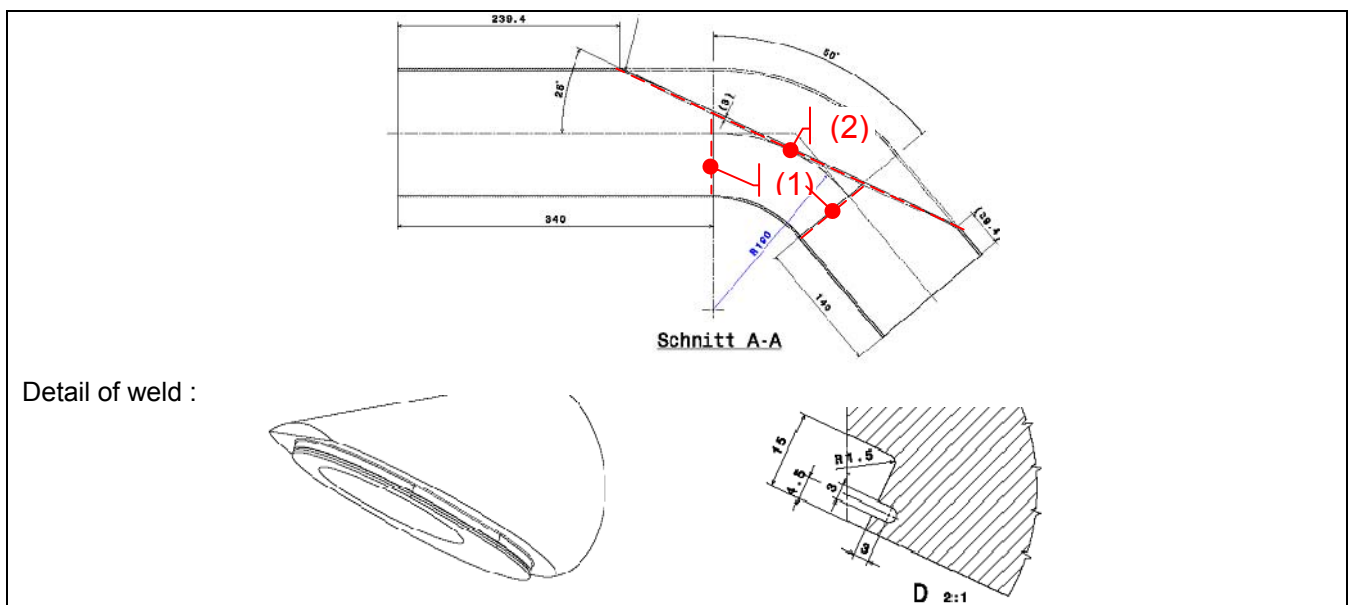
Figure 37: Detail of the welds in the inlet tube [Ref10]

The stress peaks visible in Figure 36 and Figure 38 above are located close to weld seams which have to be examined in more detail. Since the FEM consists in 2D shell elements, the best method is to extract the element shell stresses in critical areas indicated by the arrows in Figure 36 above. The relevant plate elements are chosen according to their position with respect to the stress peaks and weld locations. This is illustrated in the next few figures by a comparison of a side view of the inlet tube with the stress distribution.
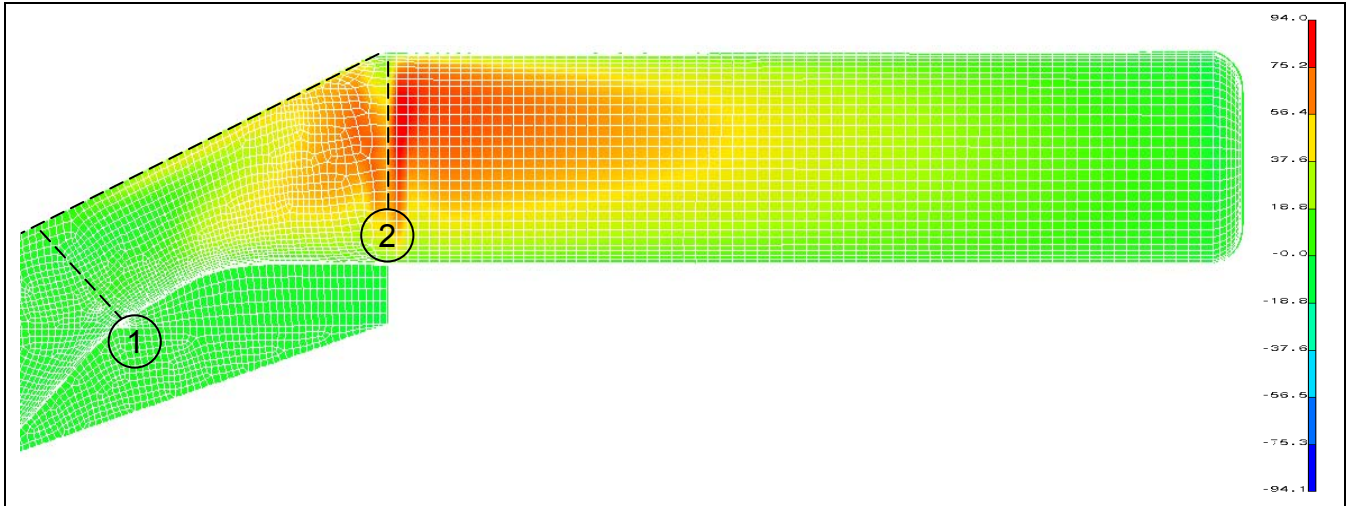
Figure 38: Stress distribution in longitudinal direction for the 1mm Lateral displacement case. [Ref10]

There are fundamentally two types of welds at risk: The first (1) in Figure 38 is a conventional V-weld around the perimeter of the tube either end of the bend, the second (2) is a weld to a scarf-type junction running the full perimeter of the angled cut where it joins onto the fixture for holding the target to the test rig.

The stresses in longitudinal direction are shown in Figure 38 above and reach a peak of 95 [N/mm^2] for a 1 mm lateral enforced displacement. In the vicinity of weld 1, longitudinal peak stresses are in the order of 70 [N/mm^2]. As this is a V-weld the section need not be reduced other than by the weld factor. For a qualified welder this factor is 0.8. Hence the margin on weld 1 is;

> M.o.S. = 0.8 ^{x} 400/ (1.5 ^{x} 70.0) -1 = 2.05   against ultimate failure of weld N°1 for a 1mm lateral displacement of the window

For the second weld (2 in Figure 37 and Figure 38), the stress is somewhat more complex as the design shown in Figure 37 includes a groove to relieve built-in stresses from the welding of the inlet tube to the fixture. Hence when the lip of the groove is pulled, this will create a stress concentration in the radius of the groove.
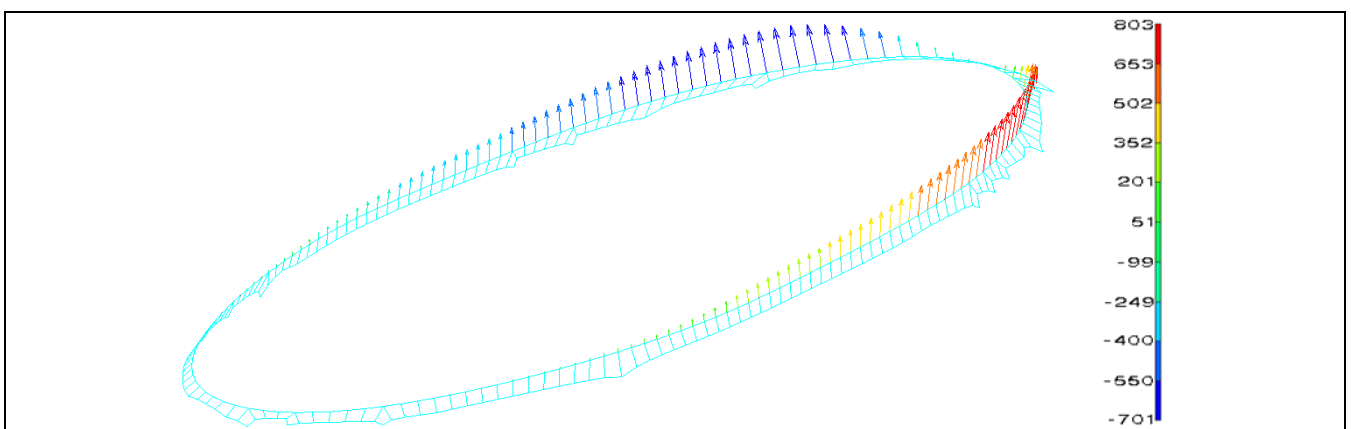
Figure 39: Interface loads [N/mm] at inlet tube interface for the 1mm Lateral displacement case [Ref10]

The underlying assumption in the model is that the tube is connected edge-on to the interface. In reality there is a weld seam along the face which displaces the line -of-action of the tube membrane stress and tends to

open the groove more. It is therefore more relevant to determine the stress at the location indicated by 2 in Figure 38, but at right angle to the weld, not in the global longitudinal direction. This may easily be derived from the reaction load at the nodes where the inlet tube attaches to the slanted scarf as pictured in Figure 37. The magnitude of the nodal forces are shown in [N] and can be converted to a running load by dividing the average pull-out component of the nodal forces by the average distance between nodes.

$$f = \Delta F / \Delta l = 375 / 5.2 = 72 \ [N/mm]$$

Hence the revised stress concentration in the groove can be obtained from the classic formula:

$$\sigma = 6 \times (M/l) / t$$

Where:

t is the thickness of the weakest section = 3 [mm] (see Figure 37)

(M / l) is the running bending moment in Nmm /mm $= f \times b$

and b is the moment arm = 2 [mm] (see Figure 37)

Hence:

$$\sigma = 6 \times (72 \times 2) / 3 = 288 \ [N/mm2]$$

This will yield a slightly negative margin;

M.o.S. = 400/ (1.5 $\times$ 288) -1 = -0.07   against ultimate failure of weld N°2 for a 1mm lateral displacement of the window

Weld 2 is clearly a weak point in the structure which has to be monitored carefully. It is difficult to reinforce the structure at such short notice, so the best option is to install a strain gauge close to the weld. For zero margin the lateral displacement must be no more than:

$$\Delta x = 1 \ mm \times 400/ (1.5 \times 288.0) = 0.92 \ [mm]$$

This corresponds to a lateral acceleration on the window of;

$$\ddot{x} = \Delta x \cdot \omega_0{}^2 = \Delta x \cdot (2\pi f_0)^2$$

Where f_0 = 62 [Hz] is the estimate of first lateral Eigen frequency, which results in the following limit for the lateral acceleration, as

$$\ddot{x} = 139 \left[m/s^2 \right] = 14 \ [g]$$

The acceleration limit depends critically on the Eigen frequency of the actual target on the test stand which is difficult to predict. If the real structure resonates at a lower frequency, the acceleration limit at which damage occurs is lower. Halving the Eigen frequency would entail dividing the acceleration limit by 4, to a level of 3.25g.

2.4.5   Sine-sweep resonance analysis

Large-scale pressure variations on a flexible structure may excite natural resonance modes. The study of this coupled phenomenon could in theory have been carried out using coupled software which would have calculated the deformation, speed and acceleration of the structure at every time step in relation to the pressure field. This would then have been fed back as a boundary condition to the hydraulic calculation for the next time step.

The LES hydraulic analysis of the three-dimensional model, with no such structural coupling, necessitated 30'000 time steps, and computational run times of approximately 2 months. Full coupling between the structural and hydraulic calculation would undoubtedly have slowed down the computational effort considerably, beyond what could reasonably be tolerated within the time frame of the project. The full coupling option was therefore abandoned.

In lieu of full structural-hydraulic coupling, the disturbances in the pressure fields calculated by the LES were abstracted using the Fast Fourier Transform method and applied to a structural model. This allowed the dynamic component of the hull stresses to be computed. Section 2.5.4 describes the extraction of the pressure histories at relevant locations, which are analysed in the frequency domain in order to gauge their effect in exciting a resonance in the structure. Thus, the Discrete Fourier Transform method used at selected points is reckoned to be representative of the pressure variations on the target as a whole.

The method used in abstracting the time-variable pressure curves is illustrated below in Figure 40 for point 42 which is located within the top vortex identified in Figure 53. The LES pressure history in Figure 55 is analysed by a DFT which sweeps the pressure – time curve well into the LES simulation of developed turbulent flow. In this manner the oscillatory turbulent structure in the flow is fully developed, and the periodic content in the curve can be more readily extracted by the DFT method

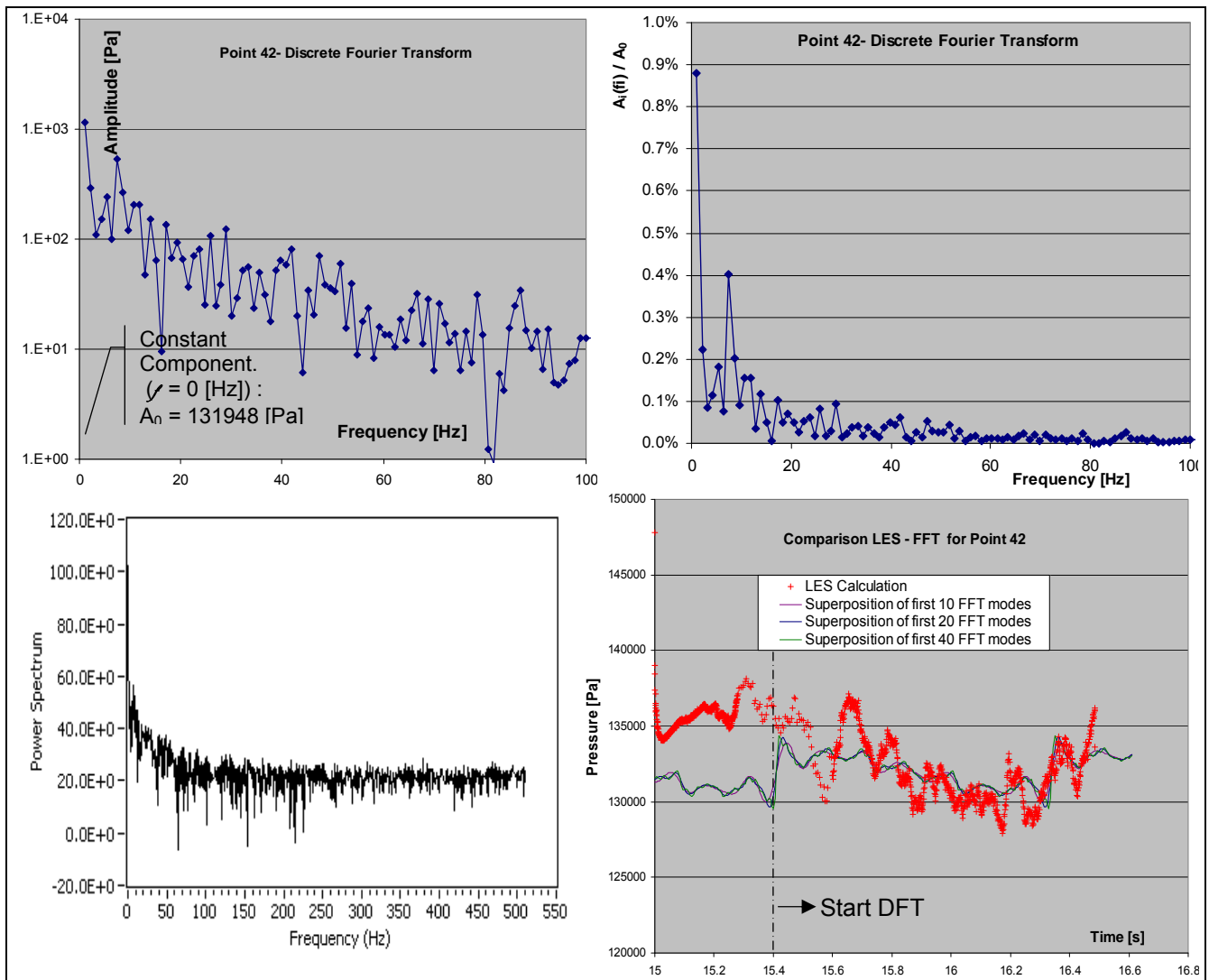**Figure 40: Frequency content (top) and DFT / LES comparison (bottom) of point 42 pressure [Ref19]**

The DFT decomposition in terms of amplitude as a function of frequency is shown in the two top graphs of Figure 40. The bottom left-hand figure is a PSD (power spectral density) of the same pressure-time curve. The top left-hand graph shows the absolute value of the amplitudes of each mode and the right-hand graph gives

the same amplitude of each frequency but as a percentage of the constant amplitude for f_0 = 0 [Hz]. Both in absolute and relative terms, the constant pressure component plays a quite dominant part. Indeed, the next highest component at 1.07 [Hz] and 7.5 [Hz] barely reach 1 % of the total pressure.

The PSD function at the bottom left of Figure 40 confirms the observations made with the DFT; there is an increase at low frequencies which peaks at 60 [Pa^2 / Hz] and tapers off quite rapidly above 20 [Hz]. The energy content is therefore fairly homogeneously distributed, at this particular point 42.The comparison in the bottom right-hand graph of Figure 40 demonstrates the similarity between the original pressure history curve extracted from the LES calculation and the approximation derived form the DFT thereof, using a superposition of the first N modes according,

$$p(t) = A_0 + \sum_{i=1}^{N} A_i \sin(2\pi f_i \cdot t),$$

where A_i are the discrete amplitudes of each of the frequencies f_i as shown in the DFT graph at the top of Figure 40. Increasing the number of modes from 10 to 20 then 40 seems to improve the agreement between the DFT approximation and the original pressure – time curve.

The DFT on different critical parts of the target (Figure 55) indicate that the worst oscillations occur on the leading edge of the guide tube, where the amplitude of low-frequencies below 20 Hz reaches 5-10 % of the total pressure. This is quite significant in comparison with the remainder of the structure, but it is also quite localised. The area of the guide tube affected by such high variations is solid metal with high local stiffness. However, the guide tube as a whole is built-in at the opposite end of the oscillations on the leading edge, so this could indirectly lead to bending stress at the built-in clamped section of the guide tube.

Figure 41 shows extractions on many points grouped in a single plot for comparison. This allows an envelope curve of the pressure variations to be created. It is clear that the high pressure variations on the guide tube entrance (Point 26) are outside the envelope. However given that the oscillations down the guide tube abate quickly after the entrance point it is unlikely to have an overall effect on the structure.
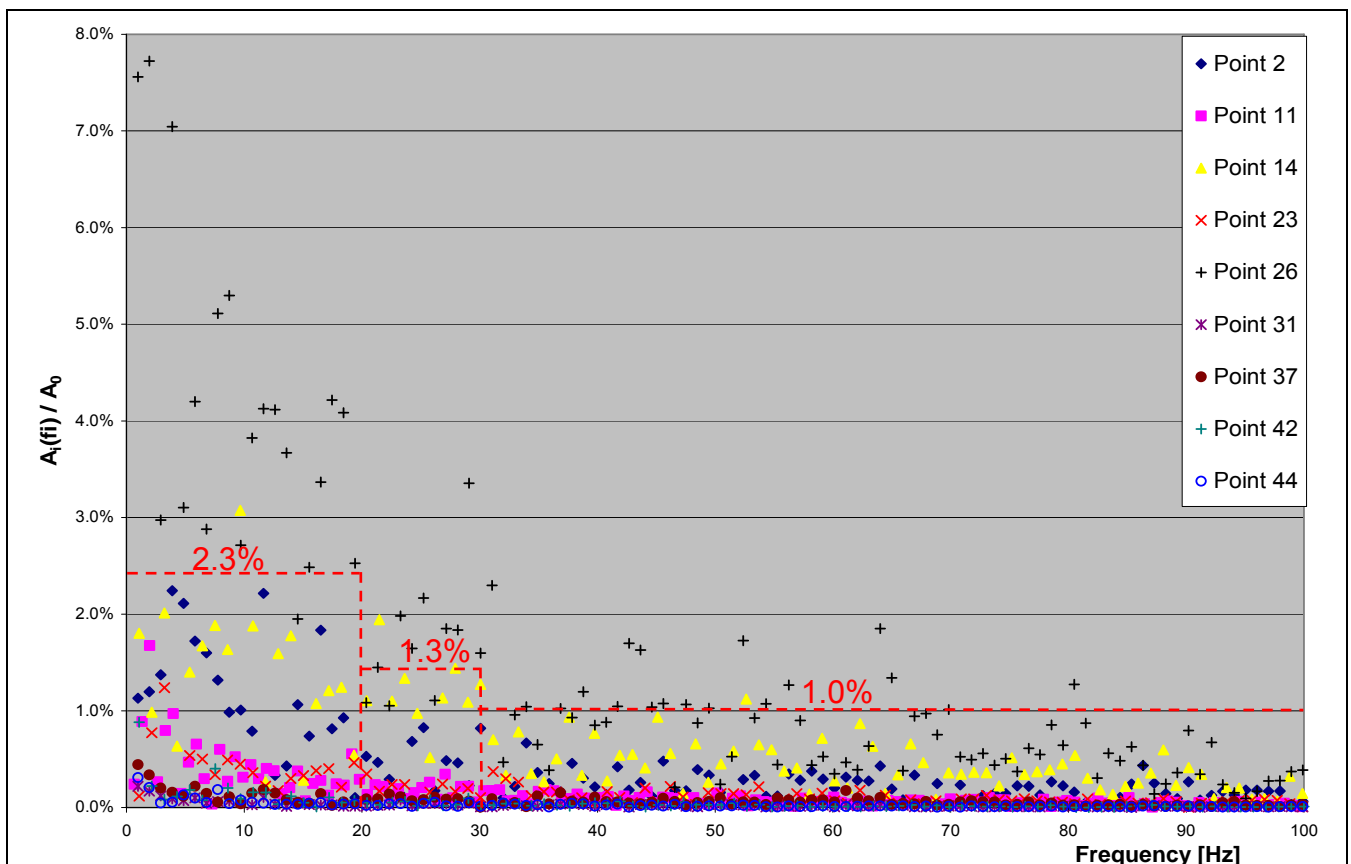
Figure 41: Overview of all representative pressure variations with envelope curve [Ref19]

The model of the target used for mechanical analysis uses a highly structured mesh. The mesh definition needed for a calculation of the stresses is not the same as for the CFD. The structural mesh needs more refinement in areas where the stiffness of the structure changes abruptly, where a weld is located or where a load introduction point occurs. On the CFD side however the boundary layer needs a high definition transverse to the wall; areas which are curved need good stream-wise definition and tend to favour box-like structured meshes. The structural model retains the half-symmetry used in the CFD as the two models are linked by the common assumption that the instabilities in the flow are broadly in the vertical and longitudinal direction because of the action of the inlet.

A new model of the structure of the hull was therefore created independently from the previous CFD mesh but using the same geometry. The pressure distribution resulting from the CFD is then projected onto the structural model so as allow stresses and deformations to be calculated in time-dependent mode.
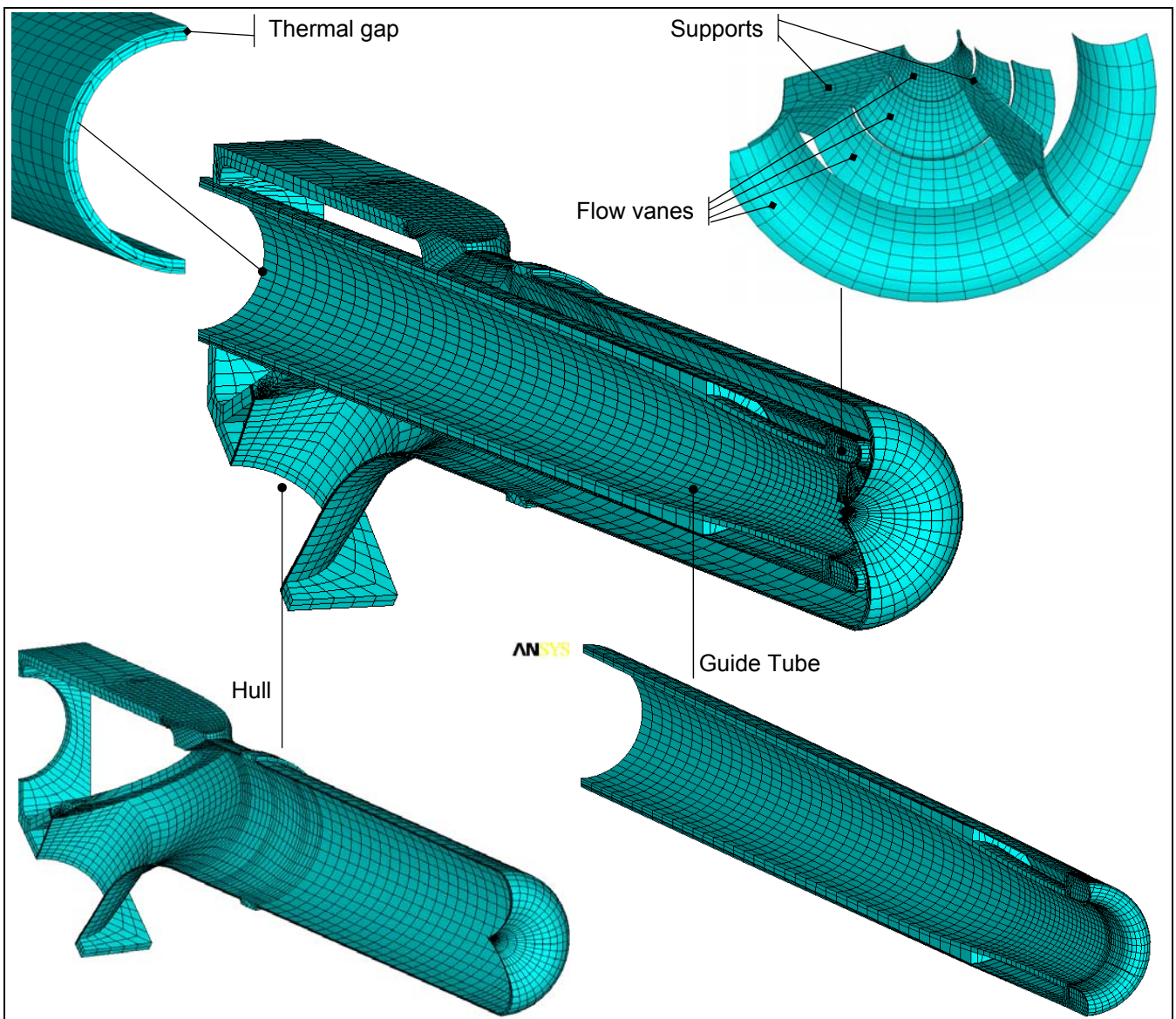
Figure 42: Structural FEM Model used in calculating the stresses and deformations from the pressure distribution [Ref19]

Details of the internal structure of the model are shown surrounding the FEM in the centre

The effect of the static time-averaged pressure load on the target has been studied. In the following the dynamic component is evaluated as a percentage of the preceding static pressure load. The sine-sweep method is used for the computation of the dynamic stresses in the target. The method assumes that the Eigen modes are essentially decoupled from one another, as is the case in the simple structure being studied at

present which has distinct resonance modes. The method illustrated in Figure 40 will therefore be applied to the target using the dynamic component of the pressure variation. The relevant factor expressing the amplitude of the pressure variation is a percentage of the total static pressure load and is extracted from Figure 41 as a function of the frequency. The flow vane assembly and overall structure are examined separately, as the vanes move quite significantly relative to the rest of the target. First the vanes are examined in Figure 43. The graph at the top of Figure 43 indicates where the peak resonance Von Mises stresses occur, from 30 to 200 [Hz], the area below 30 [Hz] having been swept but not shown any coupling. The frequency-dependent stress level monitored in the top graph represents the peak stress location in the flow vane assembly; the weld connecting the vane to the support is therefore at risk.
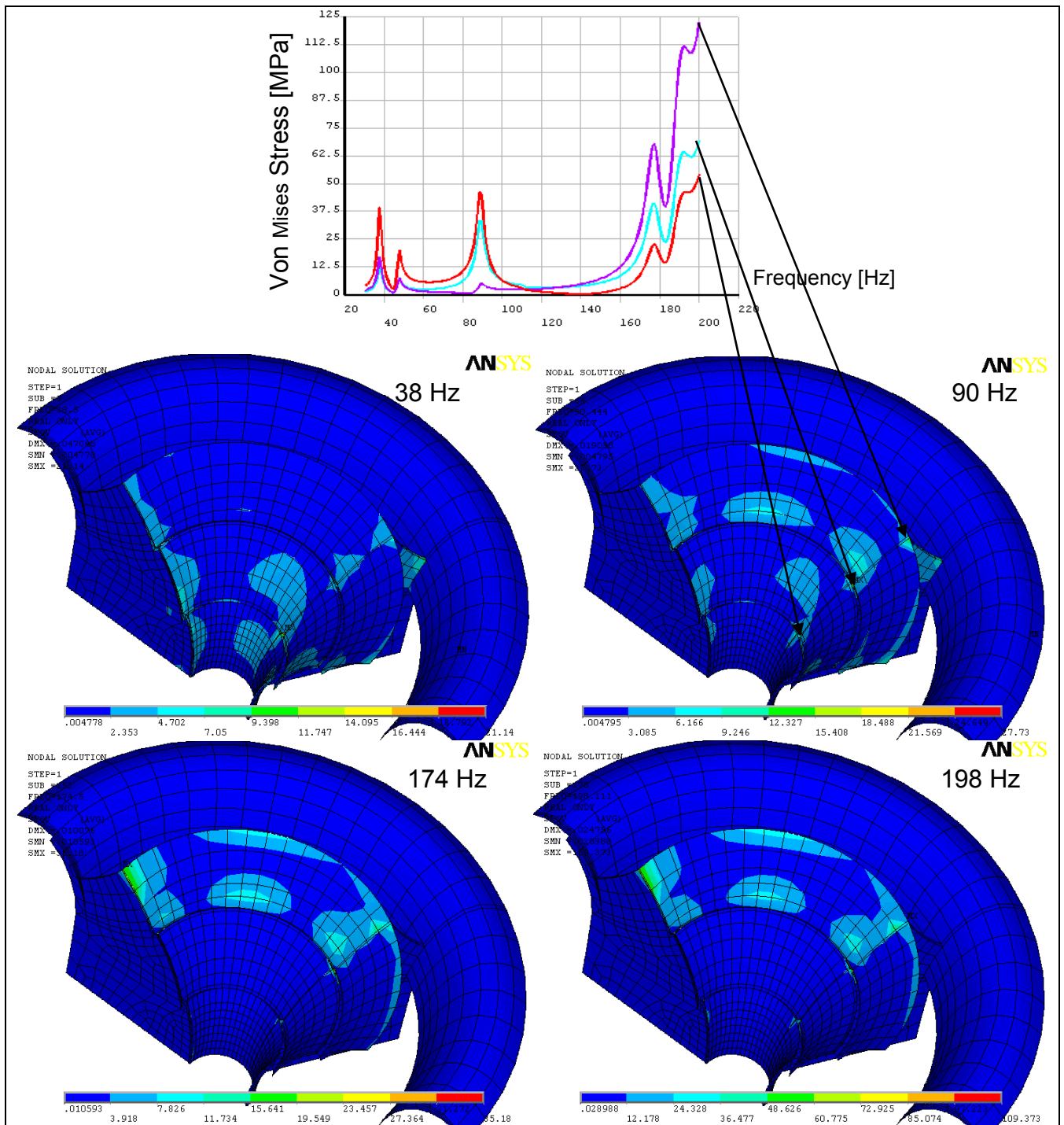
Figure 43: Dynamic stresses in window vane assembly at peak resonance.[Ref19]

The pressure fluctuation on the flow vanes leads to a peak stress of 109 [MPa] at 180 [Hz] which when added to 76 [MPa] of static stress reduces the margin on the weld to,

$$M.o.S = \frac{0.8 \cdot 400}{1.5 \cdot 185} - 1 = 0.15$$

In the above calculation of the dynamic stress, damping was set at 2%. Damping affects the peak response at resonance. Higher damping lowers the peak displacement and hence stresses. In general 2% damping is considered adequate for most homogeneous structures consisting in welded or integrally machined parts. More complex mechanical components such as aircraft wings or rocket stages are given values of up to 4 % damping. Obviously there is an element of guesswork involved in apportioning the correct amount of damping to a structural resonance problem. However it is clear that a complex structure with numerous parts that are bolted or riveted together such as in aerospace structures can dissipate more energy under vibration than a structure such as the one considered here which is mostly welded and therefore essentially homogeneous. For this reason, a value of 2% was chosen for damping which proved to be conservative. Indeed during the hydraulic test reported in [Ref12] the attenuation of vibrations from a hammer test showed that the actual value of damping was closer to 3%.

The guide tube is examined next purely from the point of view of the displacements (Figure 44) as the structural margins in the hull and guide tube under dynamic loads are of no concern (Figure 45). The resonance frequencies are fairly low but small in amplitude. They should not affect the flow, the displacement at these resonances being smaller than the thickness of the boundary layer.

Figure 44: Dynamic deformation in guide tube and hull assembly at peak resonance [Ref19]

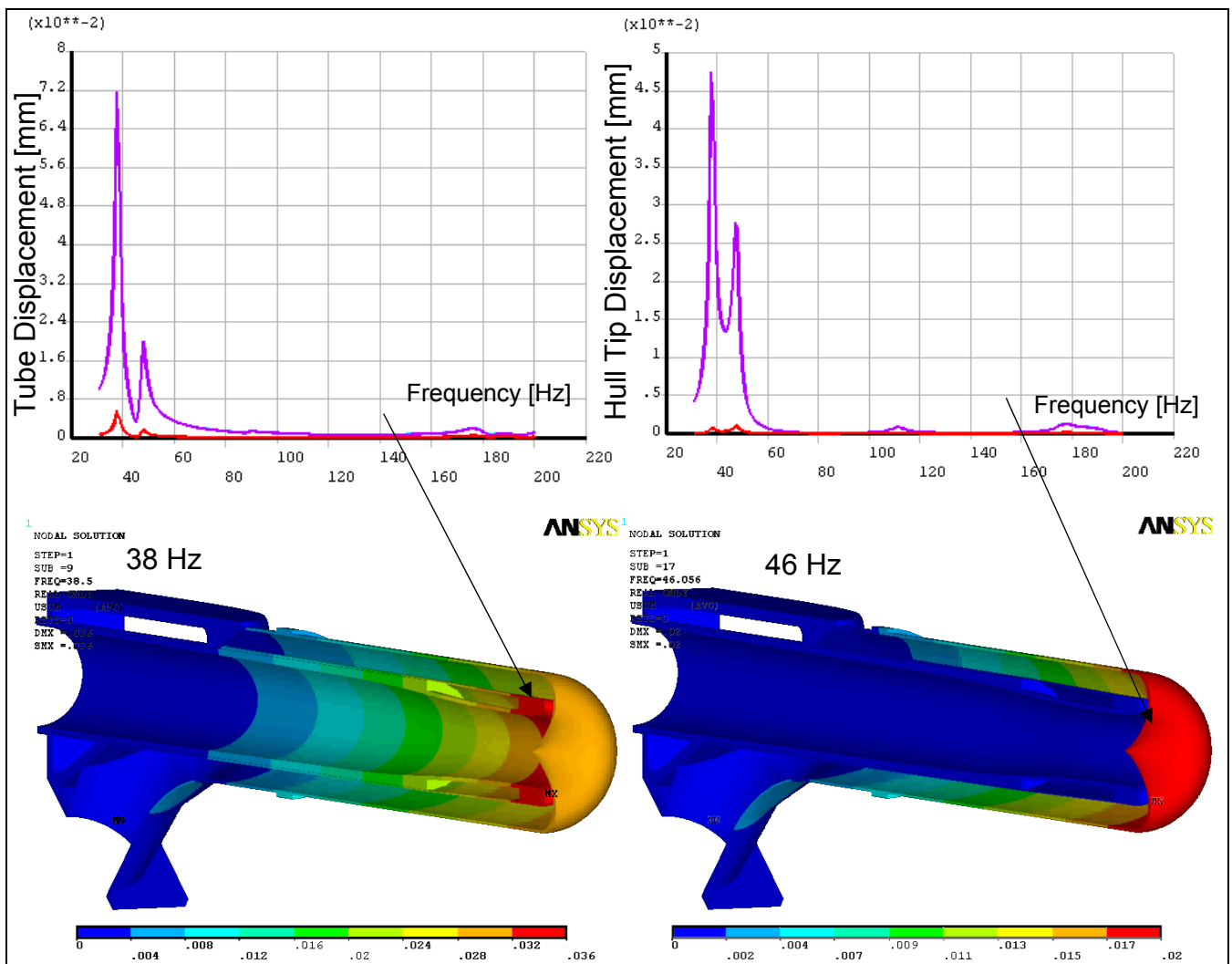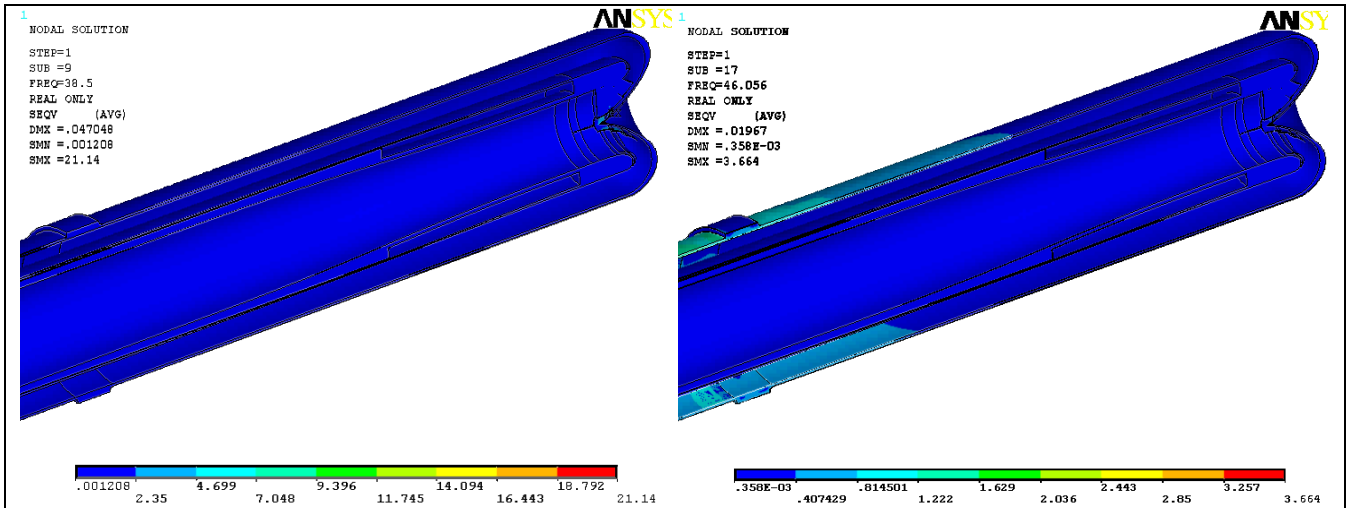**Figure 45: Dynamic stress in target at peak hull resonance [Ref19]**

Structural integrity of the hull is not obviously threatened by dynamic stresses which are in the order of 1 MPa at the most. Therefore the static stresses shown in Figure 34, around 5 [MPa] caused by the straightening out of the bent tube will predominate. This does not include the internal pressure which is variable as described in [Ref12]

2.5 Hydraulic performance of the optimised target

2.5.1 Global CFD model of the initial design

The use of Computational Fluid Dynamics (CFD) is now quite common to predict liquid metal flow patterns. Prior experience with the Megapie project at PSI as well as experiments such as Achlim at FZK have demonstrated reasonable agreement with the standard turbulence models implemented in commercial codes as for instance CFX which was used in [Ref8] to predict hydraulic behaviour as shown the following. The CFD model used for predicting the flow pattern in the hydraulic test did not include any structure, nor heat deposition from the beam as it was used solely for predicting the pressure and velocities in the fluid and derived structural behaviour was predicted by a dedicated FEM structural model.

The CFD model has 3 million cells. Initially, turbulence is modelled using an SST (Shear Stress Transfer) model, as it is more stable numerically although it lacks the ability to resolve some periodic turbulent structures which may be of interest. Hence the SST model was only used to ramp up the fluid flow in the target to full power at which point the analysis proceeded with an LES (Large Eddy Simulation) turbulence model, using the results at full power for initial conditions. The ramping up of the flow does however yield interesting information on the pressure drop across the target. The ramp-up function to full power is shown schematically below.
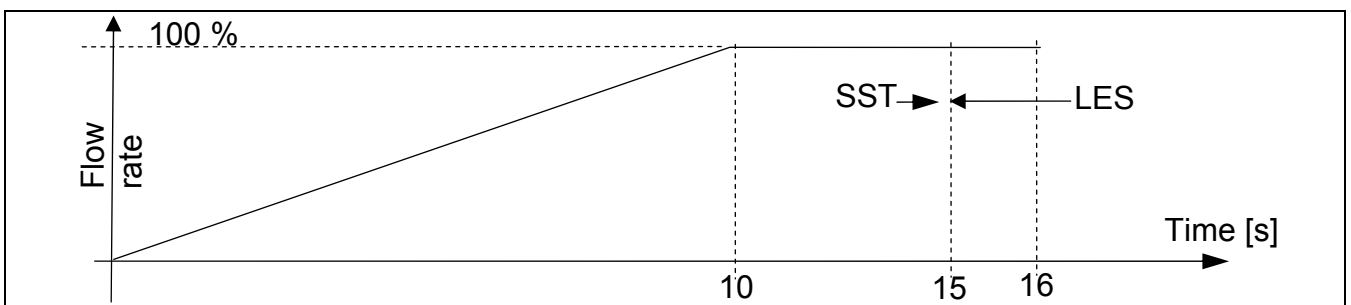
Figure 46: Ramp-up of the flow in the CFD analysis [Ref 19]

The CFD model of the full target uses half-symmetry through the longitudinal vertical plane, to reduce its size. The reason underlying this model assumption is that any major flow dissymmetry which may occur is more likely to occur between the upper and lower half of the source. The likelihood of a local dissymmetry such as a Von Karman vortex arising behind the support of the vanes is studied by splitting the top support in half, which results in one of the supports being at 120°, totally surrounded on either side by fluid.

The three-dimensional CFD model is highly complex and encompasses three million cells in a structured hexahedral mesh. The figure below shows model details areas of particular interest such as around the vane supports, the vanes proper and the inner surface of the beam window. Figure 47 shows the detail of the CFD model described summarily here-above.
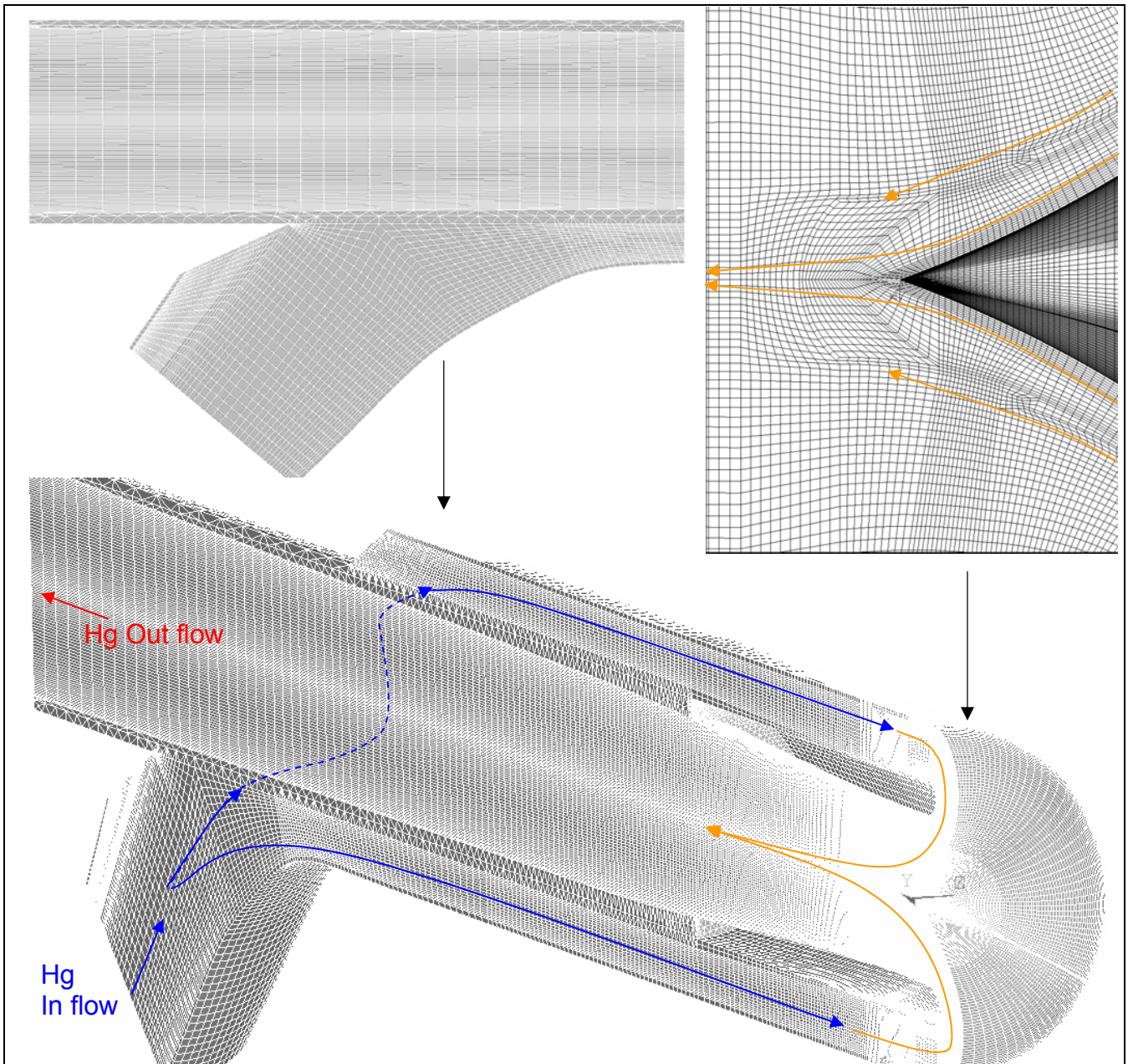
Figure 47: CFD Model details of the target [Ref19]

The physical models for the fluid are strictly limited to the requirements necessary for predicting hydraulic behaviour in the most effective manner. This entails in particular that the following restrictions apply;

- There is symmetry in the vertical plane.

- The inlet turbulence is 5%

- The outlet pressure is defined at 0 Bar relative and defined as an opening (which allows two way flow)

- The fluid is one phase and non buoyant

- There is no transfer of heat to the wall nor heat deposition from the beam

- The SST model is used to ramp up the fluid flow to nominal over 10 seconds.

- The LES turbulence takes over after a 5 second stabilisation and is run for at least 1 second

The CFD model one run at full power gives results that may be compared to systems measurements. The most relevant are the velocity fields which can be compared easily along the walls by pressure taps.

The beam end of the target is of particular importance, due to the need for cooling the window, for which flow vanes were proposed (Figure 48). Both configurations with and without flow vanes were validated experimentally [Ref9], but they were also investigated ahead of the test with CFD, in particular with an LES turbulence model which is most adapted to studying large-scale oscillatory turbulent phenomena.
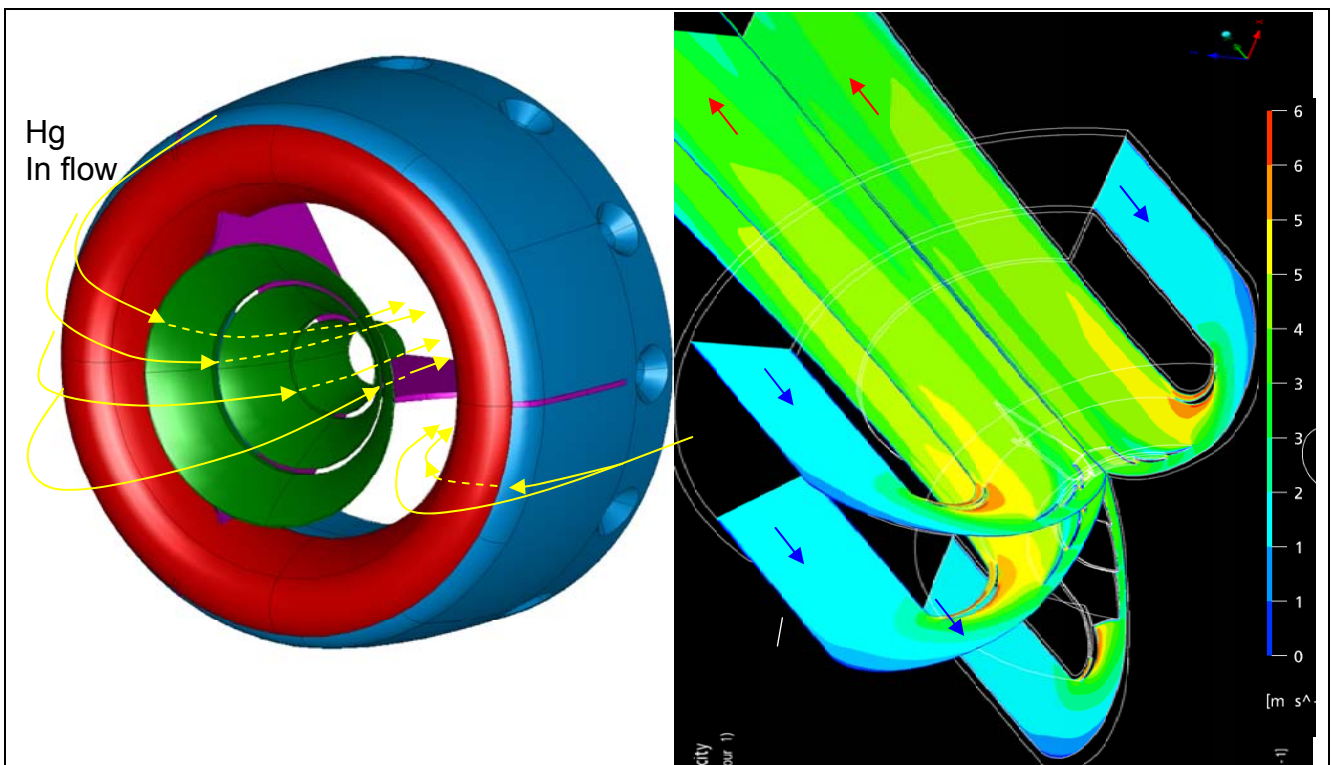
Figure 48: Flow reverser design (left). Detail of beam window flow pattern and velocities (right) [Ref19]

The design with flow vanes as shown in the left side of Figure 48 is rather complex to manufacture, and it was one of the main goals of the test to determine its degree of effectiveness. The velocity magnitude profiles taken along various longitudinal sections and shown in the right-hand side of Figure 48 indicate quite clearly an area of high acceleration at the beam window, where the vanes have been implemented.

It is therefore informative to observe the time-evolution of the velocity field during an LES simulation as illustrated in Figure 49. The figure examines a comparison of the flow field projected on the vertical symmetry plane for the design with flow vanes as compared against the case where the flow vanes are removed. The velocity field during the LES simulation indicates a steady flow configuration over the window with the flow reverser but an oscillating detachment if the reverser is omitted. The structure in the outflow channel is also more unsteady without the flow reverser. The pressure fluctuations from the large-scale instabilities are limited to the inner surface of the guide tube which is therefore more likely to be subjected to vibrations than the outer

shell, where the velocity is both smaller and appears more stable. The beneficial effect of the reverser seems therefore to be both in terms of limiting vibrations in the outflow and precluding cooling variations on the beam window which would have a detrimental effect on the lifetime of the window through high cycle fatigue.
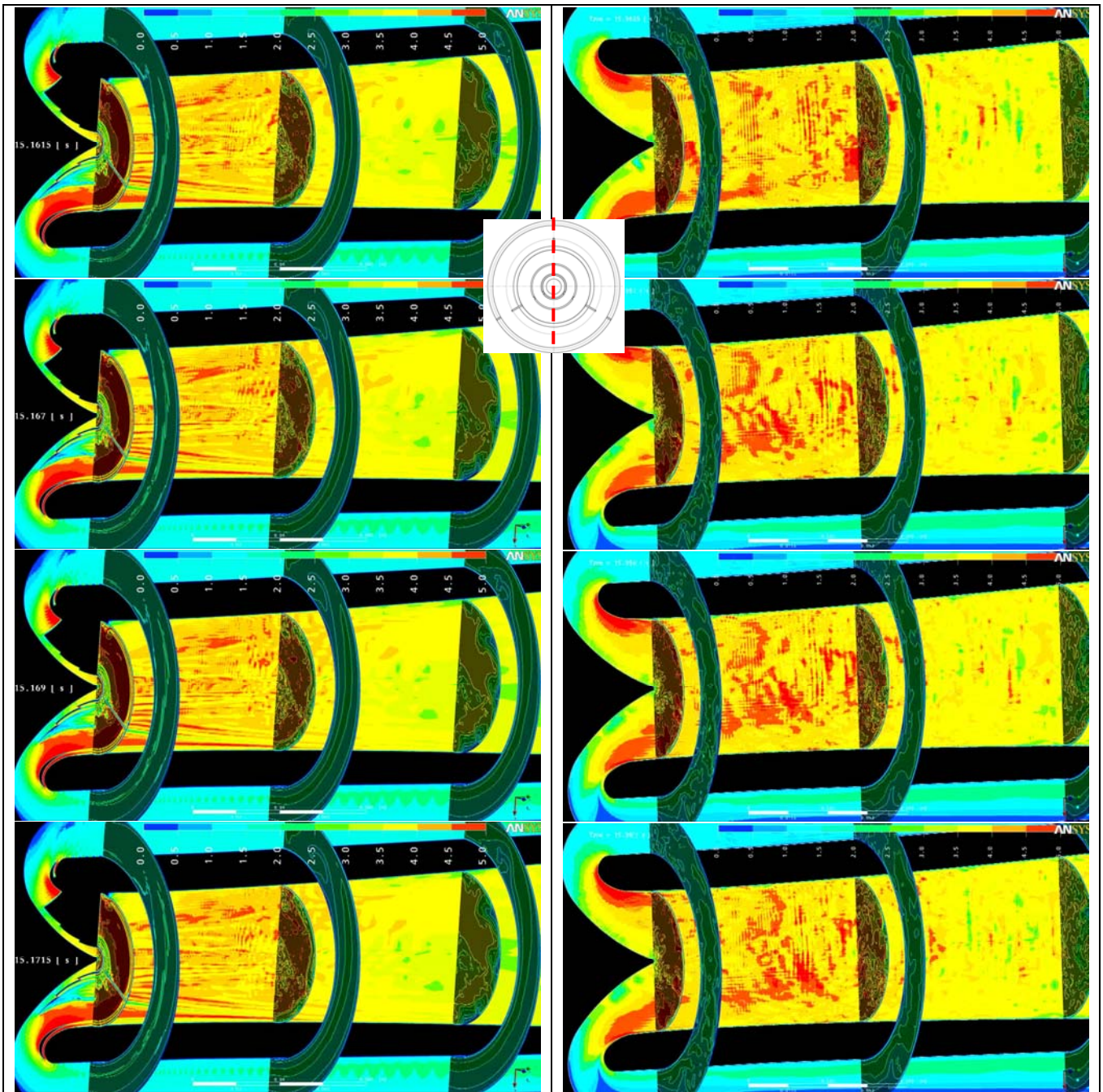
Figure 49: Velocity fields at $^2/_{1000}$" intervals with (left) and without (right) the flow reverser [Ref19]

The overall velocity field is shown in Figure 50. The pressure losses from inlet to outlet are in Figure 51, and are found to be well below 1 Bar which is within the systems specification set out early on in the program. The areas in blue at or below -1Bar relative, or 0 [Bar] absolute indicate that cavitation will occur locally unless the static pressure in the loop is increased. A detail look at the structure of the pressure contours around the vanes indicates that an overpressure is required to suppress cavitation locally around the forward end.

Figure 51 shows static pressure inside the target changes gradually along the duct as expected due to friction on the walls. The outlet pressure is fixed at 0 Bar, so all static pressures in the conduit are relative to this reference static pressure. In the test the actual static pressure was varied from 3 to 5 Bar. The boundary conditions specify a fixed entrance mass flow rate, and zero relative pressure at the outlet.
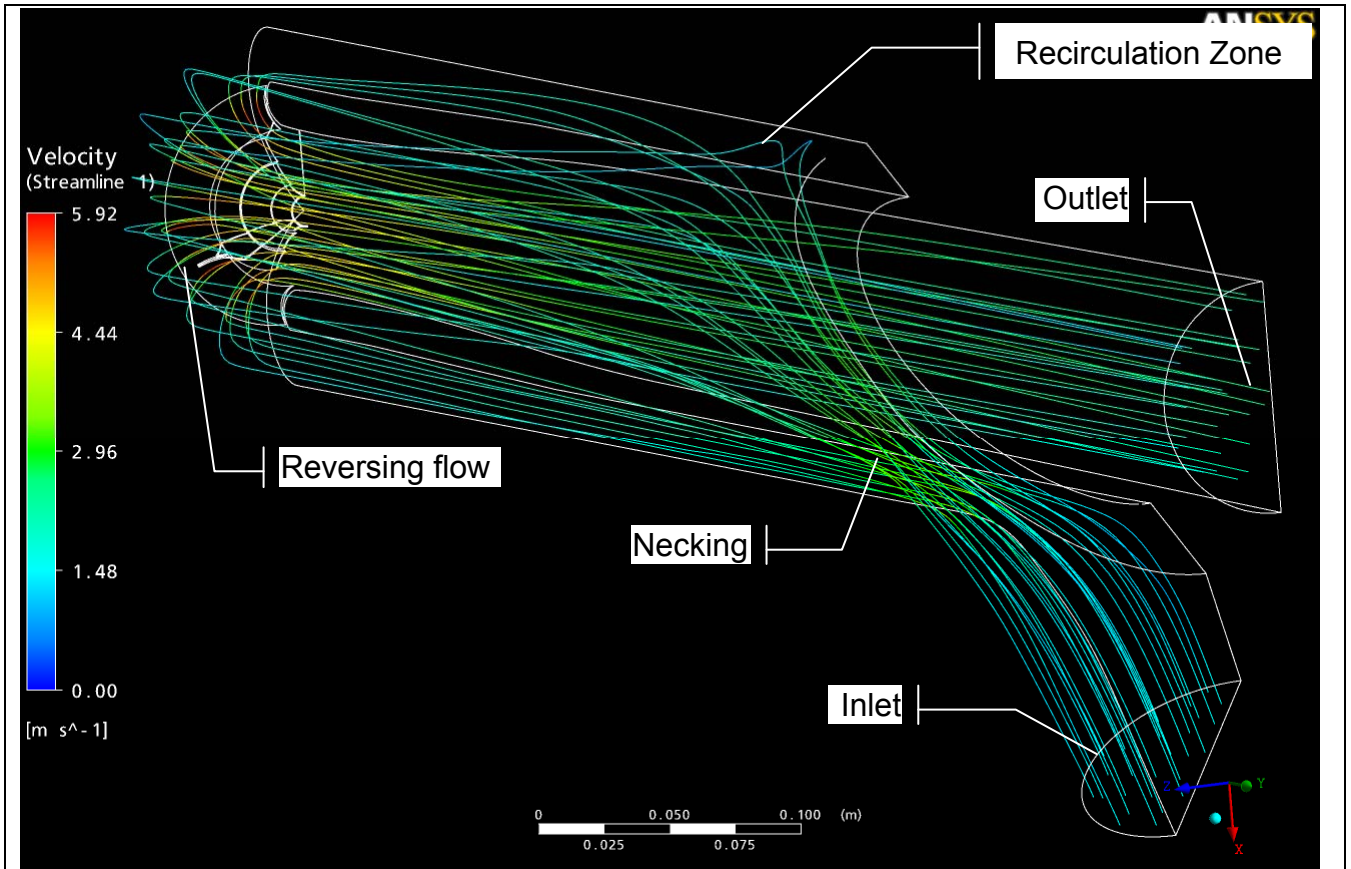
Figure 50: Flow pattern thru the converter target [Ref 19]

Figure 51: Static pressure at nominal flow on the model with vanes for the [Ref19]

Reference pressure: 0 Bar at outlet

2.5.2 Cavitation

Cavitation may be predicted from the CFD calculations shown in Figure 51 albeit with a caveat as the model does not include potential cavitation sources such as surface roughness. It would appear that cavitation does tend to occur at a lower pressure with the reverser in place due to high local velocities around the vanes. This effect may be abated by adjusting the static pressure accordingly, at the following values:
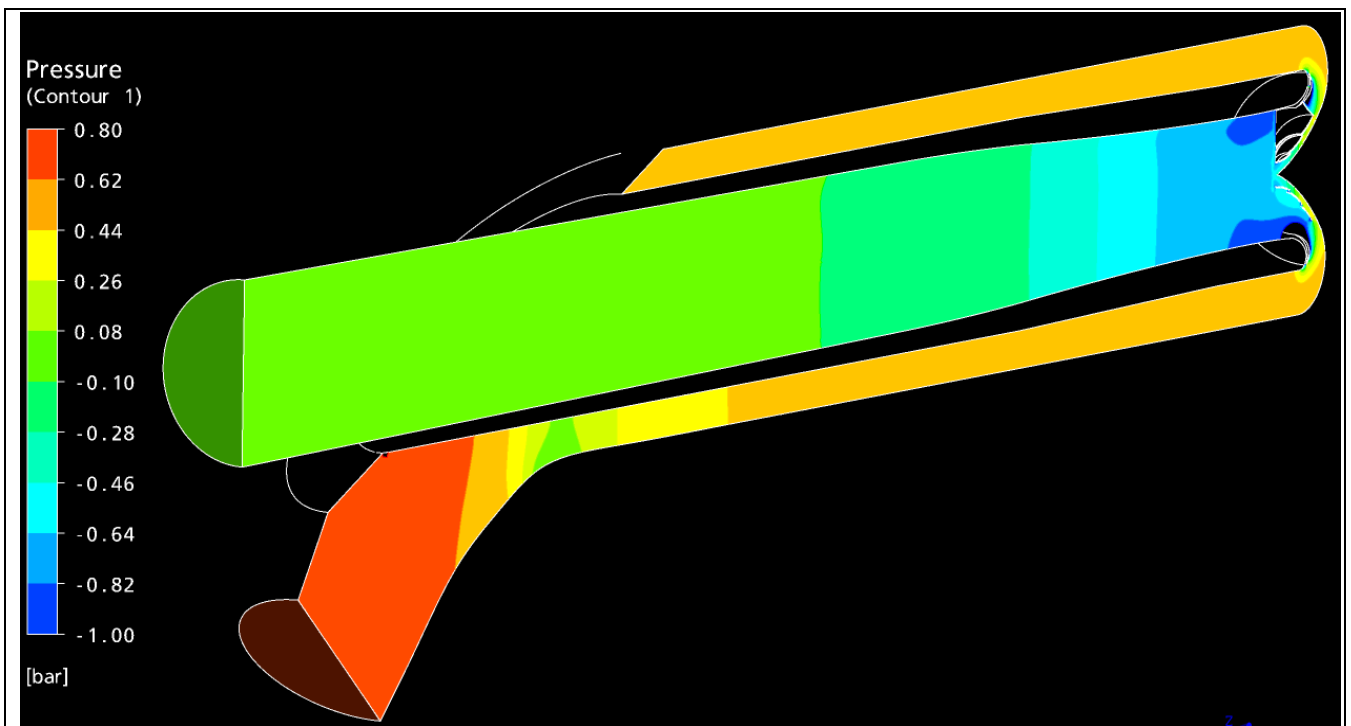
– Without blades: +1 Bar

– With blades: +2.6 Bar

2.5.3 Pressure loss

The target pressure loss refers to the pressure difference between inlet and outlet; it increases with the square power of the flow rate as shown in Figure 52. There are some inertia effects when accelerating the fluid which is initially at rest. This influences the calculations during the ramp-up to full power, but overall the power law hold true, and the instabilities can easily be filtered out.

The pressure drop at full power satisfies the overall system requirements. This experimental parameter was measured in the hydraulic test and serves to check the validity of the models used in the hydraulic design.

In the figure: Pressure drop [Bar] (y-axis), Flow rate [l/s] (x-axis)

$$\Delta P \text{ [Bar]} = 0.06 + 0.00365 \times (\text{flowrate [l]})^2$$
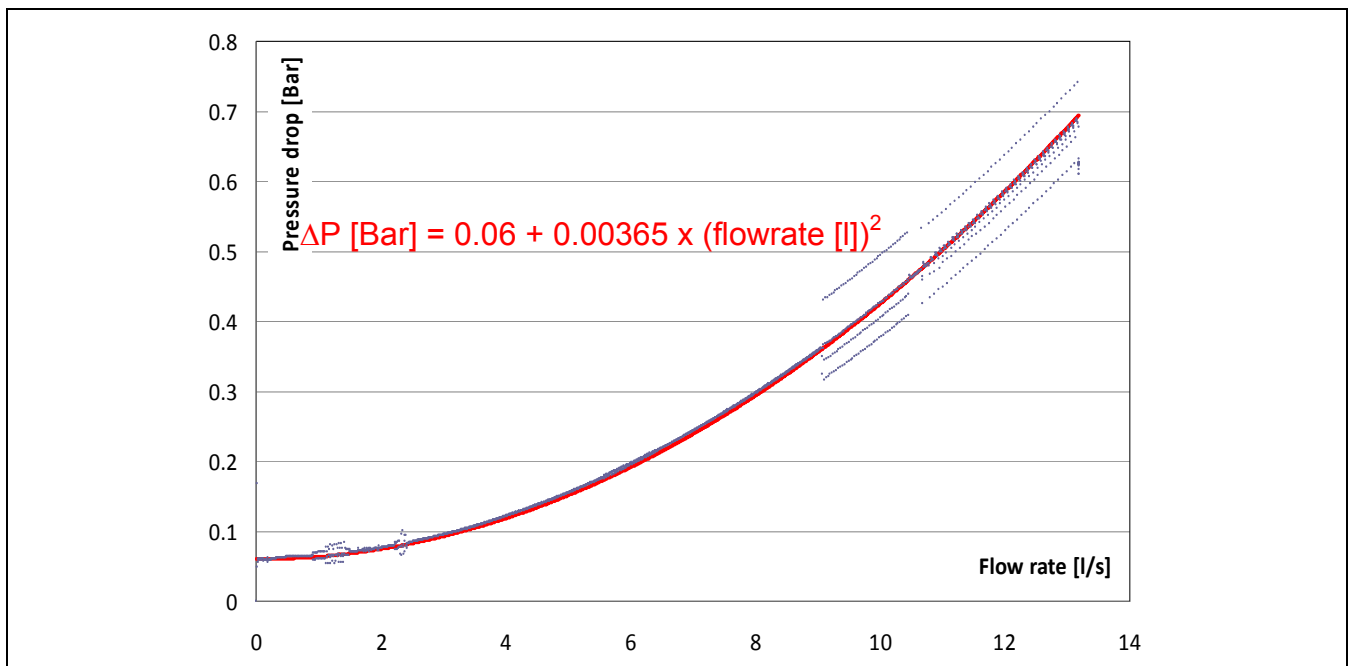
Figure 52: Predicted pressure losses in the target with flow vanes for the INITIAL DESIGN [Ref 19]

2.5.4 Pressure variations extracted from the global CFD model of the initial design

The full three-dimensional model was used to examine as the impact of pressure fluctuations on the structure. Naturally the difference between the CFD model and the as-built mock-up presented some difficulties. Nevertheless the window and guide tube were strictly identical as these portions of the target were not modified by the design office and it is precisely in these areas that the most severe turbulence exists. It was therefore considered that the CFD model would be representative in terms of pressure fluctuations, such as could be obtained from the LES turbulence model. The pressure fluctuations from the large-scale instabilities

are highest on the inner surface of the guide tube which is therefore more likely to be subjected to vibrations than the outer shell, where the velocity is both smaller and appears more stable.
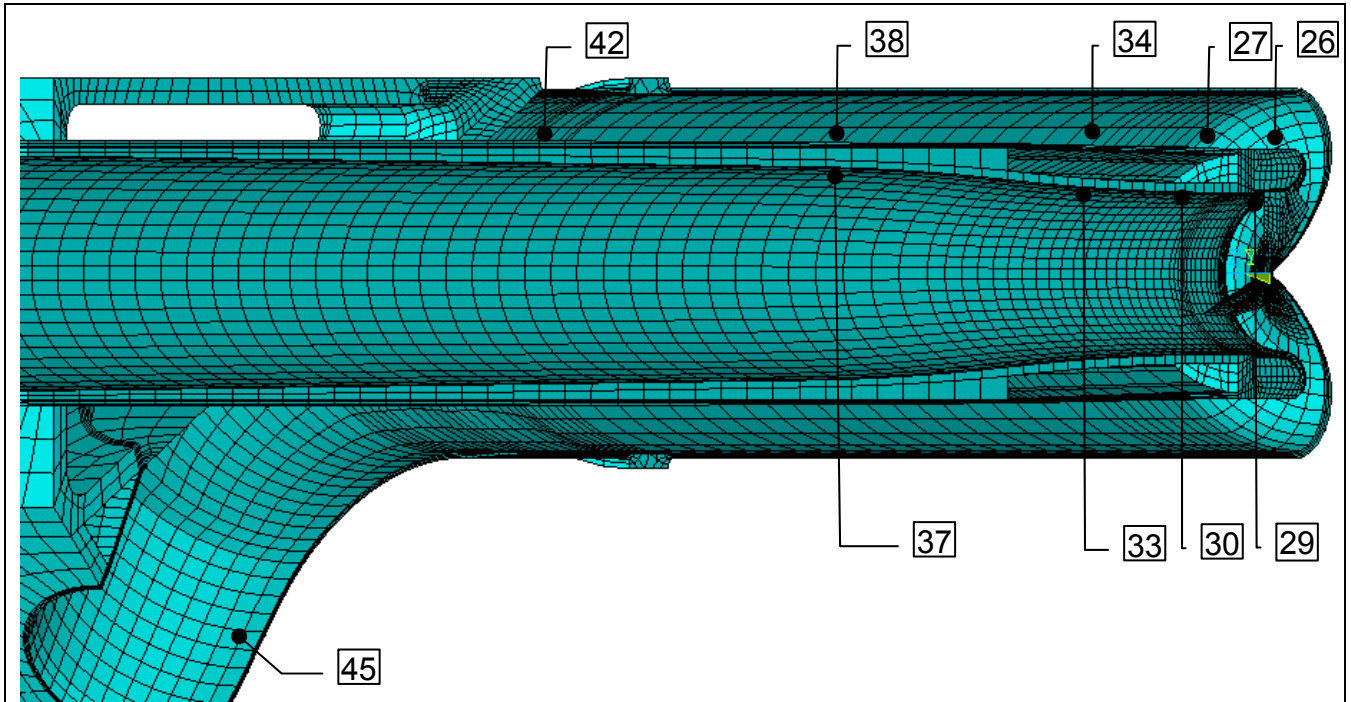
Figure 53: Diagram showing where pressure histories on the guide tube are extracted [Ref 19]
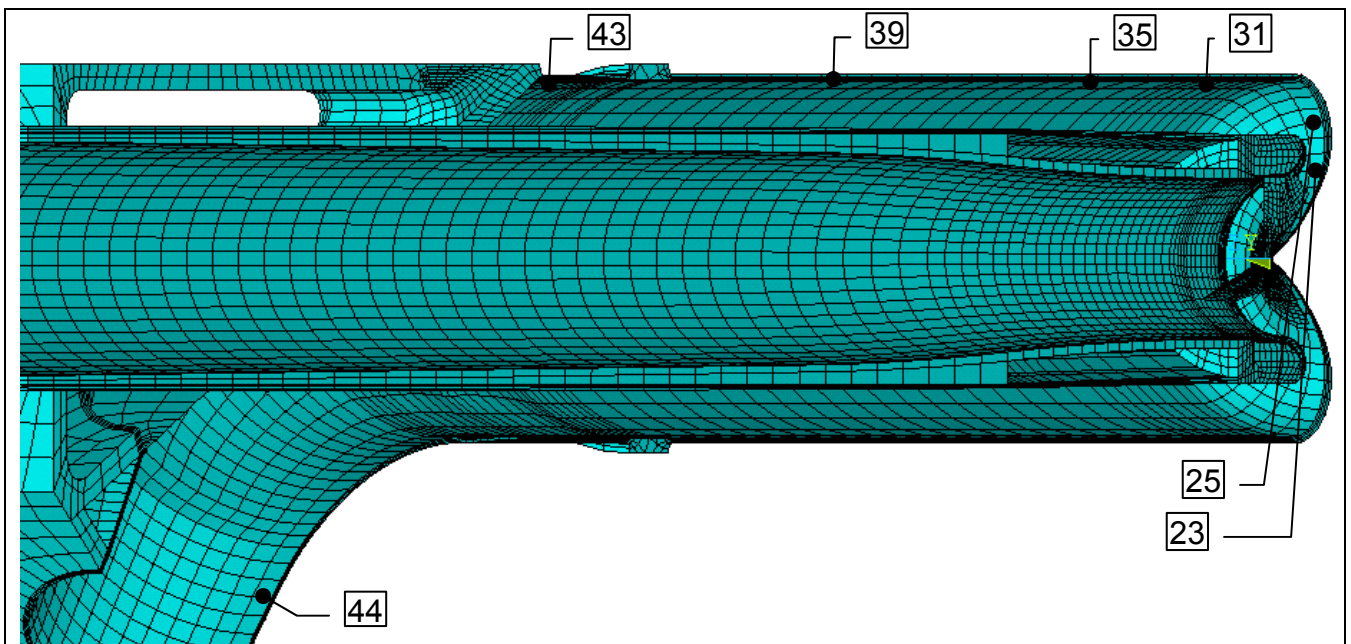
Figure 54: Diagram showing where pressure histories on the hull are extracted [Ref19]

The pressure histories on the points shown above are graphed in Figure 55 which shows that the largest pressure oscillations occur at the tip of the window. Next most affected by rapid variations in pressure are the inner guide tube, and finally the target hull proper which witnesses the smallest pressure disturbance.

One of the objectives of the hydraulic test is to record pressure variations inside the hull, in particular on the window where the amplitude of the pressure oscillation is highest. The goal of the direct measurement of the

time-history of the pressure is to validate the use of the LES turbulence model for liquid metal flowing at high speed.
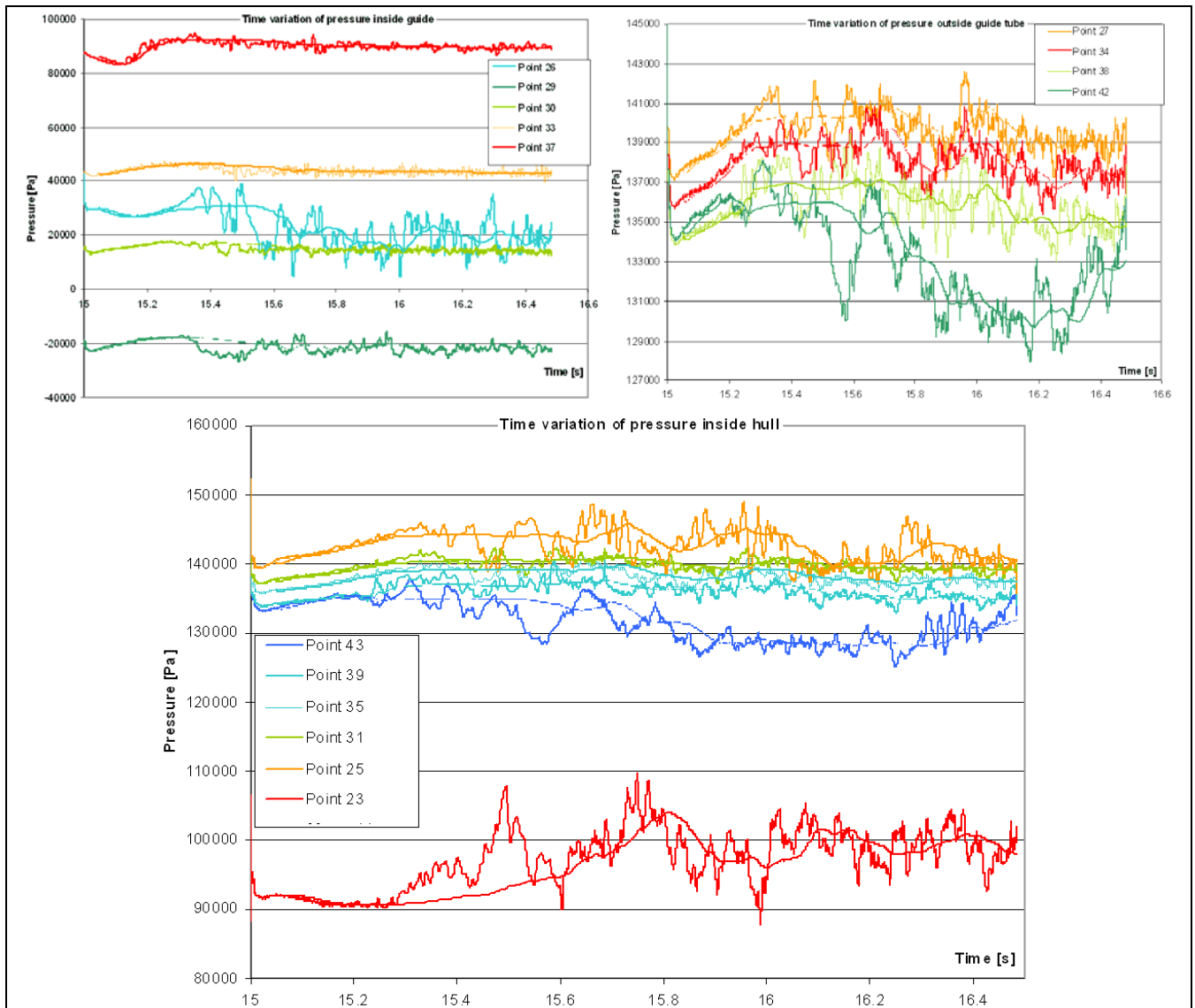
Figure 55: Pressure histories with moving averages on guide tube (top) and hull (bottom) [Ref19]

The pressure oscillations are critical to the structural coupling analysis described here above in section 2.4.5 which is important not only to validate the performance of the design but also its safety. Indeed, there has always been great concern that a resonance phenomenon might set in once the top speed in the liquid metal reaches 6 m/s. The velocity field during the LES simulation indicates a steady flow configuration over the window with the flow reverser but an oscillating detachment if the reverser is omitted. The structure in the outflow channel is also more unsteady without the flow reverser.

The pressure fluctuations from the large-scale instabilities are limited to the inner surface of the guide tube which is therefore more likely to be subjected to vibrations than the outer shell, where the velocity is both smaller and appears more stable.

The beneficial effect of the reverser seems therefore to be both in terms of limiting vibrations in the outflow and precluding cooling variations on the beam window which would have a detrimental effect on the lifetime through high cycle fatigue. (section 2.3.1)

2.6 Target operation outside nominal conditions

There are a number of cases not previously covered by the nominal σ = 15 mm beam load case, which are of particular relevance to safety considerations

2.6.1 Target cusp window under accidental conditions: flow blockage

The calculations have focused on the heat deposition generated by the σ = 15mm beam in the target under operational nominal conditions. There exists however a critical accidental case which must also be considered, namely when an obstruction in the loop or a puncture causes an immediate drop in pressure head, with the flow of liquid metal stopping instantaneously.

In such a case the heat removal capacity of the liquid metal is considered to be restricted to the amount of liquid metal contained by the target itself, as if it were disconnected from the loop. The liquid metal intersected by the beam will then heat up rapidly, and due to the expansivity of the metal will rise to the top of the target. The space intersected by the beam is then replenished with cooler fluid from the remainder of the target until all the liquid metal inside the target has reached a high enough temperature that internal natural convection ceases. At that point boiling will occur, followed rapidly by a pressure rise and rupture of the hull.

The previous calculations used a two-dimensional section model. In order to obtain natural convection it is necessary to add buoyancy and hence a direction for the gravity field, which makes the problem no longer axis-symmetric. Conservatively, and to gain a rapid estimate of the time to rupture, the section model is used assuming a gravity field along the diameter. This means the exchange of cooler and hotter fluid will only occur from the axis to the top of the target, and not the entire target as would be the case in reality.
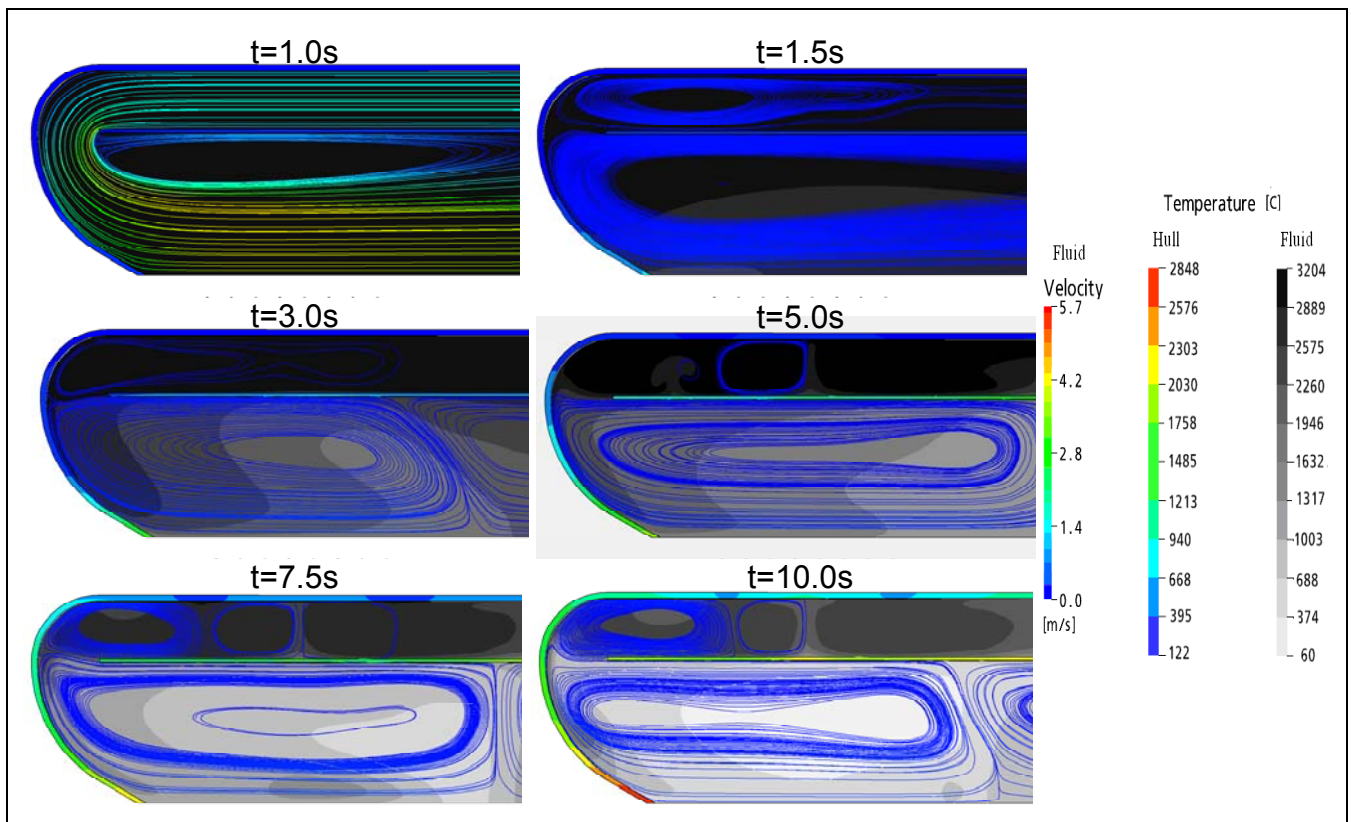
Figure 56: Resulting fluid temperature, velocities and hull temperature during a flow interruption for a target filled with mercury [Ref6]

The resulting pressure increase can be derived from the vapour pressure curve which is shown in Figure 14, it indicates that the 10 Bar design pressure limit will be reached in less than ½ second.

The rate of increase in the temperature of mercury is shown in the next figure, accompanied by the temperature rise from a target flow stop in a target filled with LBE. It indicates quite clearly that LBE has a greater margin against boiling in the event of the flow being suddenly blocked. LBE can tolerate full beam power with no flow condition for up to 6 seconds. This comparison centres only on the liquid metal and serves to weigh up the relative merit of each option. Another aspect of the problem is that the window heats up as well and may fail thermally before boiling inside the target is reached, although, the model is very conservative for the window as it does not consider cooling by thermal radiation back into the beam tube.
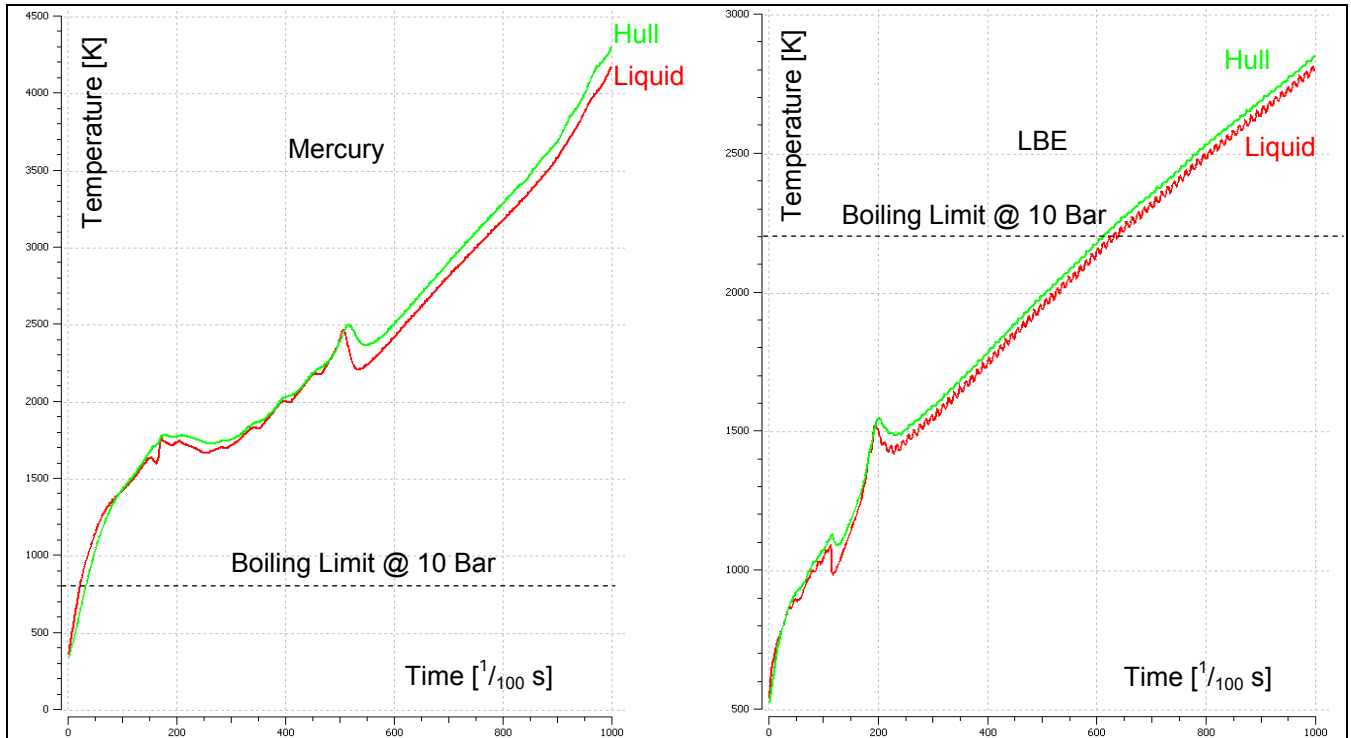
Figure 57: Increase of fluid temperature during a flow interruption for a flow stoppage [Ref6]

The longer time to reach boiling as well as the lower rate of increase of temperatures clearly favours the LBE option. The decision to use Mercury for all design studies early on in the project was motivated primarily by neutronic considerations (section 1.3) and the uncertainty regarding Polonium production (section1.5) and also the fact that keeping LBE liquid meant the entire loop would have to be heated and insulated.

2.6.2 Widening of the Beam

In order to enhance target integrity it may be interesting to increase the proton beam diameter from 15mm to 25mm, in order to reduce the local heat deposition of the beam in the window. This allows for either a reduction of the stresses and temperatures compared to the original design or an increase in the window thickness from the initial 0.8mm whilst aiming for the same temperature and stress as in the original design.

The analysis for optimising the window design for a 25mm beam focuses on the latter option, i.e. increasing the wall thickness whilst maintaining the same level of stress and temperature as in the original design. In this manner it is hoped that the design for a 25mm will be less susceptible to corrosion, fatigue and irradiation damage due to a larger number of grains through the thickness.

The 25mm beam is not the baseline option as the physics dictate a narrower 15mm beam, the larger beam may however be of interest in a broader context where a balance between safety considerations on the one hand, and striving for peak performance in the field of physics have to be struck.

The temperature distribution resulting from a 15 and 25 mm beam on the original geometry are shown in Figure 58 below:
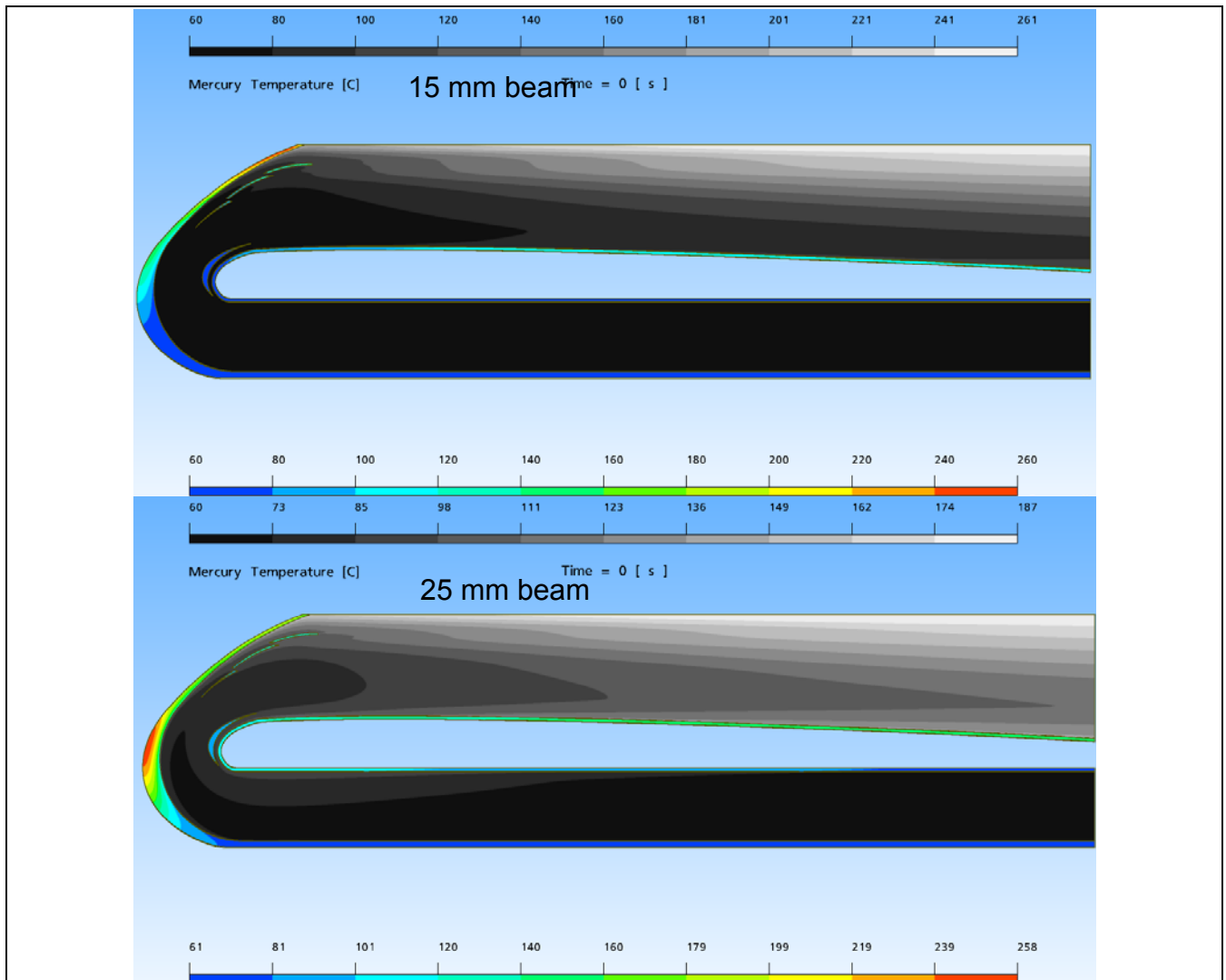
Figure 58: Effect of increasing the beam diameter on beam window optimised for a 15mm beam [Ref20]

The distinct temperature increase on the thickened section of the beam window is a direct result of increasing the beam. As shown in , expanding the beam creates another problem, in that the edges of the beam now impact the thickened section of the window designed to resist internal pressure and as a result generates high stress in that particular area.

Such a high temperature gradient along the outer rim of the window leads to a stress concentration. Clearly the shape of the window needs to be optimised to suit the wider beam Nevertheless, this issue can be solved by changing the geometry and shifting the thicker section radially outwards.

Decreasing the local intensity of the beam is however very beneficial to the window and the liquid metal temperature as shown in the figures hereafter. Indeed, the peak temperature in the liquid metal with a 25mm beam is 187 ºC, which is lower than with the 15mm beam, a decrease of 74 ºC

The thickness distribution is revised. Aiming for the same stress level as for the 15mm beam design, the thinnest part of the window optimised for a 25mm beam has a thickness of 1.4mm against 0.8mm for a 15mm beam design. Also the local stress raiser caused by the thickened section being impacted by the edge of the proton beam is eliminated and an optimised design for the 25 mm beam can thus be obtained. This goal is achieved by the shape shown in Figure 59.
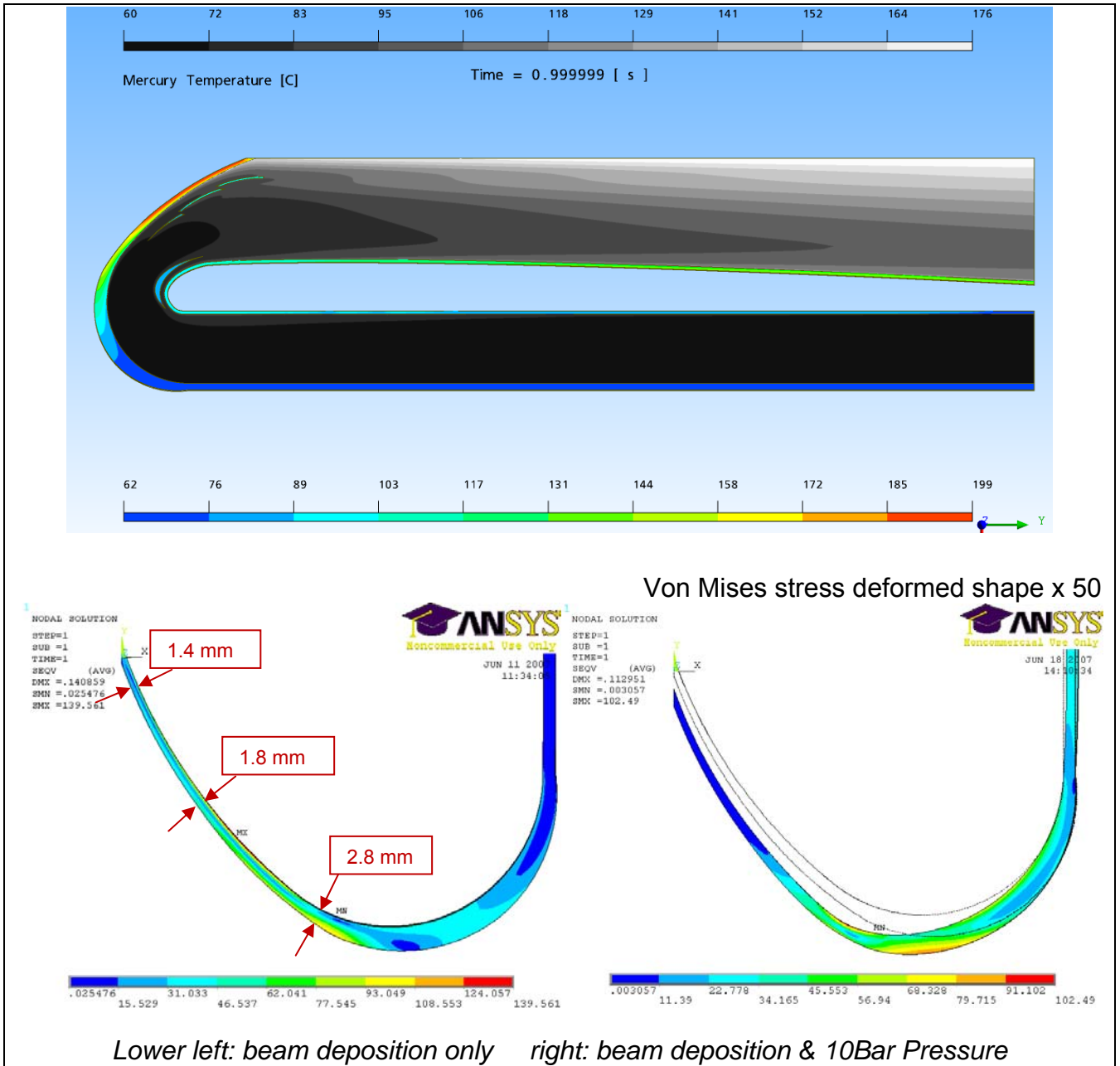
Figure 59: Temperature (top) and thermal stress (bottom) with 10 Bar internal pressure in the window optimised for 25 mm [Ref20]

2.6.3 Off-centre Beam

The possibility of the beam wandering off-centre needs to be examined as there is no guarantee that stability can be achieved at all times either in terms of the location of the beam or its intensity (The next section deals with beam interrupts). The calculation considers the beam to be static, positioned at a point 5 [mm] off-centre along the symmetry axis. The velocity at which the beam may be displaced from the window centre to the off-axis position is not considered in this calculation.

The effect of an off-centre beam is to change the stress pattern in the beam window, but also to cause possible variations in the flow patterns as buoyancy of the flowing liquid metal will be affected. For these reasons it is necessary to examine such effects in three dimensions (unlike the previous case). Hence the full

model of the window in 3D with half-symmetry is used and the offset is located in the symmetry plane. A value of 5 mm was seen as fairly representative of the worst possible deviation which would be tolerated before automatic shut-down systems step in to secure the beam line.
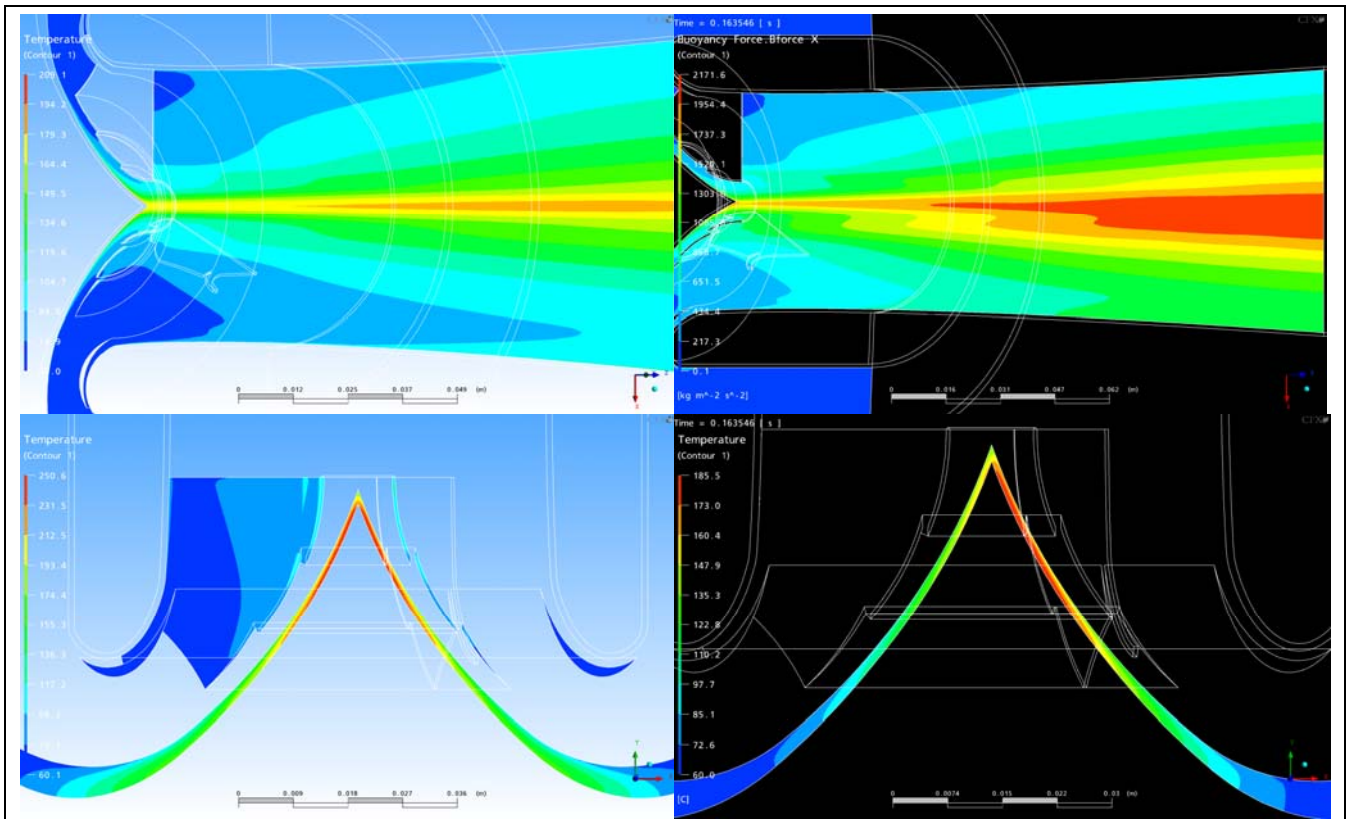
Figure 60: Temperature in mercury (top) and window (bottom) for the on-centre beam (left) and off-centre beam (right) [Ref8]
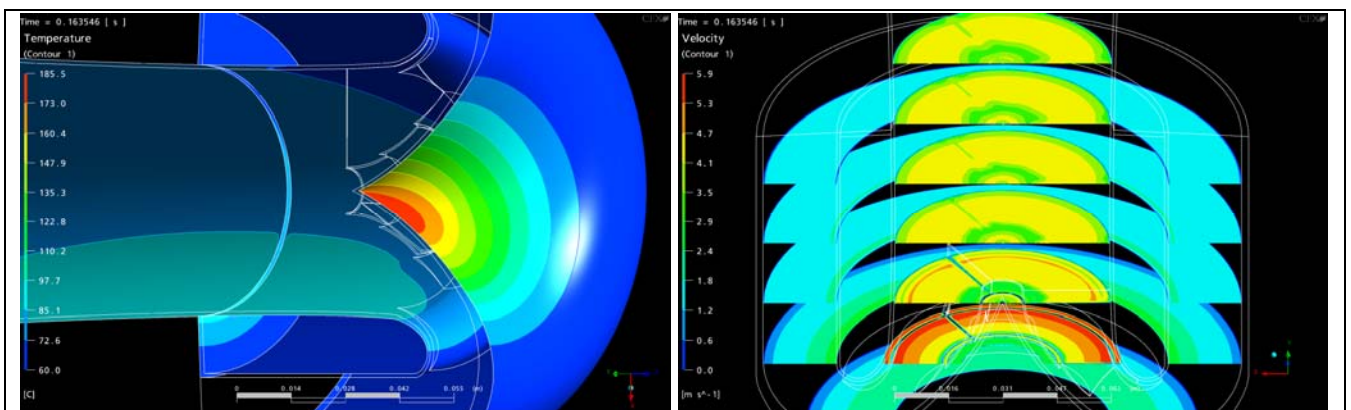
The effect of buoyancy is represented in the CFD model. The effect of the off-axis beam on the temperature in the window is immediately apparent. There is a clear shift along the symmetry plane in the peak temperature of the window towards the off-axis position of the beam, as shown in Figure 60.

Figure 61: Temperature in hull (left) velocity magnitude in Hg (right) for the off-centre beam [Ref8]

The magnitude of the temperature in the window and overall structure does not change however, compared to the on-axis case. The effect of the off-centre beam is clearly visible on the hull in the left of Figure 61.The streamlines are also of interest as the run is transient, and hence instabilities in the flow resulting from the off-axis position will show up. A section cut of the velocity field shown in Figure 61 indicates no serious perturbation from the off-axis position of the beam.

2.6.4 Pulsing of the Beam

Pulsing of the beam may occur voluntarily for time-of-flight experiments or may be the result of involuntary instabilities of the beam.

The deliberate pulsing is more constraining as the peak power is far greater; it is therefore retained for the study detailed in the current section. A thermal-stress analysis study of a pulsed proton beam with a pulse duration of 1ms and a 50 Hz repetition rate (pulse distance = 20ms) was found to be the most relevant from a physics point of view (cf. Table 1). The time-integrated density power remains at 4 MW on the target.

Figure 62 monitor the asymptotic temperature evolution at points of interest corresponding to a transient analysis performed with a 0.0001s time steps for a total time period of 2s, starting from no power. The three monitor points provide a clear visualization of the temperature changes relative to a pulse beam starting from cold conditions. The liquid metal experiences temperature variations of $\Delta T= 55C$ during a pulse cycle near the window (blue) whereas the outlet is more stable (red). A stabilized condition is reached in under 1s.
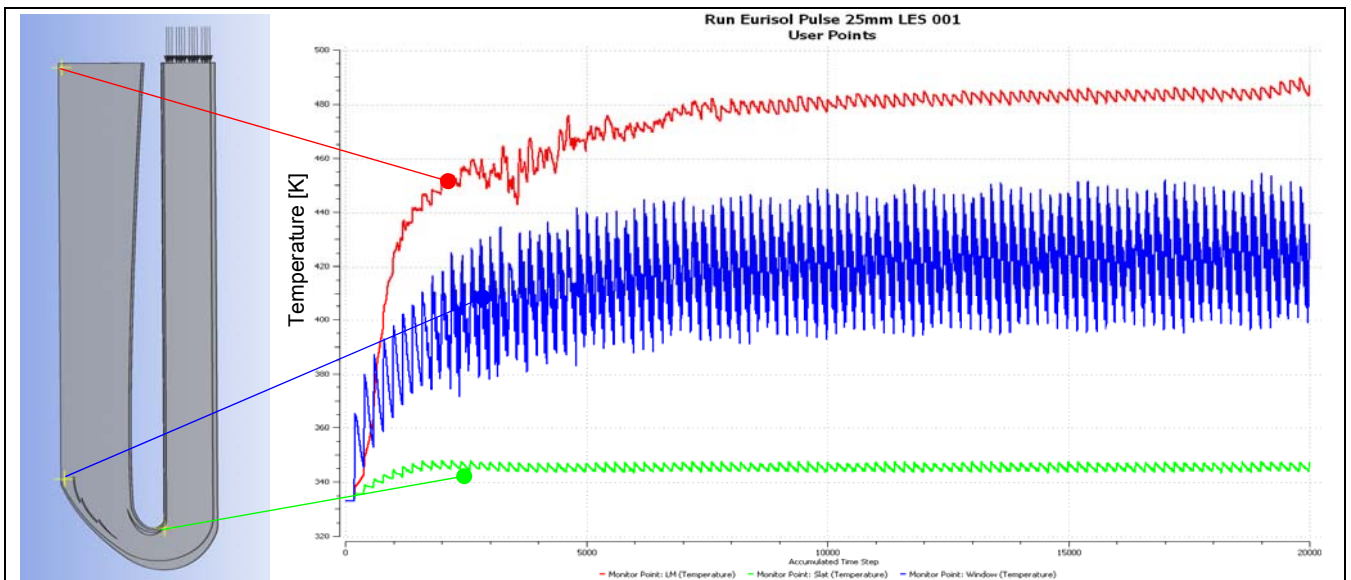
Figure 62: Temperatures monitored at critical points (left), reaching saturation (right) [Ref20]

In Figure 63, results show a time close to steady-state with a typical temperature, pressure and velocity flow, using an LES turbulence model. The pattern due to the pulse beam is clearly identifiable in the temperature field in the liquid metal, although pressure and velocities are not much affected. Temperatures and pressures are quite close to that of the continuous beam, although a pulsed structure is recognisable in the liquid metal.

Figure 63: Temperatures (left) pressure (right) field with a pulsed beam [Ref20]

The LES model should allow for detecting any large-scale structure in the flow field such as vortex shedding around the blades. This does not appear to be the case such that the configuration may be stable in a pulsed beam scenario. It should be emphasized that the effect of pressure waves resulting from the interaction of a sudden liquid metal expansion with a resonance in the structure is not included in this simulation.

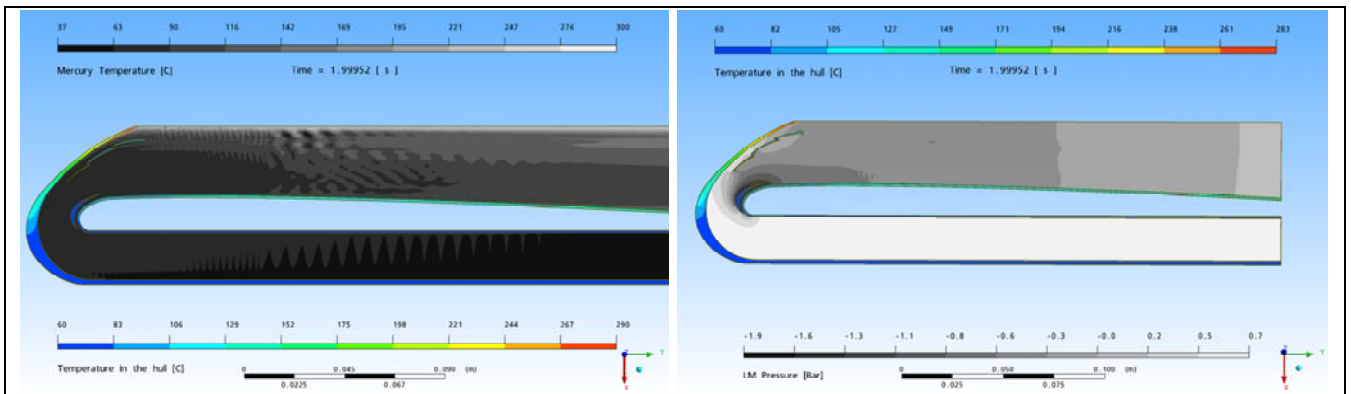The pressure and velocity flow fields, appear to be consistent with that of the continuous beam, the issue of thermal stress must be addressed. Ideally all the transient CFD steps should be transferred to a fully-coupled thermal-structural analysis. However, this complex problem can be simplified appreciably by focusing on a time segment which was selected when equilibrium has been reached.

Two monitor points were placed on the inner and outer wall of window where the window experiences the highest Von-Mises thermal stress. This is shown in the following temperature curves on the left of Figure 64 as a temperature gradient between the inner wall and outer wall. The temperature gradient starts increasing straight after the beam pulse until the next pulse is deposited, an effect of the cooling drawing out the heat of the pulse which creates an increased temperature gradient through the thickness. During the pulse, the temperature across the window section is saturated and is distributed homogeneously as there is no time to evacuate the sudden heat pulse, hence the gradient decreases slightly, although overall, the average temperature in the section increases. Then, after the pulse the inner wall immediately cools down through the effect of the liquid metal, hence the temperature gradient gradually increases, and it reaches a peak, when the next pulse is about to hit the window. Hence, the time that is of interest centres on just before and after the ramp-up of the pulse. It is precisely for this time-frame that the stresses were calculated as pictured in the right-hand of Figure 64. It should be stressed that in all instances stable flow was realised along the beam window as this is a pre-requisite for evacuating heat from the pulse (cf.Figure 20).
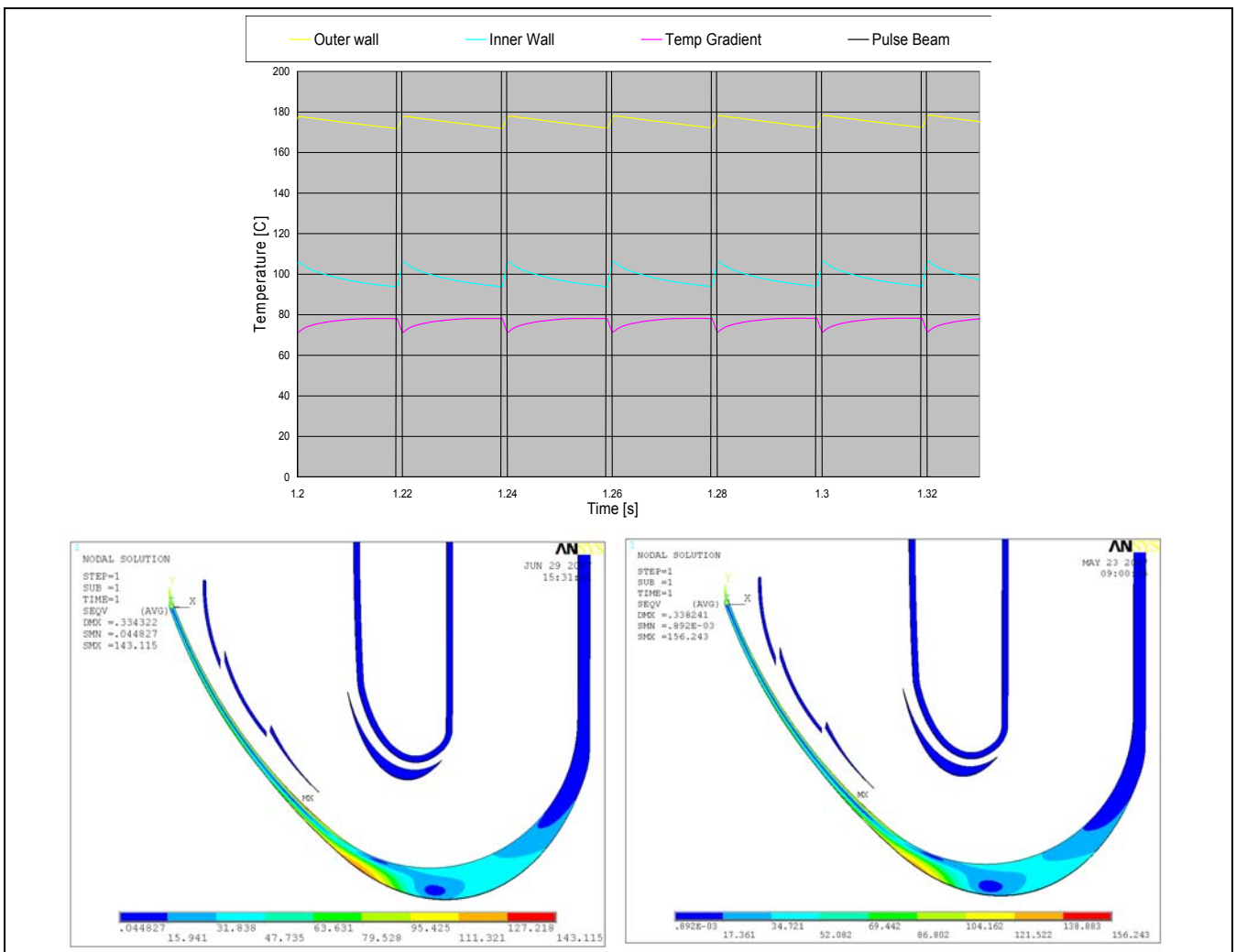

Figure 64: Temperature curves characteristic of the gradients in the window (top) Von-Mises thermal stress in the window at equilibrium (right) before (left) and after (right) pulse [Ref20]

2.7 Manufacturing of the converter target

2.7.1 Inlet / Outlet channel and thermal barrier

Insulating the cold inflowing LM from the heated outflow is necessary to facilitate heat extraction from the converter target but it is also complicated due to space limitation imposed on the design. In addition pressure losses must be minimised because of the restrictions on the pump. The solution to this particular problem relies on LM flowing into the target from below at 40° to the horizontal to improve hydraulic efficiency. The inflow is thermally insulated from the LM flowing out by a double-walled guide tube structure, the cavity between the two walls being filled with air.

The double–walled guide tube is essentially manufactured from an inner machined barrel with ribs on the outer surface over which a simple outer tube is positioned and welded in position (see detail in Figure 66). Thus the only full thru-metal thermal passage from the outflow to the inflow side occurs along the ribs, which represent less that 10% of the total wetted surface. Although this design does not eliminate thermal cross-flow entirely it does limit the extent of the problem.

The inflow channel is defined by the outer shell (in yellow in Figure 65) of the guide tube which is welded to the support piece (magenta) as shown in the figure below. Then the inlet tube (orange) is welded on the support piece. Thus the inflow channel is formed whereby the LM entering through a circular pipe section flows either side of the guide tube and then co-axially towards the window.
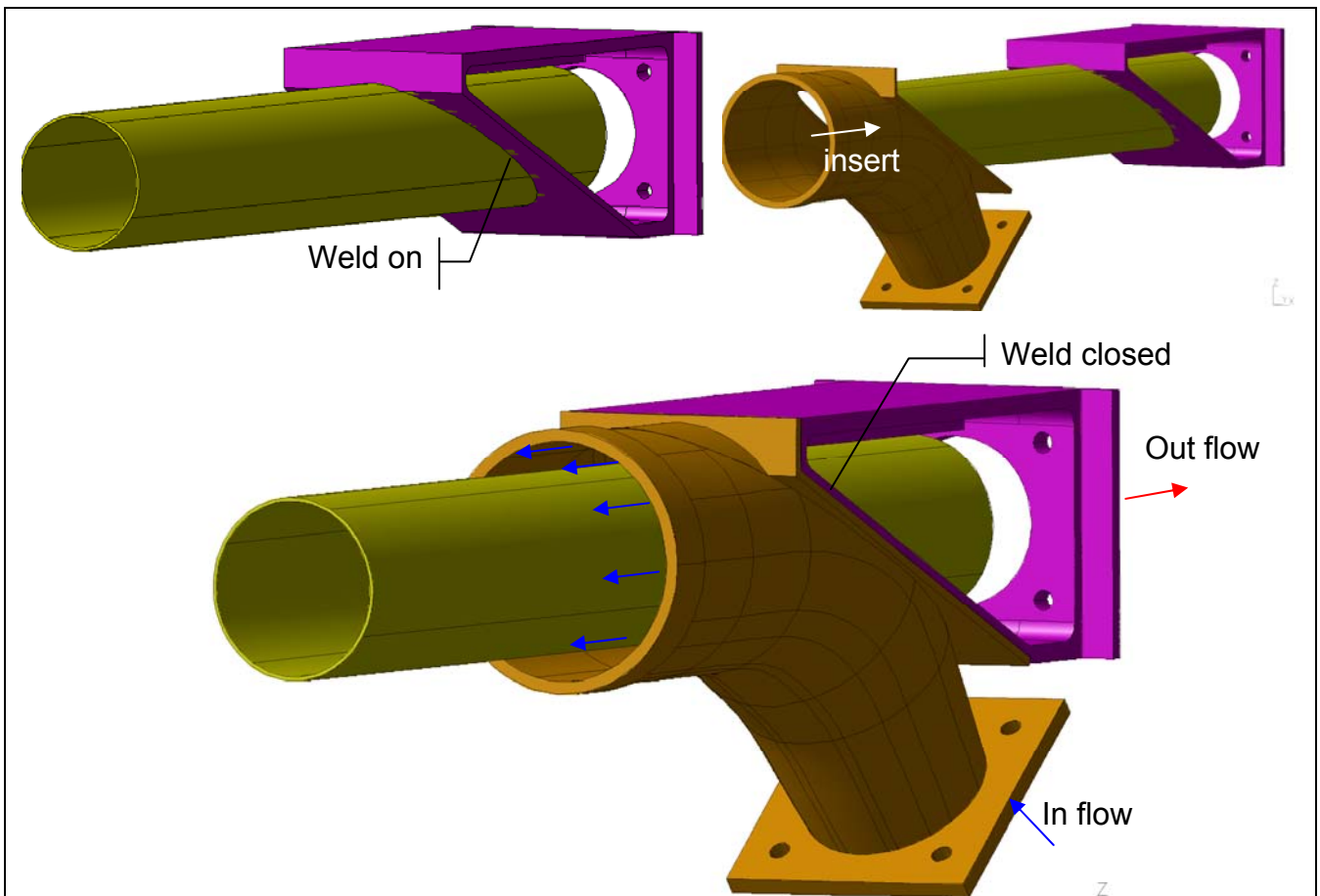

Figure 65: Manufacturing of the inlet channel [Ref8]

The return flow of LM towards the back of the converter target is directed by the inner guide tube (in gray in Figure 66 below). The guide tube is essentially hollow, formed by an outer cylindrical tube (yellow in Figure 66) which is welded onto the machined inner guide tube. The ribs of the inner guide tube maintain a small thermal gap between the outer cylinder and the inner guide tube (detail in Figure 66). In addition the inner guide tube features three channels spaced out at 120° which serve to house the instrumentation cabling leading back to the rear of the target where transducers for the pressure pick-ups and electronic data gathering are located. The fore part of the guide tube has a large cavity to prevent heating from the proton beam.
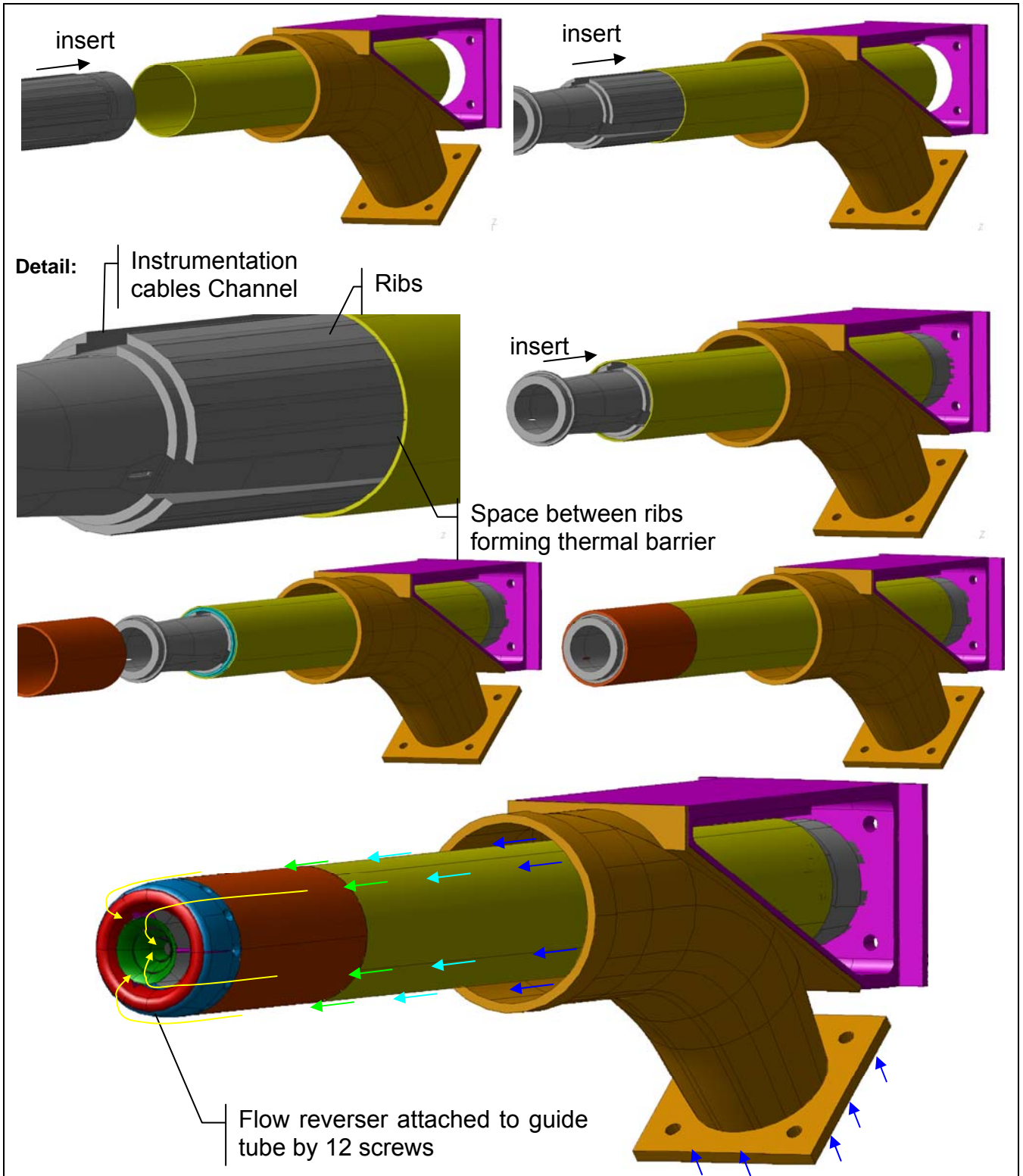
Figure 66: Integrating the inner guide tube (left to right, top to bottom) [Ref8]

2.7.2 Flow reverser

The purpose of the flow reverser is to turn the flow 180° with minimal pressure loss. At the same time it should encourage convective cooling by accelerating and attaching the flow locally over the window. For testing purposes the flow reverser is detachable from the fore end of the guide tube. The reverser resembling a cowling attaches to the guide tube by a dozen screws at a 30° pitch, which enables the assembly to be rotated by 30° relative to the static instrumentation inside the guide tube. Thus by simply rotating the flow reverser, different velocity profiles of interest can be measured either between or directly behind the 3 supports.

Figure 67 below shows how the reverser is manufactured. First, the 3 supports for the flow vanes are held in a fixture in three matching slits spaced out at 120° Once the supports are in place the vanes immediately adjacent to the guide tube (shown in red below) can be welded on by two 45° angle either side of the support. It is thicker in section than the window vanes and has a dual purpose; on the one hand to help bend the flow back into the guide tube, but also to reduce cavitation risk on the back-swept part of the guide tube by encouraging reattachment of the flow.

Then the window vanes (in green) are also welded to the support using again angle welds. The window vanes are intended to accelerate the LM locally over the hottest part of the window where the proton beam enters the target. Initially the window vanes form a single funnel shaped piece (not shown here). The slits between each individual vane are only machined in after the vane funnel has been welded on. The basic idea is to prevent distortions during welding, as the whole funnel-shaped piece ought to be stiffer than 3 separate vanes.

Finally the fixture holding the supports is removed, and the supports are inserted in corresponding slits in the cowling (in blue) before being finally welded in place.
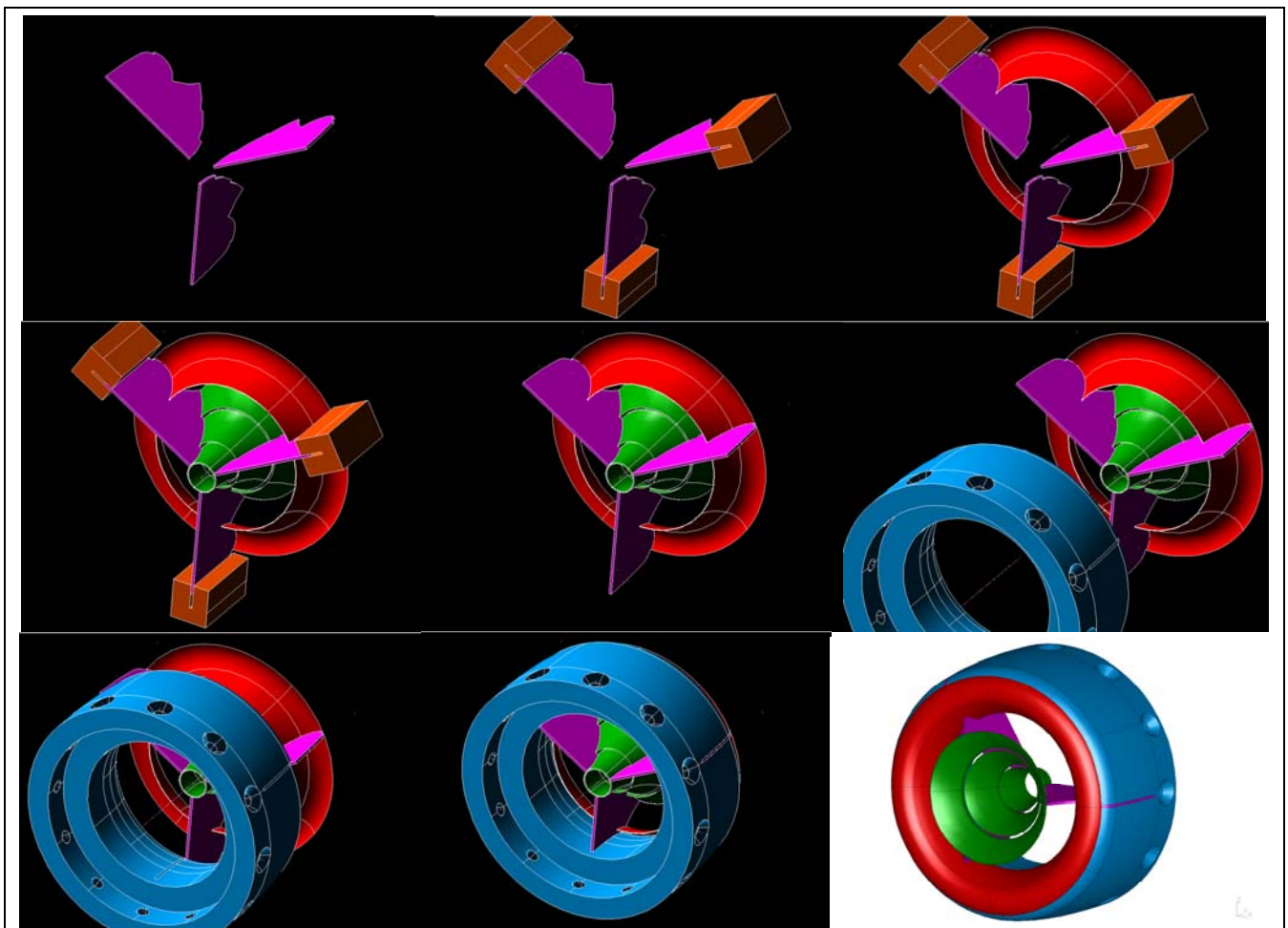

Figure 67: Steps in manufacturing the integrated flow reverser unit (left to right, top to bottom) [Ref8]

2.7.3 Instrumentation

The current instrumentation is only relevant to the target manufactured for advanced hydraulic testing. It is not intended for the production unit which will at most contain a few thermo-couples, and no velocity profiling. Neither has the proposed instrumentation been implemented in the series of hydraulic test performed at IPUL in January 2009 and documented in [Ref12]

The method for measuring the velocity profiles relies on conventional Pitot tubes housed in winglets which are inserted at three stations along the return flow in the guide tubes as shown in Figure 68 below with the tubes running towards the rear of the target in dedicated instrumentations tunnels, this instrumentation harness is repeated three times around the circumference, spaced out at 120° intervals.
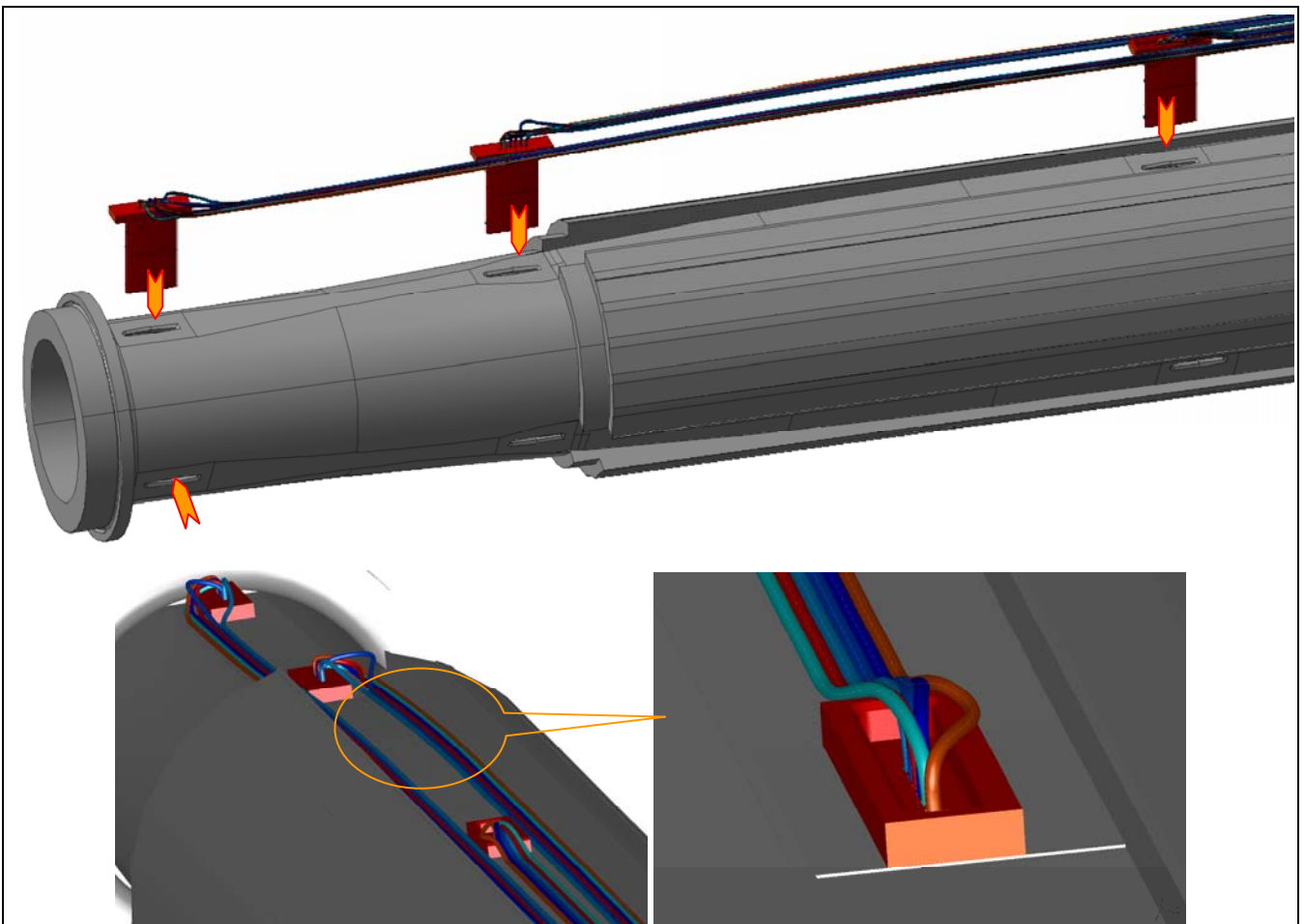
Figure 68: Positioning of the instrumentation in the guide tube [Ref8]

The winglets contain not only capillary tubes for pressure pick-up but also thermocouples so as to resolve the thermal boundary layer as well as the velocity boundary layer.

The thermocouples and capillary tubes are both 1 mm in diameter and sufficiently pliable to be bent around tight radii. Nevertheless, care must be taken when routing the tubes particularly at the rear station where the thickness of the guide tube is very much reduced and does not offer much space. As shown in the bottom right of Figure 68, it may be necessary to hollow out the pad on the rear most winglet to give sufficient space for bending the tubes.

The winglets may be placed in line or separate tests may be dedicated for measurements with winglets at each station separately. This may be needed to avoid having the second station adversely affected by the downwash from the first station. It is also possible from a design point of view to offset laterally the centreline of the second winglet by about 10 mm from that of the first. Another possibility is to create a set of

---

instrumentation tunnels every 60° so as to place the second row of winglets 60° offset from the first and last row.

The following figure gives some insight into the manufacturing and internal details of the winglets containing the pressure pick-ups and thermo-couples. All pressure measurements are made at the rear of the target via the capillaries which run out to pressure transducers. On each winglet there is a pressure pick-up in the dead zone at the base of the trailing edge to measure static pressure. There are three pressure pick-ups on the leading edge so as to resolve the velocity boundary layer.

In addition two thermocouples; one near the wall and one closer to the centreline allow measurement of the thermal boundary layer, when tests with heated LM are carried out

The manufacturing of the instrumentation winglets is illustrated in Figure 69, starting with the placement of the thermo-couples and capillaries in grooves that have been previously machined in a flat plate. A second plate is placed on top and the whole assembly is brazed creating a solid block using high-temperature soldering techniques. Care must be taken during soldering not to obstruct the capillaries with flux; this may be prevented by allowing a small extension length of capillary out of the block which ensures they remain open after they have been machined back.

Finally the soldered block with the imbedded capillaries and thermo-couples can be machined in the shape of a winglet with an attachment pad, all the tubes protruding from the lower end of the pad.
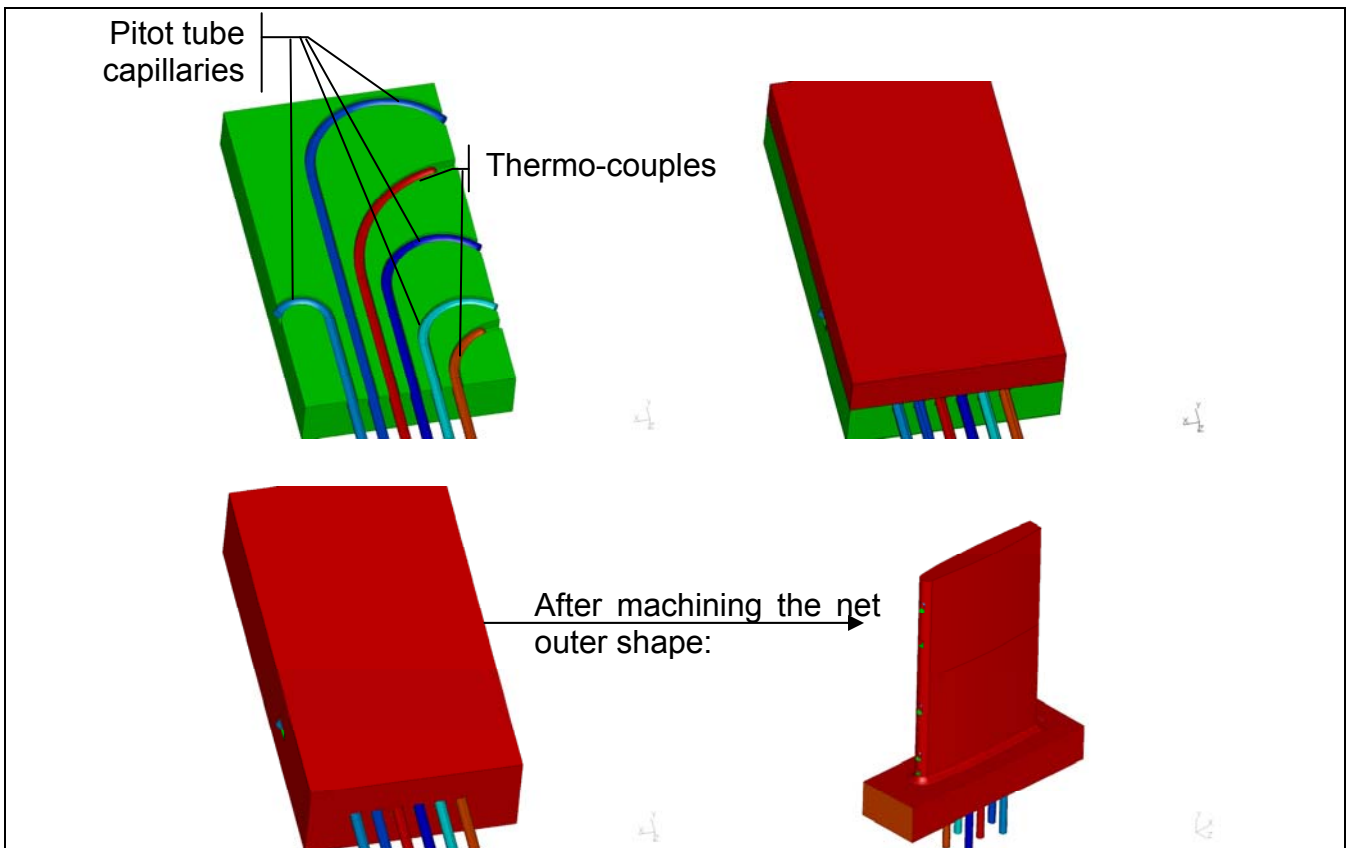
**Figure 69: Steps in manufacturing instrumentation winglets (left to right, top to bottom) [Ref8]**

2.7.4 Outer hull

The outer hull is simply welded on to the inlet tube at a thickened section. Although the final strategy for the window has not yet been decided it may be feasible to foresee a bolted flange in lieu of the weld as this may facilitate the exchange of damaged outer hulls, particularly in the window area.

Overall, the nature of the connection from the outer hull to the inlet tube does not affect the hydraulic performance inside the target, hence the present design study does not consider it in any greater detail, but leaves the choice open to the draughtsman as to the exact nature of this interface, bolted, welded or indeed even secured with a belt-clamp.

The exact dimensions of the window hull shape have been derived with a full thermal-hydraulic analysis for a σ 15mm beam, some preliminary work exists for a σ 25mm beam indicating the minimum thickness could be increased from its current value of 0.8 mm at the tip of the cusp to about 1.7 mm. The main differences are summarised in the figure below for completeness.
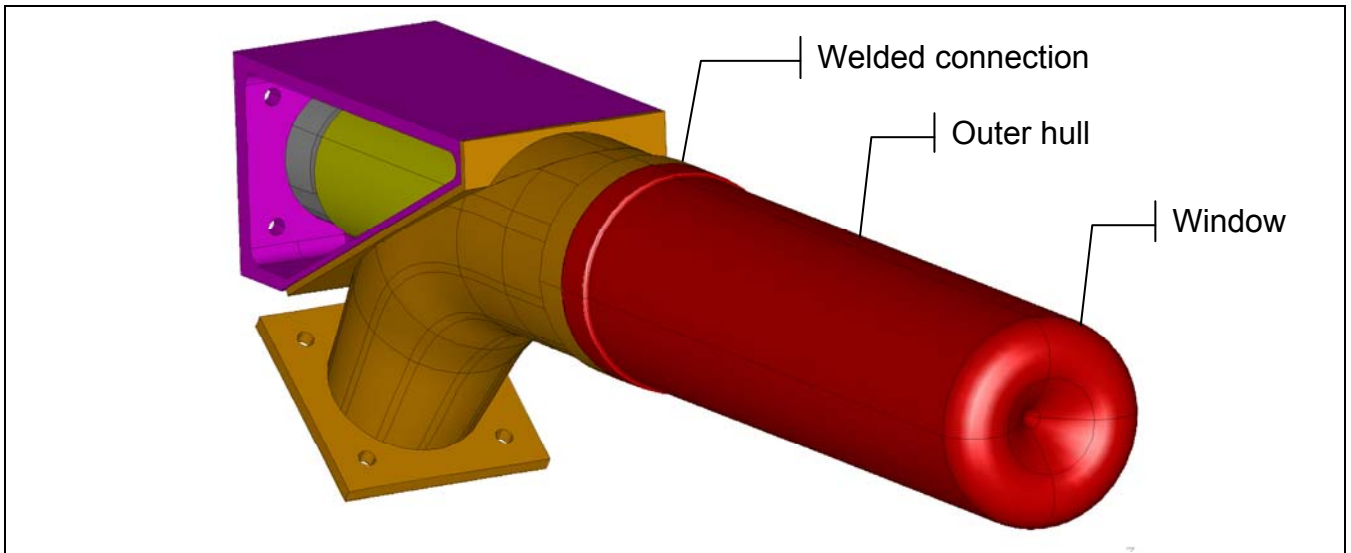
**Figure 70: Design of the outer hull [Ref8]**

3 The WTF windowless target

3.1 Conceptual features of the window design

An alternative windowless design was also developed, to avoid the technical difficulties related to the beam window, also presenting several advantages in terms of neutronics. The transverse mercury film would fall by gravitation, interacting with the proton beam to produce spallation neutrons and efficiently removing the beam power with reasonable flow rates. The most relevant benefit of such design is the brief exposition of the liquid metal to the proton beam, thus permitting an accurate control of the temperature in the liquid metal.

Within EURISOL – DS, a liquid metal spallation target with a power of several Megawatts is designed to provide neutrons to a fission target. The target station that allows the full intensity of a 4 MW proton beam to be used for RIB production will require new advanced technology. It is a critical component of EURISOL. For a power density over 10^3 MW/m^3, the windowless, free – surface, molten LM-jet is proposed as a target since it avoids the very serious lifetime –shortening damage caused by the power proton beam in a system with a window. In the case of the spallation neutron sources, mercury has been chosen as the most promising high-Z target and coolant material.

There are many advantages to a windowless liquid metal (LM) target, as has been recognised by collaboration agreements within the framework of EU Research. In the SINQ facility at PSI the proton beam is bent upwards by special magnets. In principle, the beam could be bent also downwards and aimed at an open liquid metal free surface. A project in this configuration was spearheaded by IPUL in collaboration with the Belgian Nuclear Research Centre (SCK) as part of design and verification experiments for a Windowless Spallation Target for the ADS Prototype MYRRHA. This application was intended as a small high-performance irradiation facility with fast neutron fluxes up to 10^{15}n/cm²/s.

Operating a liquid metal target without a beam window is markedly different to that described in section 2 for the window target. The separation between the liquid and the beam line is materialised by a separate beam window located at a fair distance to the liquid metal and which is not the focus of this study. The windowless target itself is described hereafter; focusing on the trajectory of the beam intersecting the liquid after the beam has entered into the target section.
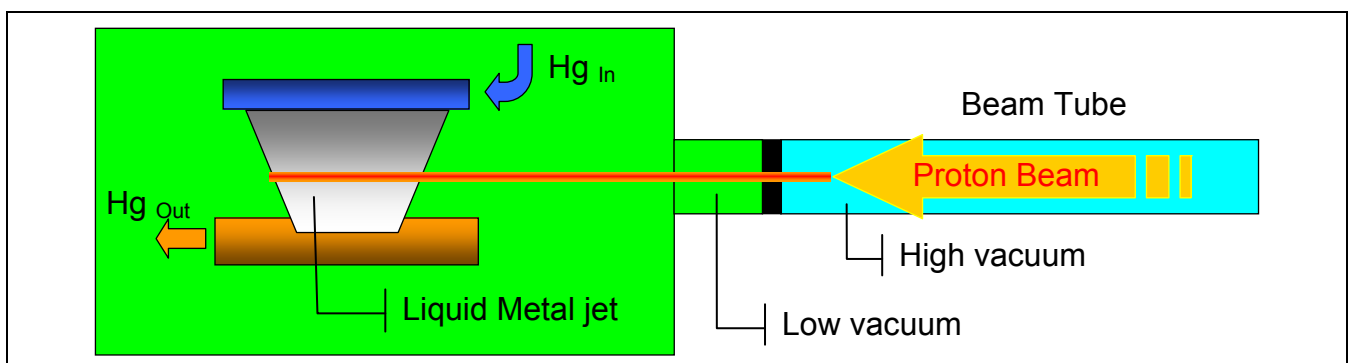
Figure 71: schematic of windowless target

The EURISOL windowless target tested a concept shown at the top in Figure 72. The target injector is at the centre of the target and consists of three sections, which provide different velocity of flow in each section depending of the heat dissipation required in these regions.

The velocity difference can be adjusted by different hydraulic resistance in each section of the film former; such an injector can be seen in the bottom left of Figure 72.

There is another possibility to create a different flow rate in each section by providing separate Hg inlet for each section. It would complicate the construction of the target, increase weight and the number of welds. Nevertheless experiments on the IPUL Mercury loop show that such a concept can create an adjustable velocity in each section. This "Speed tailoring" can decrease the amount of mercury needed to dissipate the heat of the beam. So it is possible to use a smaller pump, which results in saving weight, energy which in turn will reduce the dimensions of the Hg loop.
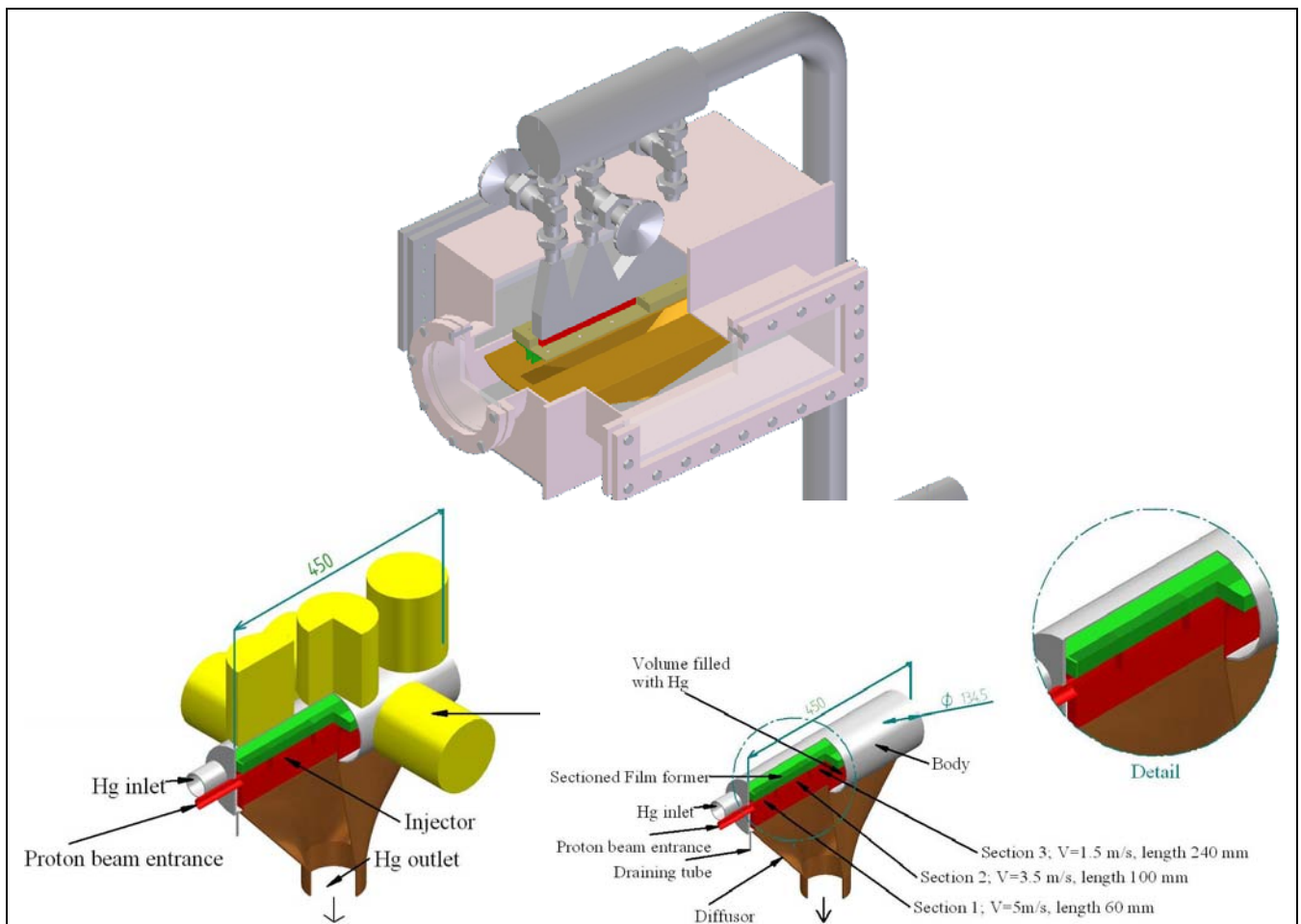

Figure 72: IPUL concept featuring different injector speeds [Ref14]

3.2 Power Deposition and Thermal Hydraulic Design

3.2.1 Heat Deposition in the WTF target

A critical issue for the design of a high-power spallation source is the energy deposition in the different elements of the target. Neutronic calculations using a quasi pencil-like beam (σx,y~2 mm) were carried out, the very thin beam serving to improve neutronic efficiency as explained in section 1.3.4. For thermal-hydraulic studies, interest focuses on the peak power density in order to verify the WTF converter concept may evacuate the deposited heat safely.
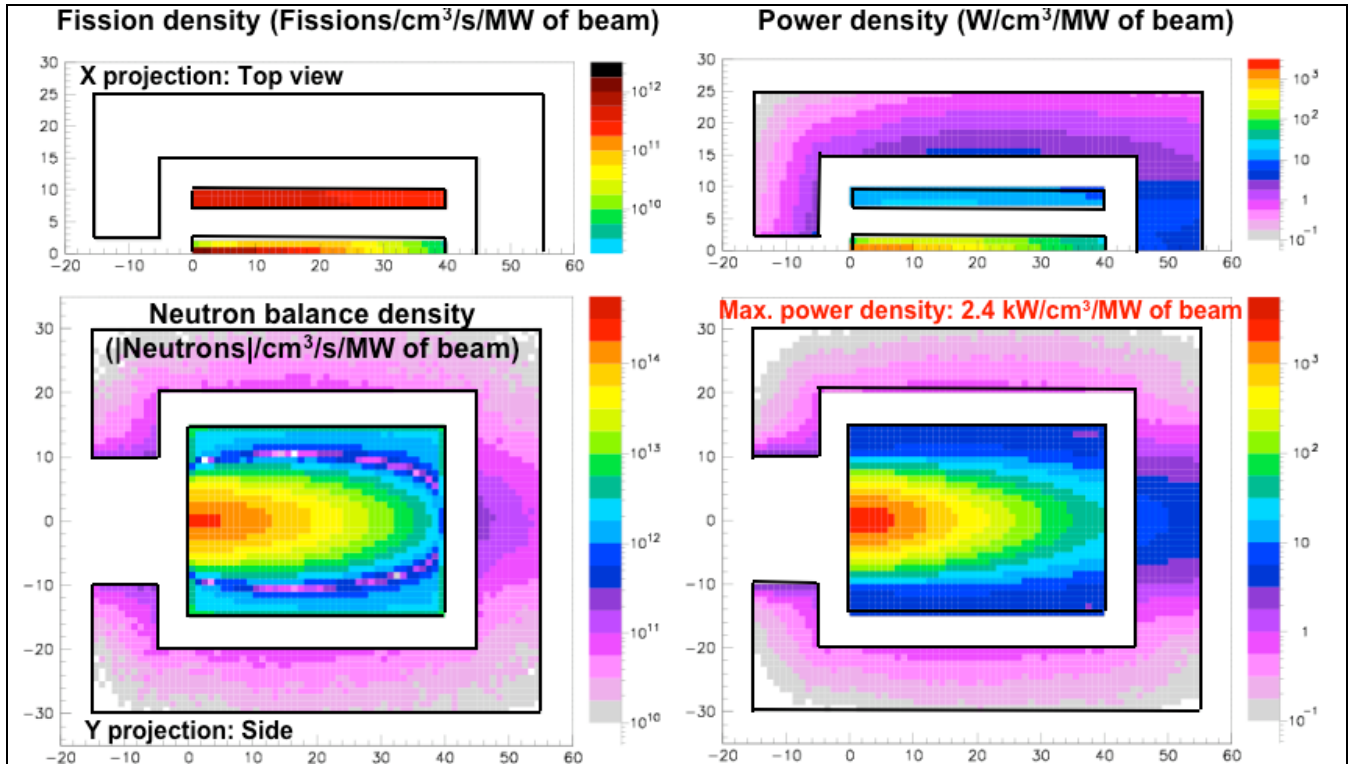
Figure 73: neutronic characteristics (left) and power density (right) for the film target [Ref4]

The beam particles considered are protons with an energy of 1GeV, a Gaussian distribution with a standard deviation of 2 mm in both x and y directions. The dimension of the target is 40 cm in length, 4 cm width and 30 cm high. Figure 74 illustrates a view of the target along the proton beam axis.
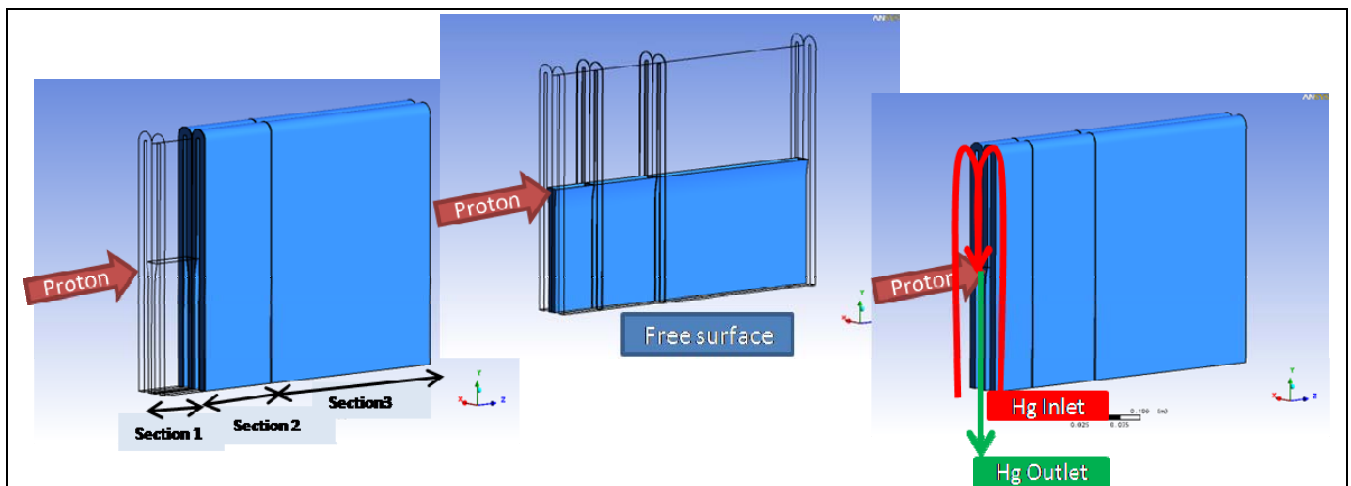

Figure 74: 3D cut view of the target [Ref17]

For 1 GeV protons, the largest power deposition occurs in the first 10 cm after the beam impact, along the beam axis, as illustrated in Figure 75, with a maximum value of ~80 kW/cm^3/MW of beam power at ~0.5 cm from the impact point. Once the proton range is reached, the power density drops sharply, to values below 500 W/cm^3/MW of beam. Large deposition gradients appear radially in the interaction region due to the narrow beam shape.

The maximum energy deposition calculated in the target is 0.08 GeV/ cm^3/proton which is equivalent to 80 kW/ cm^3/MW of beam. Therefore, in the case of a 4 MMW beam, the peak power density corresponds to 320 kW/cm^3.
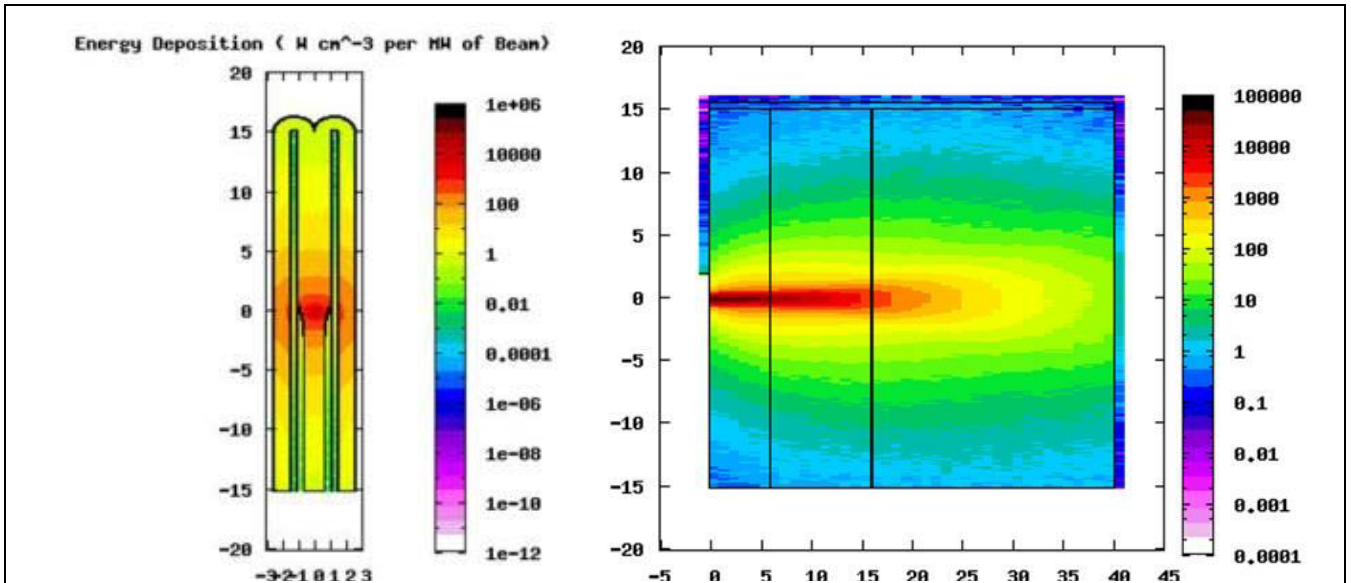
Figure 75: Power density (GeV/cm3/primary) in a Hg target for a 1 GeV proton beam. [Ref17]

3.2.2 Temperature distribution in the WTF target

A model has been set up in Ansys-CFX representing only the fluid around the beam and on which the inlet velocity has been changed to different value in order to estimate the minimum mercury flow velocity required to minimize the peak temperature. Figure 76 shows the mercury temperature and velocity in the symmetry plane. The peak temperature, at 250°C ,is located where the flow velocity of the Mercury reaches 5m/s.
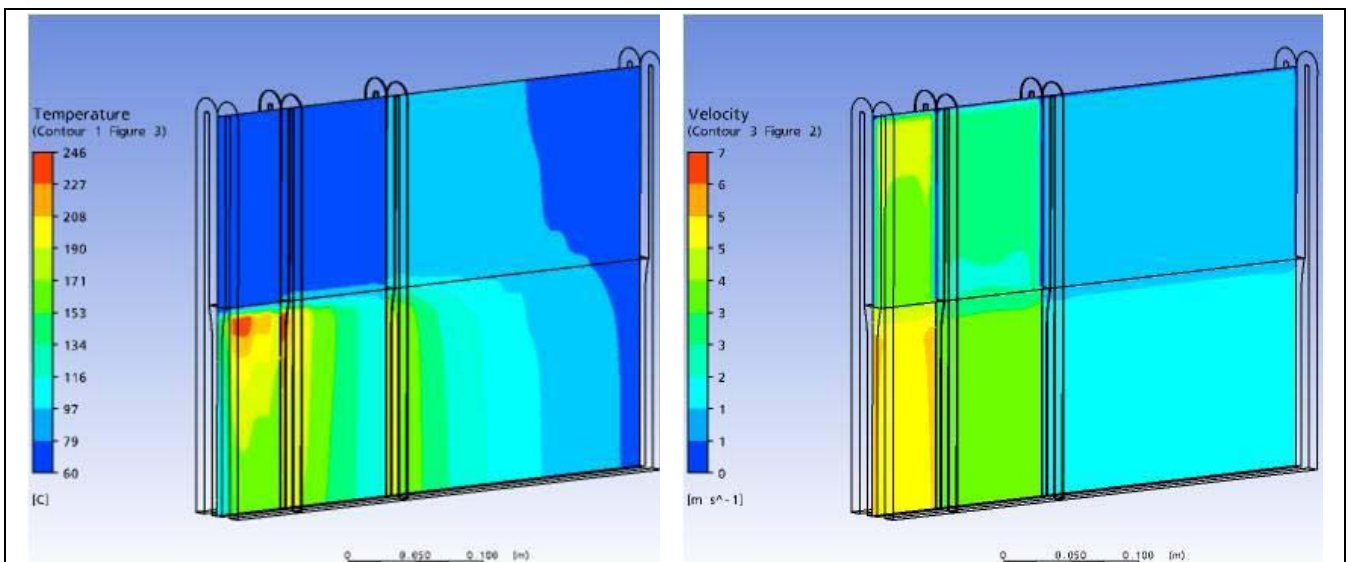

Figure 76: Power density (GeV/cm3/primary) in a Hg target for a 1 GeV proton beam. [Ref17]

Different experiments documented in [Ref15] showed that it is possible to create a film of mercury with the necessary dimensions for use in windowless target and to adjust the flow velocity in each section. The beam interaction with the liquid metal film requires more R&D. Design of the full target would be needed however to test the hydraulic behaviour under operational conditions.

Figure 77 hereafter sums up the requirements on the film velocity resulting from the CFD analysis documented in full in [Ref17].
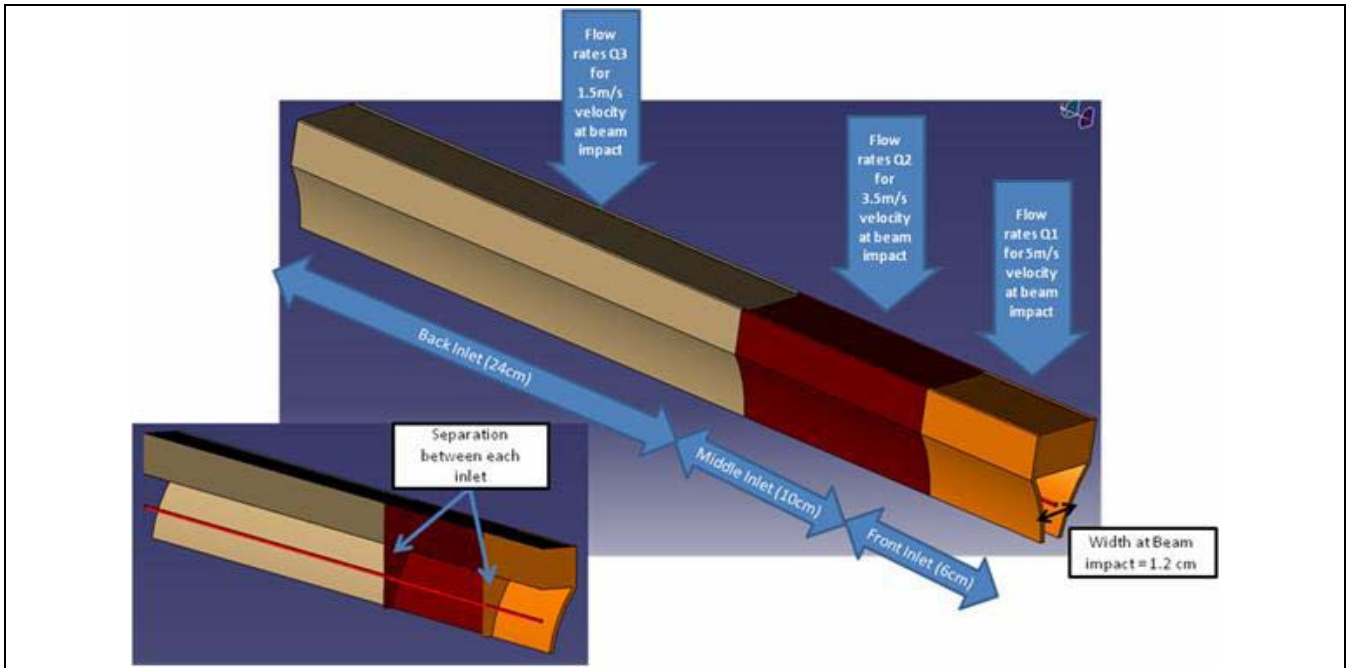
Figure 77: Ideal speed distribution at the film former. [Ref17]

3.2.3 Hydraulic performance of the WTF target

According to theoretical estimations, well – shaped solid walls are incorporated must be the injector body in order to stabilize a liquid metal film in the beam direction. The shape of the walls of the injector ensures an almost flat free surface in the transverse plane, at a peak velocity in the mercury film of about 2m/s [Ref14].

During the spring of 2007 IPUL performed several attempts to establish stable free falling liquid In/Ga/Sn eutectic film in their experimental facilities. These efforts were part of an IPUL project for the introduction of a novel full-scale Hg liquid film neutrino spallation target.

Several rectangular shaped (approx. 10x100mm) jet inlets with differently shaped nozzle openings were tested for maximum Hg volume fraction in the jet. Finally, the inlet with multiple stripped bar openings for the jet was chosen since it resulted in almost 100% metal in the jet without any gas inclusions. However, the shape of the free-falling unrestrained In/Ga/Sn jet was judged to be unacceptable as the jet evidently shrunk during it's free-fall, with large changes in jet sectional shape.

The calculation model is shown in Figure 78.The Plateau Rayleigh instability may trigger rather unstable jet behaviour in the lower part. The deformed shape of the liquid metal film as well as oscillations of the free jet surface due to unpredictable proton beam scattering are undesirable and in some cases may even be critical for spallation target operation.

The origin of the jet shape changes is related to Bernoulli's theorem which is an acceptable assumption for our jet as the friction losses in the free surface are negligible. The theorem for any jet sections Si-Sj with respective normal oriented along the vertical Z-axis states

$$\frac{U_i^2}{2} + gz_i = \frac{U_j^2}{2} + gz_j = C(x,y)$$

Where Ui and Uj are the local velocity in sections i, j crossing the streamlines at right angle.
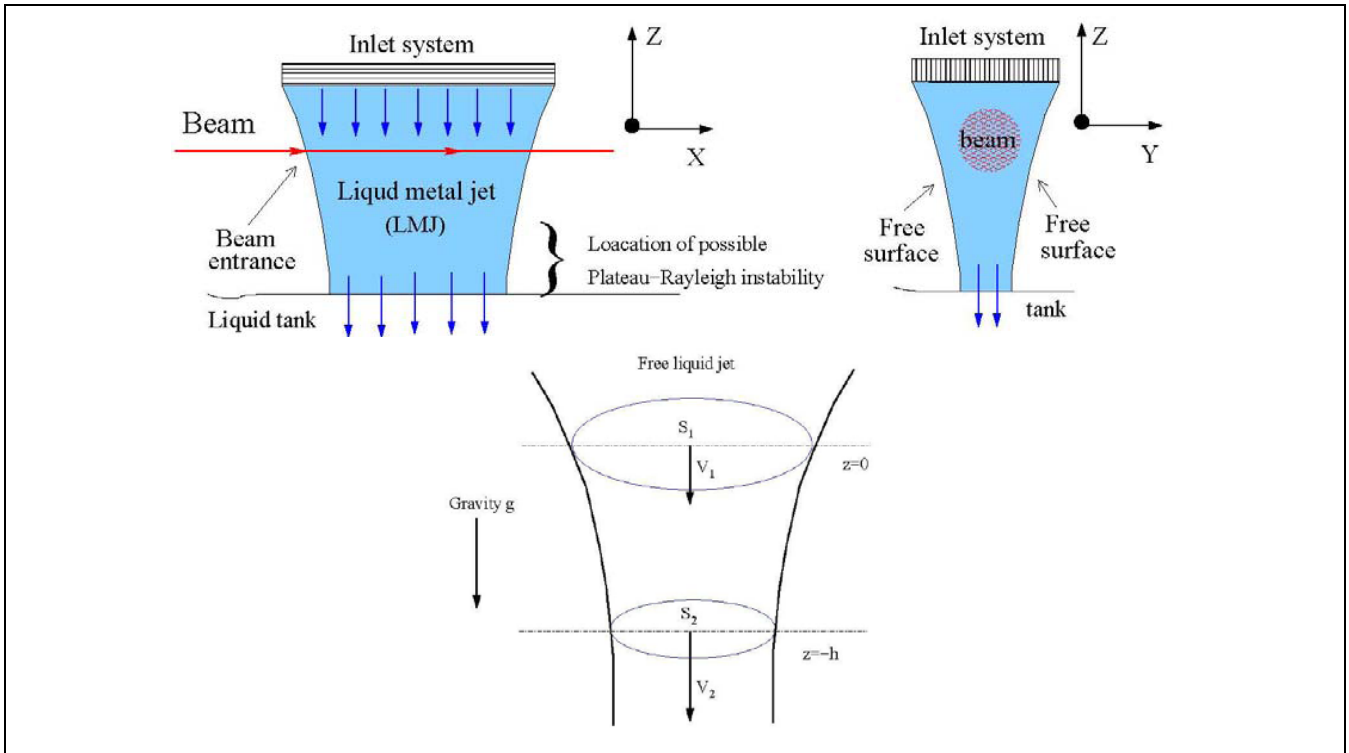
Figure 78: The film free-jet schematic calculation model [Ref14]

Let us choose a coordinate system such that

S_0 is located on the injector outlet at z = 0, whilst

S_1 is lying downstream, at a distance z = Δh,

Let us assume potential flow on inlet with U_1 = const, then C(x, y) = const, therefore Bernoulli's equation may be rewritten as,

$$\frac{U_1^2}{2} = \frac{U_2^2}{2} - gh$$

The above combined with jet continuity condition

$$SU = S_1 U_1 = S_2 U_2 = Q_{tot}$$

relates the cross sectional ratio of the jet with it's inlet velocity

$$\frac{S_2}{S_1} = \left(1 + \frac{2gh}{U_1^2}\right)^{-1/2}$$

As an example, consider a jet average velocity of 0.5 (m/s). For h = 2.5cm, the equation above yields a section ratio S_2/S_1=0.58, i.e. the free jet area is reduced by about 40%, which is a quite noticeable change. In the case of noncircular liquid film the shorter jet edges which are perpendicular to the beam direction will shrink more than the long ones, oriented along the beam. This is a concern as the beam must at all times hit the target. Hence it is deemed desirable in a production target to extend the exit lips of the film former to encompass the part of the film which lies in the path of the beam. This possibility is discussed in the next section.

3.2.4 Enhanced performance of the WTF target

One of the possible approaches to reduce the inward curvature of the liquid film surface on the beam entrance point is to constrain the jet in beam direction on both sides by solid surfaces as depicted in Figure 82. The shape of the jet-forming planes can be chosen with the aid of numerical CFD simulations.

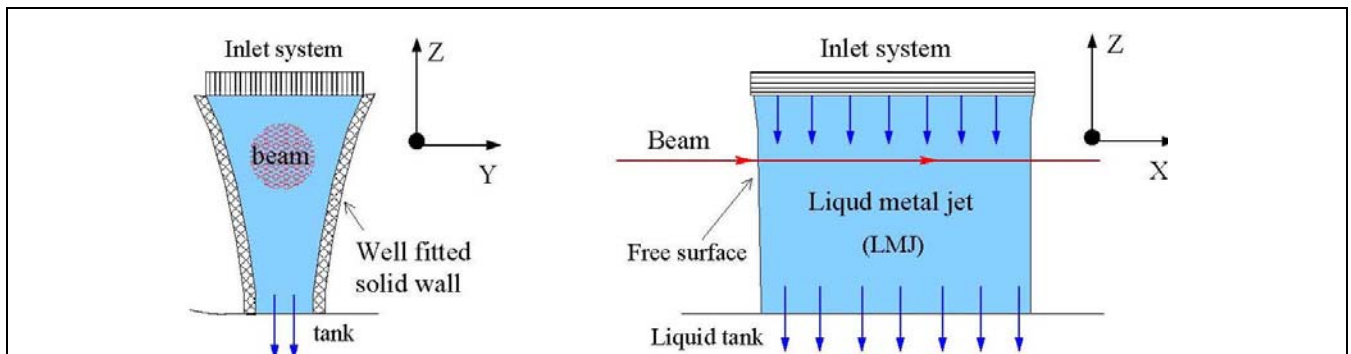In a first approximation, deviation of constraint surface from the Z-axis will follow the ideal jet law.

$$\delta = \Delta\left(1 - \sqrt{1 + \frac{2gh}{U_1^2}}\right) = \Delta\left(1 - \sqrt{1 + \frac{2gh\Delta^2 l^2}{Q_{tot}^2}}\right)$$

Where

Δ is the inlet width,

l is the inlet length,

Q_{tot} is the flow rate

Figure 79: Enhanced film free-jet schematic calculation model [Ref14]

Although the proposed constrained liquid jet design solves geometric and surface tension-related stability problems, it also introduces an additional turbulence in the liquid film due to liquid jet interaction with constraining walls.

Turbulent pulsations may affect the free surface near the beam entrance location, leading to unpredictable local beam entrance angles. The maximum chaotic free surface pulsations are rather small - below 1mm - yet may be a limiting factor for the use of the proposed design for high Re jets, i.e. high velocities or thick injector shapes. Both, numerical and experimental routes are suggested in order to find maximum acceptable dimensions for a given mercury flow rate.

Numerical simulations have been conducted without the heat deposition from the proton beam to predict pressure losses in the WTF test. The general results are presented hereafter.

After internal consultations, the following dimensions of the inlet were selected for the experiment detailed in [Ref14]

Width Δ = 14.26(mm),

Length l = 107(mm)

The thickness of internal separators is 2.5(mm).

The corresponding computational domain, was designed for an average Hg velocity $U_1 = 0.5$(m/s) in the jet cross section directly after the inlet. With the dimensions given here above, this velocity results in a total flow rate through the inlet equivalent to:

Q_{tot} = 0.76 l/s

This flow rate is roughly one twentieth of the total flow rate needed to evacuate the full beam power; as such the test is to be viewed as a sub-scale experiment representative of full flow conditions. The Open FOAM CFD package toolkit was used for all simulations. A conventional k ε model was chosen for the turbulence. Boundary conditions applied during the simulations to the computational domain were also standard for CFD. Thus, on all solid surfaces, such as the inlet and the jet forming walls zero velocity and standard k ε wall functions were set. A uniform velocity was set on the domain inlet, while pressure gradient conditions were corrected by taking into account gravitational force. Zero pressure conditions and zero normal gradients for the velocity are set at the outlet. On free surfaces free slip conditions were set.

Since results above are from stationery fluid dynamics models, the initial conditions are not specified. First indications from the simulation are that a pressure loss of 0.3 [m^2/s^2] * 13500 [Kg/m^3] = 4'050 [Pa] for a flow rate of 0.76 l/s is to be expected.

The power needed to evacuate the peak power deposition at the front end of the beam has been estimated at around 5 m/s. Given that pressure losses in a fluid follow roughly a square root law, such a tenfold increase in flow rate would result in a hundredfold increase in pressure losses through the jet from 4'050 Pa to 405'000 Pa, or 4 Bar. However it should be emphasized that the top speed of 5 m/s is mot needed along the entire 40 cm beam path, such that demand on the pump will be somewhat lower.
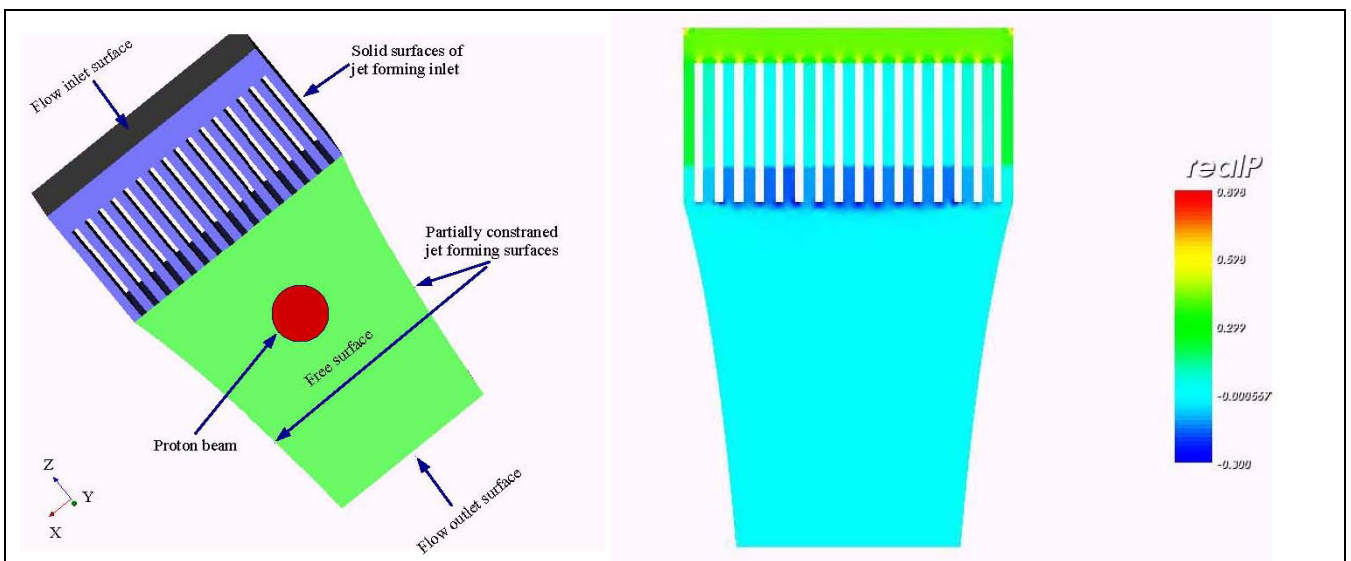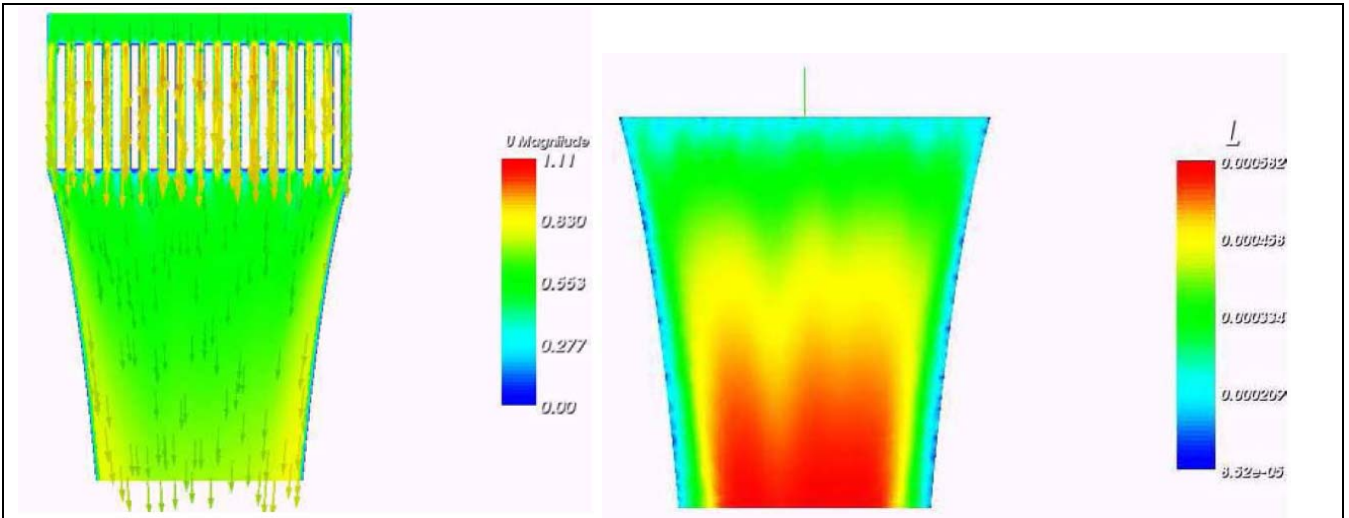

Figure 80: Numerical simulation of film free-jet – Density-normalised pressure P/ρ in m ^{2}/ s^2 [Ref14]

The velocity distribution is shown in Figure 81. In the real target the shape of free surface would differ from a flat surface, due to pressure equalisation between gaseous and liquid metal environments. However, driven by the need to simplify the numerical problem and enhance convergence, a flat free surface jet has been assumed. In this case pressure deviations from the reference are indicative of where the free surface jet would be unstable. This is translated, using the formula below, into deviation in [m] from a flat and is shown on the right-hand side of Figure 81.

$$\varepsilon = \frac{k^{3/2}}{L} \quad \text{or} \quad L = \frac{k^{3/2}}{\varepsilon}$$

Figure 81, right shows rather small amplitudes in the turbulent pulsations, under ½ mm, which would be quite acceptable for use with a proton beam. However, this result is unverified as it depends on an approximate k-ε model, thus experimental verification is required.


The experimental validation of these theoretical simulations was precisely the goal of a dedicated experiment as described in [Ref14]

Figure 81: Numerical simulation of film free-jet – velocity in [m/s] (left) and size of pulsating deviations from a flat surface in [m] (right) [Ref14]

The simulations show the potential benefit of flow formers in equalizing the velocity distribution at the free jet exit where the beam hits the film jet side-on. A first conceptual design shown below in Figure 82 was suggested, with a uniform velocity film formed by honeycomb. The tailoring of the film flow velocity profile according the local heat deposition was the reason for development of different former section as pictured in the right-hand side of Figure 82. This is achieved by choosing appropriately the thickness and length of separate channels feeding the film jet.

The inlet tube at the top of the unit feeds the incoming mercury through small holes in the wall to throttle the flow which ensures a uniform distribution of liquid along the unit. In order to ensure the pressure head required at the entrance of profile former is met, the pressure must be measured and fed back in a control loop to the pump power. Additionally, a pouring – over unit can be introduced outside or inside of this assembly.
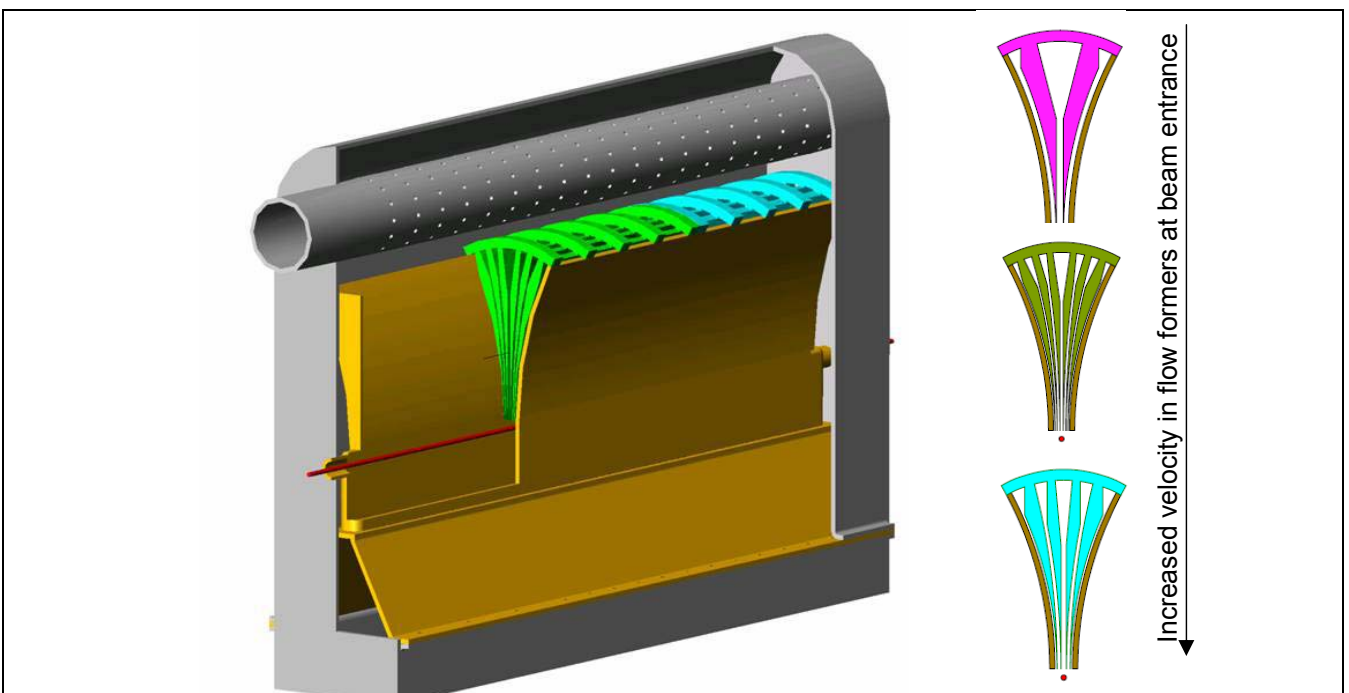
Figure 82: Implementation of design in a proposed advanced version of the WTF [Ref14]

4 Conclusions

Two designs have been proposed for the Eurisol converter target and validated in detail by a series of engineering studies and dedicated tests. All proposed designs have been reviewed and checked for matters related to thermal, hydraulic performance and structural integrity. The analysis conducted thus far has shown that the designs are well able to fulfil the requirements set on the converter target.

The baseline target featuring a window cooled by liquid metal is deemed relatively simple to manufacture as most steps do not resort to expensive manufacturing techniques or exotic materials. Undoubtedly the thin window (0.8 mm currently) is a challenge; however there is an alternative window design with a thicker 1.4mm window if a wider beam is selected. The window peak stresses, at approximately 100 MPa, and temperatures less than 400°C ensure that the integrity of the window under irradiation is not a concern. Hydraulic performance of the target has also reached the desired goal with a pressure loss of 1-2 Bar; an optimum given the high mercury speeds attained.

The windowless target offers great potential to deliver superior neutronic performance particularly in the energetic hard spectrum, a capability unique to this type of configuration. It is a less conventional solution and was studied in detail to ensure stable flow of liquid metal and an optimal configuration relating to heat evacuation. The tailoring of separate jets to suit the heat deposition is seen as a major advance which will benefit future developments of this type of target

Both designs were the subject of dedicated hydraulic tests which served as an ultimate validation of the calculations performed in the engineering phase.